Università degli Studi di Milano-Bicocca

Department of Materials Science

PhD program in Materials Science and Nanotechnology - 32^{nd} Cycle

Investigating metal-organic/inorganic interfaces with different dimensionalities from first-principles

Candidate:

Ugolotti Aldo

Reg. # 774295

Tutor:

Prof. Brivio G. P.

Co-Tutor:

Dr. Fratesi G.

Academic Year 2018–2019

Abstract

In the last decades, the ability to control the behavior of the matter at the nanoscale has yielded many technological breakthroughs. Such miniaturization steps have been triggered not only by the development of novel experimental techniques of synthesis and characterization of the materials, but also by the introduction of advanced theoretical models based on quantum mechanics. Through these models, it has been possible to simulate the behavior of the matter in order to support, expand and also predict experimental results.

Being at the heart of the majority of devices of everyday use, the interfaces created by the coupling of metallic surfaces with either organic or inorganic materials are of great importance in current technology. A proper characterization of the geometry and the electronic properties of such interfaces is paramount in defining the performances of a device; additionally, it can help in identifying new physical processes which can lead to novel technologies.

The work included in this thesis is focused on the study of interfaces where materials with different dimensionality are deposited on metallic surfaces. The models more appropriate for describing such systems have been identified in order to extract the physical properties more relevant to describe the active processes at the interfaces but also to be compared with and fully exploit the experimental data.

Four cases have been taken into account, as prototypes of materials with different dimensionality: a single organic molecule, pentacene, representing the isolated system, chains of carbon atoms, representing mono-dimensional systems, a silicene sheet, representing a two-dimensional system and the reconstruction of Si atoms on a substrate as a limit case of higher dimensionality. Part of the study has been dedicated to identify the properties of the pristine materials, but the main effort has been focused on the changes of such properties induced by the presence of metallic surfaces as Pt(111), Au(111), Ag(111) and Ag(110) respectively, commonly found in opto-electronic devices.

From the atomistic point of view, the geometry and the electronic property of each

system have been derived within the framework of density function theory. Such an approach is suited for the ground state only: therefore it has been necessary to extend the theoretical models to describe the excited states too, which are those commonly probed by experimental techniques. Every technique, however requires a dedicated approach to deal with and solve the related model.
In particular, here the x-rays absorption spectrum has been investigated to gather insights on the interactions between pentacene and Pt(111) and to verify the contribution of carbon chains in the absorption from organic molecules with mixed sp^1, sp^2 hybridization states. The optical absorption has been then investigated along with the reflectivity for silicene grown on Ag(111), in relation with the electronic structure of the system and its modifications induced by the functionalization of the surface through the adsorption of H or F at different coverages. It has been shown that silicene peculiar properties are lost not only because of the presence of a substrate, but because of the reactivity itself of Si atoms. As a last case, the deposition of Si on the substrate made of a thin film of NaCl grown on Ag(110) has been investigated in order to understand whether is possible to recover the Dirac cone structure. As experimental results do not provide a solid evidence about the actual formation of a silicene overlayer, additional insight was indeed required about the structure of the reconstruction of Si atoms. Both a static and a dynamic approach have been followed, in order to find the best structure matching the experimental topography and to tailor the self-assembly process itself. Finally, the most probable configuration has been searched through a novel approach based on genetic algorithms, which are inspired by the natural selection process observed in biology to optimize the evaluation of random configurations.

Contents

Introduction

One of the founding paradigms of Materials Science is to tackle with the complexity of the matter and identifying its smaller bricks, namely molecules or atoms and their mutual interactions, in order to find a rationale governing their properties. The characteristics of a material, such as the chemical composition or the structure, can be dealt with at the scale of few atoms, pushing forward the understanding of physics and chemistry in the realm of quantum mechanics. Among the many aspects of technology, electronics may be the best example of how the benefits brought by such improvements, given its connection to our every day's life. To give a scale of it, the phones used to stay in touch with anyone in the world and that can fit easily in a pocket, they have thousand times more computational power than the computers used in the end of the 60's by NASA to send men on the surface of the moon [1].

The driver of such progress can be identified, among other factors, in the optimization of the building blocks of electronic devices and their structuring at the nanoscale can exploit quantum-mechanical effects to define new operational paradigms. Just to name a few, the tunneling, ordering or delocalization of the electrons which may allow for an enhanced charge transport, or even something more radical as the formation of condensed states, which behave differently from the electrons themselves.

The final properties of the device are deeply influenced by the formation of interfaces delimiting one or more materials as their morphology and electronic properties would be coupled together and possibly mixed to form a new material. Metallic surfaces are certainly one of the most common constituent of interfaces, because of their role either as electrode or as substrate for the subsequent growth of different materials. Their properties have been effectively tuned through functionalization by coupling them with both organic or inorganic compounds, especially as active materials for electronic transport, optical absorption or catalytic reactions. In this perspective, the dimensionality plays an important role for the behavior of a material, mainly because the presence of a surface along one or more directions changes the electronic structure and dynamics. The

investigation of the physical process at the interfaces of such systems is a key step for understanding the functionality of a device.
The field of the study of surfaces has gathered in the last decades a set of standard tools to rely on, to probe the structure, the chemical composition and the electronic properties of a material. Some of them will be briefly introduced in Chapter 1 for a reference about how to connect the measured data with the underlying physical processes. From an atomistic point of view, which will be presented with more detail in Chapter 2, the numerical approach for constructing the ground state has to be extended with a formalism which is suitable to construct the excited states of the system, or at least reconstruct some of their properties.
In this work prototypical systems of different dimensionality have been investigated by the means of their geometry and their spectral signatures, in relation with the interaction with a metallic substrate. The adsorption of an aromatic molecule, pentacene, on the Pt(111) surface will be discussed in Chapter 3 through both experimental and theoretical x-ray absorption results as a case of the behavior of an isolated system. The spectroscopic fingerprints of carbon structures of different hybridization states will be theoretically investigated in Chapter 4, in particular related to the contribution of carbon linear chains, as example of mono-dimensional adsorbates. The case of a two-dimensional thin structure is discussed in Chapter 5 for silicene grown on the Ag(111) surface and functionalized by the adsorption of H and F atoms; in particular the electronic structures are related to the optical absorption and reflection spectra. Finally, in Chapter 6 the dynamics of a more extended system is investigated in the case of the reconstruction of Si atoms deposited on a substrate consisting of a thin film of NaCl grown on the Ag(110) substrate.

Chapter 1

Experimental background

Approaching the investigation of a new material, several techniques have became nowadays a standard in surface analysis; in the following of this chapter will be described some of the most common ones. Part of them are used to infer the structure of the sample by imaging the electronic distribution at the surface through scanning tunneling microscopy (STM) or by reconstructing the lattice structure through low energy electron diffraction (LEED) and extended x-ray adsorption fine structure (EXAFS); in other cases the structure of the electronic states is probed, as done by x-ray photoemission spectroscopy (XPS), near edge x-ray adsorption fine structure (NEXAFS) or optical adsorption and reflection, the latter through surface differential reflectivity spectroscopy (SDRS). Despite the fact that such techniques make use of either electrons or photons, not all of them are constrained by Abbe's principle, directly correlating the characteristic size of the feature to be observed with the wavelength associated to the probe; therefore it could be more useful to adopt a classification based on the main physical mechanism involved in the process of measurement. It might also be important to point out that several techniques, especially those using electron sources or probes, in order to collect a signal with the lowest noise and to avoid spurious effects most of the techniques listed above (with the exception of reflectivity and other optical characterization) require the sample to be put in a sealed chamber with high or ultra-high vacuum, with pressure $\lesssim 10^{-8}$ mbar. Similarly, during the growth the ambient pressure has to be controlled in order to ensure the highest quality of the sample.

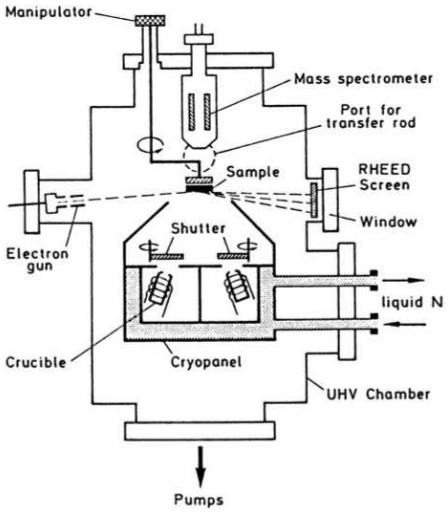

Figure 1.1: Schematic representation of a growth chamber for molecular beam epitaxy. For chemical vapor deposition, the reactants can be injected into the chamber through feeding lines coming from outside instead of shuttered crucibles. In the picture, RHEED refers to the diffraction pattern formed by reflected electrons. Image taken from Ref. [2].

1.1 Building the surface of a (new) material

The process of growing a film of a material often starts by choosing the most appropriate substrate, which will act as support and, in most cases, as template for the subsequent step. This material is selected having in mind its role in the final device; therefore it would necessary to consider its electro-chemical properties which are given by its composition, as for example reactivity, magnetization or conductivity and also of its structural features, namely its crystal structure. In particular, these characteristics can be selected by playing with its composition, but also the orientation of the surface to be exposed. When a substrate is to be created, the desired orientation of the surface of the selected material is obtained, usually through cleavage: this technique exploits the mechanical weaknesses within the material for growing faults that can extend up to the point of breaking the material in a (more) controlled way. After this step the surface has to be perfected, in order to remove chemical impurities and geometrical defects and achieve high quality substrates: this is done by repeating several cycles of sputtering and annealing. The first technique consists in bombarding the sample with a beam of noble metal atoms which have enough kinetic energy to kick the atoms of the substrate out of the surface, effectively leveling the roughest features. By annealing, instead, the sample is heated at temperatures which are high enough to increase to mobility of the

atoms at the surface and helping them to overcome any energy barrier trapping them in non-relaxed states, without melting the material. Once the surface is ready, the actual growth can commence by depositing the elements composing the desired material for a direct growth regime or its chemical precursors for an indirect regime. The deposition is obtained by heating the source element and controlling its flow impinging on the surface; the main techniques which are employed today are the molecular beam epitaxy (MBE) and the chemical vapor deposition (CVD), for which a general sketch of the equipment is reported in Fig. 1.1. Both share the same working concept, but differ in the level of control of the working parameters, namely pressures, deposition rate and purity of reactants. In particular MBE is the most accurate one, but at the expense of requiring lower deposition rates or ambient pressures and restricting to purer sources, therefore increasing dramatically the growth times and the cost for production.

1.2 Electron Tunneling: STM

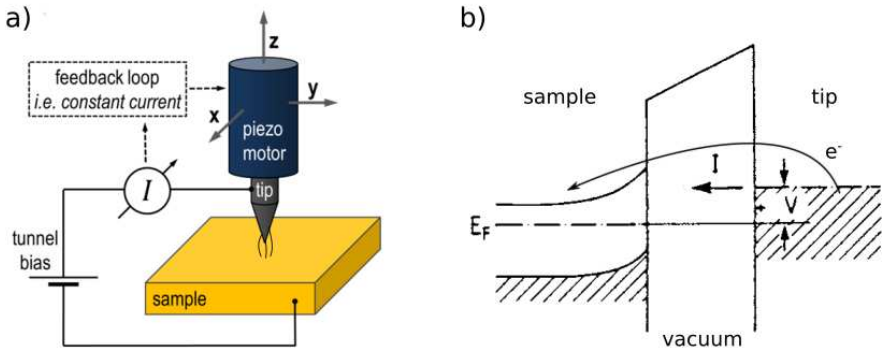

Figure 1.2: Overview of STM schematics (panel a) and principle of operation (panel b). I and V label the tunneling current and tunneling bias, respectively. In the example pictured here, the voltage lowers the energy reference of the sample with respect to the tip, allowing few electrons to be transferred. Images adapted from Refs. [2, 3].

Scanning Tunneling Microscopy (STM) allows for the surface to be scanned with an atomic in-plane resolution, returning a map of the tunneling current, which is related to the electronic orbitals. A scheme of the experimental setup is reported in Fig. 1.2: the sample is separated from a metallic tip by a gap of few angstroms which acts as a potential barrier. As stated by quantum physics, the electronic states can behave like

waves and therefore can propagate by tunneling through the vacuum, with a probability strongly dependent from the thickness of the gap. This latter fact is responsible for the local nature of the measure, as the states not directly below the tip experience a much larger dumping factor. Sample and tip are put in electrical contact so a bias potential can be applied in order to offset the energy structure of one region compared to the other. In this way, it is possible to select the state to be probed, therefore the instrument is sensitive to both valence or conduction bands of the sample by measuring the electrons tunneling from or to the sample, respectively. Applying the Fermi golden rule to the process and considering the Tersoff-Hammann approximation to the typical states of the tip for constructing the matrix which describes the wavefunction probability it is possible to write [4] the tunneling current as:

$$I \propto VR^2\chi^4 \int_{E_F}^{E_F+V} \rho(\mathbf{r_0}, E)dE \tag{1.1}$$

where V,I are the offset bias and the tunneling current,χ is the decay length of the wavefunction in vacuum (which, along the tip position $\mathbf{r_0}$ is connected with the gap size) while R is the radius of the spherical tip, $\rho(\mathbf{r_0}, E)$ is the local density of states of the sample and E_F is the Fermi energy. There are three degrees of freedom which can be played with in an STM: offset bias, tunneling current and position of the tip (in particular along the vertical to the surface); hence the instrument can be operated in two modes for microscopy operations: constant current or constant height. In the former case, the tunneling current is kept constant by a feedback loop in the electronics while the tip is left free to follow the density profile, along the scanning direction, of the electronic density; in the latter one, instead, the distance of the tip from the sample is kept constant and the tunneling current is the quantity being recorded along the surface. One of the main drawbacks of this technique is the actual inability to return directly the ionic configuration and to obtain the geometry of the atoms. The results need to be de-convoluted from the electronic structure, through the help of a simulated model.

1.3 (Low energy) Electron Diffraction: LEED

Additional information about the structure of the material at the surface can be retrieved from the investigation of the diffraction patterns formed by the atoms when acting as scattering center for an external beam, which in this case can be made of electrons, which possess the correct associated wavelength to be able to produce fringes as the interference takes place at atomic scale. The electrons impinging on the surface behave as a plane wave, each being scattered by the denser charge distributions around the

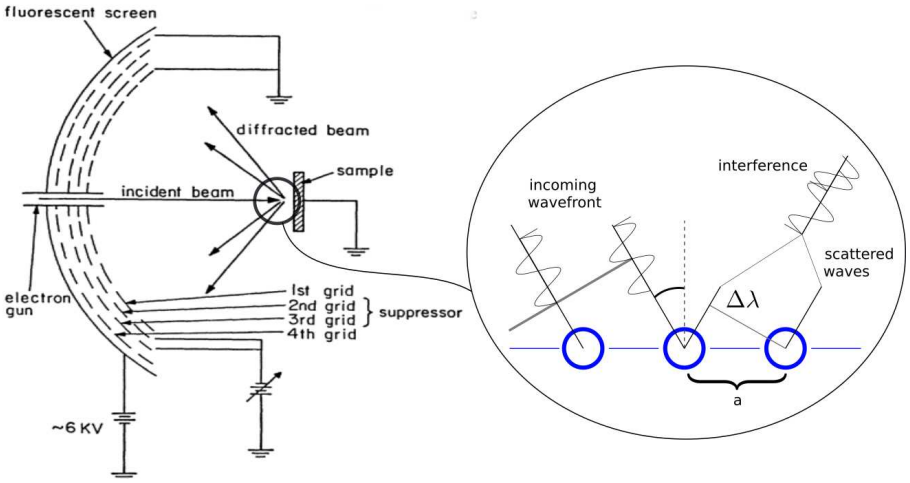

Figure 1.3: Sketching the equipment of LEED and the formation of diffraction pattern. In the zoomed region, an example of interference of the incoming/scattered electron waves is reported for a linear chain of atoms of spacing a. The difference in wavelength $\Delta\lambda$ drives the superposition of the two waves. Image adapted from Ref. [5].

atoms, which become sources of in-phase spherical waves; the outgoing waves finally interfere, depending on the difference in 'wave path', as shown in Fig 1.3 for the simplified case of a linear chain of atoms. At different observing angles correspond different phase matching conditions, therefore if an hemispherical detector is placed around the sample bright fringes should appear as the conditions are favorable for constructive interference. Considering a crystalline lattice defined by $\mathbf{R} = n\mathbf{a}_1 + m\mathbf{a}_2 + l\mathbf{a}_3$, and its corresponding reciprocal one $\mathbf{G} = r\mathbf{b}_1 + p\mathbf{b}_2 + q\mathbf{b}_3$, by explicitly calculating when the scattering amplitude is at maximum [6], the conditions at which the constructive interference occurs are $\mathbf{k}_{out} - \mathbf{k}_{in} = \mathbf{G}$. These corresponds to the Bragg condition in one dimension $\sin(\theta) = \frac{n\lambda}{2a}$, where the angle θ, proportional to the distance between two bright spots, is related to the lattice spacing a through the wavevector λ of the impinging electron. Therefore, the grid that is recorded on the screen is proportional to the reciprocal lattice of the sample; if more than one crystalline phases are stacked inside the sample, some of them would be detected as well by LEED, because of the penetration depth of an electron of few nanometers [7]. In such cases the additional lattices would be superimposed to the original one, which usually belong to the clean surface, allowing to compare the two structures and determine the overlayer lattice; however, two additional effects have to be evaluated carefully when interpreting the diffraction pattern [5, 8] because they result in additional modulation of the intensity of the spots. The first one is related

to the atomic structure within each lattice cell, which can induce additional diffraction; for every node $\mathbf{G}_i$ in the reciprocal space, the quenching factor can be approximated as $\sum_j e^{i\mathbf{G}_i \cdot \mathbf{r}_j}$ where $\mathbf{r}_j$ are atomic coordinates within the cell. The second effect is related to dynamical effects for electrons, as they undergo multiple scattering events before being emitted from the surface; this result may be due to the folding of the pattern of the overlayer onto the reciprocal lattice of the substrate.

1.4 Photon Absorption or Reflection

Photon absorption is the phenomenon taking place in a material when, as a beam of light shines on the sample, a photon is destroyed and the system is promoted from ground to an excited state, and it can be seen as an electron being transferred from an occupied state to an empty one. In such representation, once the energy of the photons is given, all possible transitions between pair of states with the same energy difference can occur at once, each with the proper probability. Several regions can be identified in the band structure of an element, distinguished by their physical features: focusing on the final states, the electrons can be promoted to two kind of regions, namely one where the states are bound to the nucleus, called conduction band, and one where their are unbound from the potential of the positive ions, therefore the (photo)electron is free to propagate. The former states, instead, are usually split into a valence band, which is made of those states which respond to external chemical environment, and core states, which are much less reactive and more characteristic of the chemical species the atom belong to. Three kinds of transitions can be therefore be identified, as reported in Fig

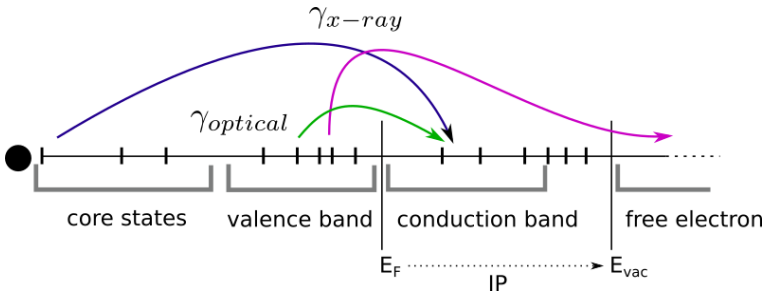

Figure 1.4: Schematics of the photoexcited transitions in a single atom. E_F marks the Fermi level, E_{vac} labels the vacuum level, IP is the ionization potential, γ_{opt} and γ_x are the optical and x-ray photon, respectively.

1.4, namely from core states to conduction band, from valence band to above the vacuum level and from valence band to conduction band; given the typical energy of those states,

the first two excitation can be promoted through x-ray photons, while the last one with optical photons.

1.4.1 X-ray spectroscopy

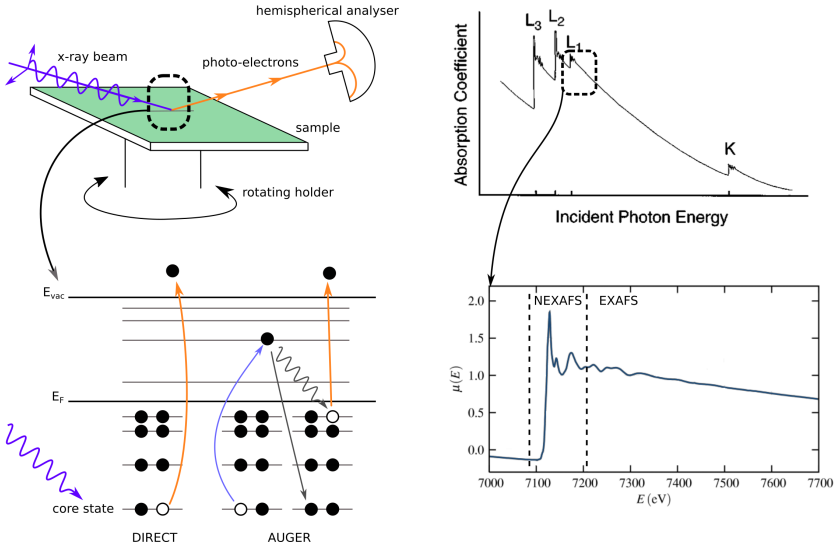

Figure 1.5: Left panel: schematic representation of a typical equipment setup for measuring x-ray beam absorption, where ejected electrons are collected by the detector. The photoelectrons can be produced through a direct or an indirect process, by changing the energy of the x-ray beam. Several experimental conditions can be exploited, by changing orientation of the sample and polarization of the beam. Right panel: typical x-ray absorption spectrum, reporting different transition edges (L or K lines); zooming around one of those, the energy regions into which the spectrum is commonly split are labeled. Image adapted from Ref. [9].

X-ray energy photons are usually chosen to excite deeply-lying states in the electronic structure, namely core states; the beam energy is selected in order to match that of the orbitals in the atomic shell, which depend on the chemical species which is going to be probed. For lighter elements the choice for the core states is more limited, as for example the $1s$ for C, while the heavier elements can offer broader possibilities. As the energy of the x-rays is varied, different empty electronic states can be reached, showing a spike in the absorption, which is indirectly measured by counting either the photo-emitted electrons from the sample or the photons emitted by the recombination process; a picture illustrating the working concept is shown in Fig 1.5 for the former case. The electrons are emitted by direct excitation, as the electron is promoted directly above

the vacuum level, or through Auger effect, namely the excited electron decays back on the core hole, transferring its energy to a secondary electron which is then promoted in the unbound continuum as well. The energy of each photo-emitted electron is inferred by an hemispherical analyzer, which exploits a magnetic field to bend the path of the electrons, and the full spectrum is finally reconstructed. As the electronic states of an atom (especially the ones in the valence band) are sensitive to the interaction with the surrounding ones, the energy required to ionized a core state changes accordingly; therefore changes in the position of the absorption peak at different edges, as those investigated by x-ray photoemission spectroscopy (XPS), may suggest different chemical environment for the detected chemical species. Investigating the absorption spectrum, instead, after the onset of every core state excitation, a richer set of feature can be observed and the spectrum itself can be further split in two regions, namely the near edge x-ray absorption fine structure (NEXAFS) and extended x-ray absorption fine structure (EXAFS) respectively, the intensity modulation of which is due substantially to two main processes, which are related to different properties of the material.

XPS

In this technique the quantity that is accounted for is the energy required to create the excited state with the ionized atom, which is called binding energy; this value accounts for both the removal of the core electron and the relaxation of the electronic states which experience a smaller screening of the ionic charge. On a larger scale, the XPS spectrum shows a series of absorption spikes, corresponding to the ionization of the core edge of any chemical species that falls within the excitation volume. Each of those peaks may present then a finer scale modulation, as the atoms of the same element may be experiencing different chemical environments, namely interacting with diverse neighbors or possessing a different ground state by changing the atomic orbital hybridization scheme (i.e. sp^2/sp^3), which defines a chemical shift. When considering surface processes as adsorption, such shifts are not determined only by the interaction of the atomic orbitals with the surrounding electronic states, as those introduced by a surface, where such a component is called initial state effect, but also on the correlation between the electronic states within the ionized atoms; this latter component is referred to as final state effects. The XPS spectrum can carry additional information regarding the geometry of the atoms, as different structures can be distinguished by different chemical environment, which can be exploited, however only after a model has been constructed, to verify the adsorption configuration of clusters or molecules.

NEXAFS

Conversely from XPS, NEXAFS spectroscopy relies on the resonant excitation of the core electron to one of the single particle excited states, thus probing the structure of empty electronic states, as the initial one is fixed by the beam energy. The measured quantity by this technique is usually the absorption cross section, since in this case whether or not a transition is triggered depends on the fulfillment of the selection rules between the initial and final state, for which, since an electric dipole is formed, the angular momentum of the state must change. Moreover, if the electromagnetic field associated with the photon is linearly polarized along in-plane directions or out-of-plane ones different electric dipoles can be excited, changing the final states that can be reached by the electronic transitions. Therefore, by comparing the NEXAFS spectra taken at different beam polarization it is possible to extrapolate some insight into the adsorbate configuration with minimal assumptions.

EXAFS

While closer to absorption edge the spectral features are directly connected with the electronic excited states, at higher energy, namely above few tens of eV from the edge, the photo-emitted electrons are almost free to propagate; therefore they can be elastically scattered by the electronic distribution localized around each atom and the two waves interfere at the site of the x-ray absorption. Because of this phenomenon the intensity in the cross section of the absorption is modulated as the two waves overlap in-phase or out-of-phase: in the former case the electronic state is enhanced resulting in a (slightly) increased absorption probability; conversely, the destructive interference causes the target electronic state to be damped as the state would not be allowed anymore, resulting in the adsorption cross section to be diminished. In this technique the measured quantity is $\chi(E)$, defined as the oscillation of the absorption with respect to the mostly uniform background after the edge. As happens in all lattices, the interference pattern is related to the inter-atomic distances; therefore from investigating the point of maximum in the signal it is possible to extrapolate the distance between neighboring atoms (first neighbor, second neighbor, ...), therefore getting additional information about the geometry of the system on a chemically selective basis.

1.4.2 Optical spectroscopy: absorption or reflection

Conversely from x-rays, because of their lower energy optical photons can probe a set of electronic states restricted to ones around the Fermi level, namely those in the valence

and in conduction band. For the same reason, the penetration depth of optical photons is much larger than the one of both electrons and x-rays as several nanometers get probed altogether. For a beam impinging on a sample, the photon can undergo three different paths: the first is the already described as absorption, which happens if in the material there are electronic states with the correct energy difference. If there are no states available, the photon can either travel unaffected by the electronic distribution of the atoms or be scattered; in the first case the beam is transmitted through the material while in the second case it is reflected by the surface, where the probability of the process that would take place is directly related to the electronic structure of the sample. The intensity of the transmitted beam is inversely proportional to the thickness of the sample, therefore only for optically thin materials the absorption can be measured with such a technique. More commonly, the surface is characterized by reflection techniques; in particular, for investigating interfaces, a two-steps method is preferred, called surface differential reflectivity spectroscopy (SDRS). In this technique, the intensity of the reflected beam is continuously measured as the new material is grown over the substrate, the changes in reflectivity are extracted and then normalized to the signal recorded, at the same energy, for the clean surface. Among the advantages of such technique, the use of a reference for the reflectivity allows for an increase of the contrast of the surface-related features and an increase in the accuracy of the measurement through a partial cancellation of the errors.

Chapter 2

Theoretical foundations

2.1 Many-electron systems

Through quantum mechanics, the matter can be described, at any time t, by a number of states, labeled $|\psi\rangle$, which are defined through the Schrödinger equations :

$$i\hbar\frac{\partial}{\partial t}|\psi(t)\rangle = \hat{H}|\psi(t)\rangle \tag{2.1a}$$

$$\hat{H}|\psi\rangle = E|\psi\rangle \tag{2.1b}$$

where $\hat{H}$ is the Hamiltonian operator which defines the physical phenomena taking place within the system. The first time-dependent equation can be simplified, in the case of a system at the equilibrium, into the second, time-independent equation, where E is an eigenvalue representing the energy of the related eigenstate. In the case of the hydrogen atom, the time-independent equation can be solved exactly [10] and the wavefunctions $\phi(\mathbf{r},\mathbf{R}) = \langle \mathbf{r},\mathbf{R}|\phi\rangle$ associated to the single electron states, or atomic orbitals, can be explicitly written in terms of the coordinates $\mathbf{r},\mathbf{R}$ of the electron and the ion, respectively. The problem, however, gets quickly too complicated to be solved exactly for other atoms and, in general, for other many-body systems, because its the eigenstates $|\Psi\rangle = |\Psi(\mathbf{r}_1,\ldots,\mathbf{r}_N,\mathbf{R}_1,\ldots,\mathbf{R}_M)\rangle$ are defined through the mutual, dynamical interaction of all the electrons (considering the ions fixed by assuming the Born-Oppenheimer approximation[1]) and therefore they will depend on the coordinates of all the particles included in the system. In fact the hamiltonian can be constructed for a non-relativistic

[1]The Born-Oppenheimer approximation assumes that the motion of ions and electrons can be decoupled thanks to difference in their masses ($m_i \simeq 1000\ m_e$), allowing the global wavefunction to be written as the product of the ionic and electronic ones as $\Phi(\mathbf{r}_i,\mathbf{R}_j) = \Psi(\mathbf{r}_i)\chi(\mathbf{R}_j)$

system, assuming atomic units, as the sum of kinetic and electrostatic terms as:

$$\hat{H} = \sum_i \frac{-\nabla^2}{2} + \frac{1}{2}\sum_{i,j}\frac{1}{|\mathbf{r}_i - \mathbf{r}_j|} - \sum_{i,j}\frac{Z_j}{|\mathbf{r}_i - \mathbf{R}_j|} + \frac{1}{2}\sum_{i,j}\frac{Z_i * Z_j}{|\mathbf{R}_i - \mathbf{R}_j|} \tag{2.2}$$

which solution would require to solve a system of entangled equations, in number of the order of Avogadro's number; therefore such complexity must be tackled with a number of approximations and techniques, both numerical and theoretical.

In order to account for the fundamental non-distinguishability of the electrons, it is necessary to properly describe the many-body states, in which single-particle fermion states get properly anti-symmetrized and normalized, as:

$$|\Psi) = |\phi_1\rangle \otimes \ldots \otimes |\phi_N\rangle \tag{2.3a}$$

$$|\Psi\rangle = \frac{1}{\sqrt{N!}}\sum_P (-1)^P |\Psi_P) \tag{2.3b}$$

where the sum runs over all different permutations of index P and $\otimes$ indicates the external product between Hilbert spaces. Therefore it is necessary to redefine the action of an operator onto such states; in the case of an operator O acting on l particles, introducing normalized single-particle states, it is possible to write the expectation value of such an operator onto an N-particles state as:

$$\left(\Psi'\middle|\hat{O}^l\middle|\Psi\right) = \frac{1}{l!}\sum_{i_1\neq\ldots\neq i_l}\left(\phi'_{i1}\ldots\phi'_{il}\middle|\hat{O}^l\middle|\phi_{i1}\ldots\phi_{il}\right)\prod_{k\neq i1\ldots il}\langle\phi'_k|\phi_k\rangle \tag{2.4}$$

where the indexes of the matrix are related to the selection of l states onto which the operator is evaluated. For an operator acting on space (and spin, in general) coordinates $\mathbf{x} = (\mathbf{r}, \sigma)$, and focusing on the elements of the diagonal, it is possible to explicit the wavefunctions as:

$$\left\langle\hat{O}^l\right\rangle_\Psi = \int \mathrm{d}\mathbf{x}'_1\ldots\mathrm{d}\mathbf{x}'_N\, d\mathbf{x}_1\ldots\mathrm{d}\mathbf{x}_N\,\gamma_N(\{\mathbf{x}'\}_N;\{\mathbf{x}\}_N)\left\langle\mathbf{x}'_1\ldots\mathbf{x}'_N\middle|\hat{O}^l\middle|\mathbf{x}_1\ldots\mathbf{x}_N\right\rangle \tag{2.5a}$$

$$\gamma_N(\{\mathbf{x}'\}_N;\{\mathbf{x}\}_N) = \Psi^*(\mathbf{x}'_1\ldots\mathbf{x}'_N)\Psi(\mathbf{x}_1\ldots\mathbf{x}_N) \tag{2.5b}$$

where the function γ_N is called density matrix and the corresponding operator is $\hat{\gamma}_N = |\Psi\rangle\langle\Psi|$. The expectation value can be further transformed [11] through Eq. 2.4 as:

$$\left\langle\hat{O}^l\right\rangle_\Psi = \int \mathrm{d}\mathbf{x}'_1\ldots\mathrm{d}\mathbf{x}'_l\,\mathrm{d}\mathbf{x}_1\ldots d\mathbf{x}_l O^l(\mathbf{x}'_1\ldots\mathbf{x}'_l;\mathbf{x}_1\ldots\mathbf{x}_l)\gamma_l(\mathbf{x}'_1\ldots\mathbf{x}'_l;\mathbf{x}_1\ldots\mathbf{x}_l) \tag{2.6a}$$

$$\gamma_l(\mathbf{x}'_1\ldots\mathbf{x}'_l;\mathbf{x}_1\ldots\mathbf{x}_l) = \int \mathrm{d}\mathbf{x}_{l+1}\ldots\mathrm{d}\mathbf{x}_N\,\gamma_N(\mathbf{x}'_1\ldots\mathbf{x}'_l,\mathbf{x}_{l+1}\ldots\mathbf{x}_N;\mathbf{x}_1\ldots\mathbf{x}_N) \tag{2.6b}$$

where the reduced density matrix γ_l has been introduced. From the density matrices, the corresponding spinless quantities can be constructed as:

$$\rho_l(\mathbf{r}'_1\ldots\mathbf{r}'_l;\mathbf{r}_1\ldots\mathbf{r}_l) = \binom{N}{l}\int \mathrm{d}\sigma_1\ldots\mathrm{d}\sigma_l\,\gamma_l(\mathbf{x}'_1\ldots\mathbf{x}'_l;\mathbf{x}_1\ldots\mathbf{x}_l) \tag{2.7a}$$

which can be related, in the case of $l = 1$ for the local representation $\rho(\mathbf{r}_1) = \rho_1(\mathbf{r}_1; \mathbf{r}_1)$ to the charge density of the single electron. It is useful to further develop the formalism and change the way many-body states are described, namely shifting from a representation based on their coordinates, to one based on the number of particles occupying the states as:

$$|\Psi(\mathbf{r}_1, \ldots, \mathbf{r}_N)\rangle = |n_1\psi_1, \ldots, n_N\psi_N\rangle = |n_1, \ldots, n_N\rangle \tag{2.8}$$

This new framework, called second quantization, allows to introduce [12] two new operators $a^\dagger_\alpha$ and a_α, called construction and destruction operator respectively, the action of which on a state, for a system of Fermions[2], adds or removes a particle on a selected state, which can be written as:

$$a^\dagger_\alpha |\alpha_1, \ldots, \alpha_N\rangle = \begin{cases} |\alpha, \alpha_1, \ldots, \alpha_N\rangle \\ 0 \text{ if } |\alpha\rangle \text{ occupied} \end{cases} \tag{2.9a}$$

$$a_{\alpha_i} |\alpha_1, \ldots, \alpha_N\rangle = \begin{cases} (-1)^{i-1} |\alpha_1, \ldots, \alpha_{i-1}, \alpha_{i+1}, \ldots, \alpha_N\rangle \\ 0 \text{ if } |\alpha_i\rangle \text{ unoccupied} \end{cases} \tag{2.9b}$$

$$\left\{a_\alpha, a^\dagger_\beta\right\} = \delta^\beta_\alpha \tag{2.9c}$$

$$\left\{a_\alpha, a_\beta\right\} = \left\{a^\dagger_\alpha, a^\dagger_\beta\right\} = 0. \tag{2.9d}$$

where the last two equations describe the canonical anti-commutation rules. In particular, every state can be re-written, by introducing the empty state $|0\rangle$ corresponding to the vacuum, with the action on it of as many construction operators as the number of particles, in the following way:

$$|\Psi\rangle = |\phi_1 \ldots \phi_N\rangle = a^\dagger_1 \ldots a^\dagger_N |0\rangle \tag{2.10}$$

The generality of the second quantization approach can be extended to a large variety of particles, which can be not only electrons, but also something more exotic as phonons for vibrations, or electron-hole pairs for optical excitations. It is possible to extend the definition of the two operators above in order to reconnect with the coordinate representation and introducing the so-called field operators, which can be written as

[2] In a Fermionic system the particles have to obey the Pauli exclusion principle. For a Bosonic system such a limitation is lifted and the normalization factor for the construction/destruction operators acting on a state is $\sqrt{n_\alpha + 1}$,$\sqrt{n_\alpha}$, respectively.

follows:

$$\hat{\Psi}^\dagger(\mathbf{r}) = \sum_\alpha \psi_\alpha(\mathbf{r}) a_\alpha^\dagger \tag{2.11a}$$

$$\hat{\Psi}(\mathbf{r}) = \sum_\alpha \psi_\alpha^*(\mathbf{r}) a_\alpha \tag{2.11b}$$

$$\left\{\hat{\Psi}(\mathbf{r}), \hat{\Psi}(\mathbf{r}')\right\} = \left\{\hat{\Psi}^\dagger(\mathbf{r}), \hat{\Psi}^\dagger(\mathbf{r}')\right\} = 0 \tag{2.11c}$$

$$\left\{\hat{\Psi}(\mathbf{r}), \hat{\Psi}^\dagger(\mathbf{r}')\right\} = \delta(\mathbf{r} - \mathbf{r}') \tag{2.11d}$$

where the spin degree of freedom can be added straightforwardly since it acts as an independent parameter as $|\Psi\rangle_\sigma = |\Psi, \sigma\rangle = |\Psi\rangle \otimes |\sigma\rangle$. From the field operators it is useful to also construct a density operator:

$$\hat{n}(\mathbf{r}) = \hat{\Psi}^\dagger(\mathbf{r})\hat{\Psi}(\mathbf{r}) \tag{2.12}$$

which represents, within both the first and second quantization formalism, the number of electrons at a point $\mathbf{r}$ in space.

Up to now, the system has been considered stationary and the time has not been directly included; to do so, it is useful to introduce [13] the interaction picture which combines the properties of the Heisenberg and the Schrödinger representations to allow the time evolution of both states and operators. In this case, the time evolution of the expectation value of an operator $\hat{O}(t)$ under the perturbation $\hat{H}_{ex}(t)$ can be expressed, at the first order, as:

$$\delta\left\langle \hat{O}(t)\right\rangle = i\int_{t_0}^{t} \mathrm{d}t' \ \langle\Psi_{gs}|T\Big[\hat{H}_{ex}(t'), \hat{O}(t)\Big]|\Psi_{gs}\rangle \tag{2.13}$$

where $T[A, B]$ represents the time-ordered action of the two operators taking care of the causality. This result will be useful later on for introducing ax explicit form for the electronic response function: in that case, the generic operator $\hat{O}(t)$ is replaced by the so-called deviation operator $\tilde{n}(\mathbf{r}, t) = \hat{n}(\mathbf{r}, t) - \langle\hat{n}(\mathbf{r}, t)\rangle$ and the perturbation Hamiltonian is the energy associated to an electron experiencing the electric field carried by a photon.

2.2 (Electronic) Ground state

The first step in the investigation of a system is solving the Schrödinger equation to obtain the ground state of the electronic problem; among the possible ways in which the complexity of such a problem can be dealt with, the density functional theory (DFT) has become a standard tool in computational materials science. This framework is

founded onto the pioneering work of Hohenberg and Kohn [14], who defined the energy of a system as a functional $F_{HK}[\rho(\mathbf{r})]$ depending on the charge density and proved that such functional is unique given an electron density. Moreover they also showed that the energy of the ground state can be obtained through a variational approach and the charge density minimizing the energy functional is the one corresponding to the ground state. However, a practical approach for actually calculating such density was defined by Kohn and Sham [15], who first split the Hohenberg-Kohn functional as:

$$F_{HK}[\rho] = T_S[\rho] + V_h[\rho] + V_{ext}[\rho] + (V - V_h)[\rho] + (T - T_S)[\rho] \tag{2.14}$$

where T_S represents the kinetic energy for independent electrons, V_h is the Hartree component of the potential, namely its electrostatic part and all the remainder from the original functional is grouped under an unknown functional, called exchange and correlation, $V_{xc} = (V - V_h) + (T - T_S)$ In addition, they created an auxiliary system in which the electrons do not interact but experience an effective potential; in this way the minimization of the total energy would read:

$$\frac{\delta E_{HK}[\rho]}{\delta\rho} = \frac{\delta T_S[\rho]}{\delta\rho} + \frac{\delta V_h[\rho]}{\delta\rho} + \frac{\delta V_{ext}[\rho]}{\delta\rho} + \frac{\delta V_{xc}[\rho]}{\delta\rho} - \mu \tag{2.15a}$$

$$\frac{\delta E_{aux}[\rho]}{\delta\rho} = \frac{\delta T_S[\rho]}{\delta\rho} + \frac{\delta V_{eff}[\rho]}{\delta\rho} + \mu \tag{2.15b}$$

$$\frac{\delta V_{eff}[\rho]}{\delta\rho} = v_{eff}(\mathbf{r}) = v_h(\mathbf{r}) + v_{ext}(\mathbf{r}) + v_{xc}(\mathbf{r}) \tag{2.15c}$$

$$H_{KS}[\rho] = t_S[\rho] + v_h[\rho](\mathbf{r}) + v_{xc}[\rho](\mathbf{r}) + v_{ext}[\rho](\mathbf{r}) \tag{2.15d}$$

where μ, called 'chemical potential', is introduced as Lagrange multiplier, and the equivalence derives from focusing onto the ground state for which, as described above, the potential is unique. Recollecting the many-body formalism introduced at the beginning of the chapter, in particular the Eq. 2.6a describing the expectation value of an l-particles operator acting onto a properly symmetrized N-particles state, it is possible to gather further insight about the electrostatic potential as it can be described by a two-particles operator:

$$V[\rho] = \left\langle \hat{V[\rho]} \right\rangle = \int \mathrm{d}\mathbf{r}_1' \, \mathrm{d}\mathbf{r}_2' \, \mathrm{d}\mathbf{r}_1 \, \mathrm{d}\mathbf{r}_2 \, \frac{\rho_2(\mathbf{r}_1'\mathbf{r}_2'; \mathbf{r}_1\mathbf{r}_2)}{|\mathbf{r}_1 - \mathbf{r}_2|} \delta\big(\mathbf{r}_1' - \mathbf{r}_1\big)\delta\big(\mathbf{r}_2' - \mathbf{r}_2\big) \tag{2.16a}$$

$$\rho_2\big(\mathbf{r}_1'\mathbf{r}_2'; \mathbf{r}_1\mathbf{r}_2\big) = \frac{1}{2}\rho(\mathbf{r}_1)\rho(\mathbf{r}_1)\big[1 + h(\mathbf{r}_1'\mathbf{r}_2'; \mathbf{r}_1\mathbf{r}_2)\big] \tag{2.16b}$$

Thanks to the decomposition of the reduced density matrix introduced into the last equation, the total potential can be split into the classical Hartree term plus a functional

term which includes the residual non-local interaction h. It is possible to show that the normalization of such term is equal to -1, allowing to address this component as the hole generated by the repulsion between correlated electrons induced by Pauli exchange. Therefore, even though the framework described until now results in a Schrödinger equation which is exact in principle, up to date it has not been possible to derive in a similar exact fashion the correct relationship for the exchange and correlation hole, nor for the correlation term similarly introduced for the kinetic energy. Hence, an approximation has to be made in order to actually define the functional to be included in the Hamiltonian to be solved: several approaches can be derived indeed; among the most popular ones are the local density approximation (LDA) and the generalized gradient approximation (GGA). For the former the charge density is assumed to be almost uniform in space, therefore the jellium model is directly worked out to derive, as for example in the Perdew-Wang parametrization [16], the exchange and correlation energy: For the latter approach, the Taylor expansion of the charge density is taken into account, which is then truncated at the desired order and some boundary conditions are enforces; one of the most reliable flavors of functional parametrization is the one introduced by Perdew-Burke-Enrzerhof (PBE) [17]. However, despite the high level of sophistication, the exchange-correlation functional described above are at best short-ranged and fail to describe the longer range interactions between the higher poles in the electric charge distribution. The most famous of which is the Van der Waals(vdW) interaction, namely the one correlating the (permanent or fluctuating) electric dipoles. Similarly with the exchange-correlation functional, it is possible to depict the flavors of vdW implementations as a Jacob's ladder [18]. The first steps are occupied by pairwise force contributions, which arise from the approximation of the electron-electron response function [19, 20] between two atoms with independent electronic dipoles. In this case the coefficients of such terms maybe static, namely calculated for isolated atoms as in the D2 by Grimme [21] or dynamically obtained from the actual electronic density of the system, for example as coded in Grimme D3 [22, 23] or $\mathrm{vdW_{surf}}$ by Tkatchenko and Scheffler [24]. If the electronic distributions are closer in space, their interaction can be more effectively incorporated into a functional term to the energy [19, 20], in an similar way the exchange-correlation energy is treated. Depending from the approach in which the functional is constructed, several families of functionals can be defined; for example the one so-called vdw-DF [25, 26] is based on the response function as obtained through the Lorentz model (plasmon-pole approximation) which will be introduced later on.

2.3 Numerical framework

The Schrödinger equation which is constructed from the Kohn-Sham Hamiltonian reported in Eq. 2.15d, although simpler that the many-body one, cannot generally be solved analytically, thus requiring the use of high performance computers. Nowadays several codes based on DFT are available that result in similar accuracy [27] but differ in the mathematical description of the problem. During this work I dealt mainly with "infinite" systems, namely bulk or surfaces, in which periodic boundary conditions are enforced along one or more directions. Such configurations are best suited for a plane waves basis set because of the Bloch theorem, which allows the wave functions to be written as:

$$\psi_{n,\mathbf{k}}(\mathbf{r}) = e^{i\mathbf{k}\cdot\mathbf{r}} u_{n,\mathbf{k}}(\mathbf{r}) \tag{2.17}$$

where $u_{n,\mathbf{k}}(\mathbf{r}) = u_{n,\mathbf{k}}(\mathbf{r}+\mathbf{T})$ for a lattice described by the translations $\mathbf{T} = n_1\mathbf{a}_1 + n_2\mathbf{a}_2 + n_3\mathbf{a}_3$ and $\mathbf{k}$ is a vector of the reciprocal space, defined in the first Brillouin zone. For any vector $|\mathbf{G}\rangle$ of the reciprocal lattice, a plane wave can be written in the form:

$$\langle \mathbf{r}|\mathbf{G}\rangle = \frac{1}{\sqrt{\Omega}} e^{i(\mathbf{G})\cdot\mathbf{r}} \tag{2.18}$$

and the electronic wave functions can be expanded through the Fourier transform as:

$$|\psi_j\rangle = \sum_{\mathbf{G}} c_{j,\mathbf{k}+\mathbf{G}} \, |\mathbf{k}+\mathbf{G}\rangle \tag{2.19}$$

$$c_{j,\mathbf{k}+\mathbf{G}} = \frac{1}{\sqrt{\Omega}} \int \mathrm{d}\mathbf{r} \, \psi_j(\mathbf{r}) e^{-i(\mathbf{k}+\mathbf{G})\cdot\mathbf{r}} = \tilde{u}_j(\mathbf{k}) \tag{2.20}$$

and the components of the Hamiltonian would be simplified into:

$$\big\langle \mathbf{k}+\mathbf{G}' \big| \hat{T}^{KS} \big| \mathbf{k}+\mathbf{G} \big\rangle = (\mathbf{k}+\mathbf{G})^2 \delta_{\mathbf{G},\mathbf{G}'} \tag{2.21a}$$

$$\big\langle \mathbf{k}+\mathbf{G}' \big| \hat{V}_{coul} \big| \mathbf{k}+\mathbf{G} \big\rangle = 4\pi \frac{\rho(\mathbf{G}-\mathbf{G}')}{(\mathbf{G}-\mathbf{G}')^2} = \tilde{V}_{coul}(\mathbf{G}-\mathbf{G}') \tag{2.21b}$$

$$\big\langle \mathbf{k}+\mathbf{G}' \big| \hat{V}_{xc} \big| \mathbf{k}+\mathbf{G} \big\rangle = \tilde{V}_{xc}(\mathbf{G}-\mathbf{G}') \tag{2.21c}$$

$$\big\langle \mathbf{k}+\mathbf{G}' \big| \hat{V}_{ext} \big| \mathbf{k}+\mathbf{G} \big\rangle = \sum_{j}^{ions} e^{-i(\mathbf{G}-\mathbf{G}')\cdot\mathbf{R}_j} V_{ext,j}(\mathbf{G}-\mathbf{G}') \tag{2.21d}$$

If the dimensionality of the system has to be reduced along one or more directions, a supercell method can be used. This consists in defining a fictitious cell, aka the supercell, which is periodic in all the three directions and contains the atoms to be included in the simulation. Such a system has to be carefully designed, in order to minimize the spurious interaction between the supercell and its replicas; this can be

achieved by both inserting a suitable vacuum region around the atoms and choosing the correct sampling of the Brillouin zone, which defines the maximum periodicity which can be accounted for within the simulation. Compared with alternative basis sets, the plane waves offer the opportunity to control the accuracy of the results only changing the number of vectors to use in the simulation, i.e. by specifying the corresponding energy cutoffs. Their main disadvantage is that of requiring a very large basis size when dealing with the electrostatic interaction of the ions, because of their highly localized potential wells. A common approach in this case is to use an approximated, weaker ionic potential, called pseudopotential, which is constructed [28, 29] to represent only a selected subset of less-bound atomic orbitals, assuming that the deeper ones would not be involved in any interaction. In this way, the computational load can be reduced, at the price of losing the energy reference for the electronic states; because of this fact, all the meaningful energy results in a pseudopotential representation must be presented in terms of energy differences between eigenvalues. The computational benefit coming from this approximation is related to the flavor of the choice of the pseudopotential, namely which constraint is enforced for its generation, in particular the total charge conservation. The hardest potentials, i.e. the ones requiring a larger basis set, are constructed [30] by enforcing the exact match of the pseudo charge with the real one and therefore are called 'norm-conserving'; the softest pseudopotentials, instead, allow the definition of an augmentation charge inside the core region and are labeled 'ultrasoft' [31]. In addition to the choice of the pseudization scheme of the core charge, the projector augmented wave (PAW) formalism [32, 33], allows to establish a one-to-one correspondence between the pseudo-wavefunction $\left|\tilde{\Psi}\right\rangle$ and the all-electrons one $|\Psi\rangle$ through a linear transformation $|\Psi\rangle = \mathcal{T}\left|\tilde{\Psi}\right\rangle$. Such an operator is defined to conserve the expectation value of an observable as $\left\langle\tilde{\Psi}\middle|\tilde{A}\middle|\tilde{\Psi}\right\rangle$ where $\tilde{A} = \mathcal{T}^{\dagger}A\mathcal{T}$. The linear transformation operator can be defined considering that the all-electron and the pseudo atomic orbital wavefunctions $|\phi_{\mathbf{R}n}\rangle$, $\left|\tilde{\phi}_{\mathbf{R}n}\right\rangle$ must be identical outside an augmentation region of radius $\mathbf{r}_0$, therefore introducing a projector $|\tilde{p}_{\mathbf{R}n}\rangle$ which has the property $\left\langle\tilde{p}_{\mathbf{R}'n'}\middle|\tilde{\phi}_{\mathbf{R}n}\right\rangle = \delta^{n',n}_{\mathbf{R}',\mathbf{R}}$. In this way, the operator which transforms the pseudo-wavefunction in an all-electron one can be defined as:

$$\mathcal{T} = 1 + \sum_{\mathbf{R}n}\left[|\phi_{\mathbf{R}n}\rangle - \left|\tilde{\phi_{\mathbf{R}n}}\right\rangle\right]\langle\tilde{p}_{\mathbf{R}n}| \tag{2.22}$$

where $\mathbf{R}$ represent the ionic coordinates and the projectors are defined only once, at the moment of constructing the pseudopotential and stored for later use.
During the work presented in this thesis, the DFT calculations have been carried out

mainly through the QuantumESPRESSO suite [34, 35], but also with the Vienna Ab-initio Simulation Package(VASP) [36–39]. The k-point grid, introduced by Bloch's representation, is generated through the Monkhorst-Pack scheme [40], with a converged mesh resulting in a total energy accuracy of $\simeq 1$ meV.

2.4 Excited state (properties of)

As defined in the previous section of this chapter, DFT is a framework constructed from a variational approach, therefore it should be in principle not suited for dealing with excited states. Just to mention a notable example, the band gaps of several semiconductors can be highly underestimated when calculating the electronic structure of the system. In fact, in the Kohn-Sham approach, the single-particle eigenvalue do not hold actual physical meaning, but the one corresponding to the highest occupied molecular orbital (HOMO), as per Janak theorem [41] $\varepsilon_{HOMO} = E(N) - E(N-1)$. Correspondingly, the chemical potential, as introduced in Eq. 2.15a, depends on the number of electrons in the system as $\mu(N) = \delta E(N)/\delta\rho(N)$. Therefore, even though sometimes some qualitative results for excited state properties can be extracted from a DFT calculation, the investigation of such states, which is often crucial in relating to experimental findings, must require a dedicated treatment; for this thesis' work, the ground state has been calculated first using DFT, then additional steps have been performed based onto such wavefunctions to extract the desired property of the excited states. In the following sections, the theoretical modeling required for the different experimental technique to be coupled with will be introduced; the physical concepts underlying each technique have already been introduced in the previous chapter.

2.4.1 XPS

The quantity of interest of this technique is the binding energy, which represents the energy required for the photon to photoemit a core electron as $\mathrm{BE} = E_{ex}(n_{core} = 0) - E_{gs}(n_{core} = 1)$. However, from the numerical point of view, the use of pseudopotentials usually prevents the definition of an unique energy reference for all atoms and the binding energy can be calculated only up to an additive constant, whose value is unknown. However, for extended systems with several inequivalent atoms, the change in energy reference can be overcome by calculating the core level shifts (CLS) as $\mathrm{CLS}_i = \mathrm{BE}_i - \langle \mathrm{BE}_i \rangle$. In this way, the difference with the average on the atoms cancels the energy reference term. As the atom is ionized, the electronic states in the valence band and the

one still occupied in the core will react and relax into states more bound to the nucleus, because the screening from the core electrons is reduced. Therefore, the CLS can be ideally decomposed into a contribution due to the energy spent for removing the core electron and a contribution due to the energy gained from the relaxation of electronic states. The first component only of the CLS, which addresses the initial state effects (IS), can be numerically constructed from a perturbative approach from the ground state Kohn-Sham eigenstates ϵ_l as:

$$\mathrm{CLS}_i^{IS} = \sum_{l}^{valence} \langle \epsilon_l | v_{gs} - v_{ch} | \epsilon_l \rangle \tag{2.23}$$

where v_{gs}, v_{ch} are the ground state and excited state atomic coulomb terms contained in the respective pseudopotentials. The actual relaxation of the electronic states in response to the core hole, called final state effects, are taken into account through the so-called ΔSCF method [42] instead; in this case the CLS can be regarded, for a spin-independent case, as differences of Kohn-Sham eigenvalues, namely:

$$\mathrm{CLS}_i^{FCH} \sum_{i}^{valence} 2(\epsilon_i^{ex} - \epsilon_i^{gs}) + (\epsilon_{core}^{ex} - \epsilon_{core}^{gs}) - \epsilon_{core}^{gs} \tag{2.24}$$

where ϵ^{ex} are self-consistently calculated with the pseudopotential with the core hole. The drawback of the latter approach is that, since the pseudopotential has to be generated with the remaining core electron included in the valence band, the calculation gets heavier. The CLS have to be obtained for every inequivalent excited atom, by changing the atom at which the new pseudopotential is set; such multiplicity would represent the height of the spectrum for the corresponding CLS, generating the simulated shape of XPS spectrum. The two equations reported above allow to interpret more easily the change in CLS between core excited atoms experiencing different chemical environments. In case of a charge transfer, the reduced(increased) charge would lead to smaller(larger) screening of the core potential, resulting in an increased(reduced) relaxation of the electronic states, hence a larger(smaller) CLS. In presence of a surface, in particular a metallic one, the atom would experience instead a larger potential, given by the attractive image potential: similarly to the electronic loss, the larger the potential, the larger the relaxation, therefore resulting in an increase of the CLS.

2.4.2 NEXAFS

NEXAFS spectroscopy addresses the cross section of the resonant photo absorption, which in general can be described through the Fermi golden rule:

$$\sigma(\omega) \propto \sum_f |M_{fi}|^2 \delta(E_f - E_i - \omega) \tag{2.25}$$

where the matrix element of the process can be constructed as $M_{fi} = \langle \Psi_f | \hat{D} | \Psi_i \rangle$ from the electric dipole operator $\hat{D}$ created because of interaction between the excited electron and the core hole left behind, and the all-electron many-body states $|\Psi_f\rangle$, $|\Psi_i\rangle$. Such equation shouldn't be directly tackled with through DFT, because it may fail in its description of the unoccupied states; nonetheless, the absorption cross section can be manipulated through several approximations in order to express it in terms of the states calculated for a suitable Kohn-Sham system. First it is useful to explicit the pseudo-wavefunctions through the PAW formalism introduced by Eq. 2.22 as:

$$M_{fi} = \langle \Psi_f | \hat{D} | \Psi_i \rangle = \sum_{\mathbf{R}nm} \left\langle \tilde{\Psi}_f \middle| \tilde{p}_{\mathbf{R}n} \right\rangle c^i_m \left\langle \phi_{\mathbf{R}n} \middle| \hat{D} \middle| \phi^i_{m\mathbf{R}_0} \right\rangle \tag{2.26a}$$

$$\sigma(\omega) \propto \sum_f \left| \left\langle \tilde{\Psi}_f \middle| \tilde{\Phi}_{\mathbf{R}_0} \right\rangle \right|^2 \delta(E_f - E_i - \omega) \tag{2.26b}$$

$$\left| \tilde{\Phi}_{\mathbf{R}_0} \right\rangle = \sum_{nm} c^i_m \left| \tilde{p}_{\mathbf{R}_0 n} \right\rangle \left\langle \phi_{\mathbf{R}_0 n} \middle| \hat{D} \middle| \phi^i_{m\mathbf{R}_0} \right\rangle \tag{2.26c}$$

where the strong localization of the excitation at an atoms carries a negligible contribution on other atoms, and the c^i_m are the coefficients expanding the (initial) wavefunction onto the atomic orbitals. It is interesting to notice that, since the projectors $|\tilde{p}_{\mathbf{R}_0 n}\rangle$ and the atomic orbitals $\phi_{m\mathbf{R}_0}$ are defined once the pseudopotential is constructed, the total state $\left| \tilde{\Phi}_{\mathbf{R}_0} \right\rangle$ is completely defined as soon as the coefficients c^i_m are given. The level of approximation of such a calculation strongly depends on the parametrization of the core hole into the pseudopotential: within the so-called "transition state" approach [43], the energy of the transition:

$$\omega = E^{tot}(N; n_f = 1, n_i = 0) - E^{tot}(N; n_f = 0, n_i = 1) \tag{2.27}$$

can be approximated, also taking Janak's theorem into account, as:

$$\omega = \epsilon_f(N - 1/2; n_f = 0, n_i = 1/2) - \epsilon_i(N - 1/2; n_f = 0, n_i = 1/2) \tag{2.28}$$

where the eigenvalues are those obtained from a DFT calculation which includes the half core-hole pseudopotential at the desired atom. It is possible to substitute the summation

over the final states with the action of a suitable Green function as it can be proven [44,45] that the following identity is correct:

$$\pi \sum_f |\Psi_f\rangle \langle \Psi_f| \, \delta(E_f - z) = \lim_{\gamma \to 0} \mathrm{Im}\Big\{ \tilde{G}(z, i\gamma) \Big\} \tag{2.29a}$$

$$\tilde{G}(z, i\gamma) = \tilde{G}(E_i + \omega, i\gamma) \tag{2.29b}$$

where $\tilde{G}$ is constructed from the actual Hamiltonian describing the Kohn-Sham states and the PAW transformation operator $\mathcal{T}$; finally, the cross section would read:

$$\sigma(\omega) \propto \mathrm{Im}\Big\{ \Big\langle \tilde{\Phi}_{\mathbf{R}_0} \Big| \tilde{G}(E_i + \omega) \Big| \tilde{\Phi}_{\mathbf{R}_0} \Big\rangle \, \delta(E_i + \omega) \Big\} \tag{2.30a}$$

The last equation can be solved iteratively through the Lanczos procedure [46–49] which expresses the expectation value of the Green's function operator as a continued fraction:

$$\langle \tilde{\alpha} | \tilde{G}(E, i\gamma) | \tilde{\alpha} \rangle = \cfrac{\langle \tilde{\alpha} | \mathcal{T}^{-1/2} | \tilde{\alpha} \rangle}{a_0 - E - i\gamma - \cfrac{b_1^2}{a_1 - E - i\gamma - \cfrac{b_2^2}{\cdots}}} \tag{2.31}$$

where the coefficients a_i and b_i are the eigenvalues of the eigenstates $|u\rangle_i$ of the Hamiltonian in which such an operator is in a tridiagonal form.

2.4.3 Optical spectroscopies

In order to model the macroscopic optical properties observed from experiments through the properties of matter at atomic scale, first a classical model, derived first by Lorentz, will be introduced through which it will be possible to address the most important quantities and their behavior. Then a more refined model, based on a quantum mechanical approach, will be derived in detail, which is at the foundation of the calculations performed in this thesis' work.

Classical Lorentz model

As first approach in tackling with the optical absorption, it can be useful to construct a classical model approximating the electronic excitation. From electrostatical considerations [50, 51] of a field acting on a medium, the effect of an incoming photon can be described as a spring, connecting the electron and the ions, which is being displaced out of equilibrium and therefore behaving like a spring. To generalize the model, depolarizing effects can be added to the system, representing the interaction with other electrons,

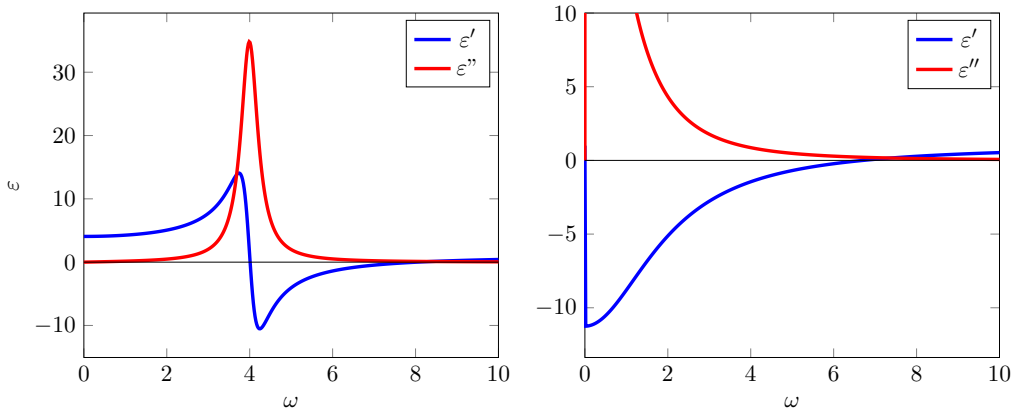

Figure 2.1: Representation of the components of the dielectric function (real ε' and imaginary ε'') as defined by the Lorentz model (left panel) and the Drude model (right panel, with $\omega_0 = 0$). The plots have been generated using $\omega_p = 7$, $\omega_0 = 4$ and $\gamma^2_{Lorentz} = 0.5$, $\gamma^2_{Drude} = 2$

as a damping term, proportional to the speed of the electron motion; a general equation of motion can be built, assuming an harmonic field, as a forced and damped system:

$$m[\ddot{\mathbf{x}} + \gamma\dot{\mathbf{x}} + \omega_0\mathbf{x}] = -eE(\mathbf{x}, t) \tag{2.32}$$

where γ is the damping constant and ω_0 is the elastic constant. The solutions of such a system allow to build the polarization vector $\mathbf{P} = N\mathbf{p} = -Ne\mathbf{x}$, which, in turn, determine the dielectric function representing the linear term coupling the total field produced in the material and the external electric field as:

$$\mathbf{D} = \varepsilon_0\mathbf{E} + \mathbf{P} \tag{2.33a}$$

$$\varepsilon(\omega) = \varepsilon_0\left(1 + \frac{\omega_p^2(\omega)}{(\omega_0^2 - \omega^2 + i\omega\gamma)}\right) \tag{2.33b}$$

$$\omega_p^2(\omega) = \frac{4\pi n(\omega)e^2}{m\varepsilon_0} \tag{2.33c}$$

where ε_0 is the dielectric constant of the vacuum and ω_p is called "plasma frequency", representing the collective vibration modes of the charge distribution, which is connected to the number of electrons participating to the transition.

The components of the dielectric functions, which are plotted in Fig. 2.1, can be

explicitly written as:

$$\varepsilon'(\omega) = 1 + \frac{\omega_p^2(\omega)\left(\omega_0^2 - \omega^2\right)}{\left(\omega_0^2 - \omega^2\right)^2 + \omega^2\gamma^2} \tag{2.34a}$$

$$\varepsilon''(\omega) = \frac{\omega_p^2(\omega)\gamma\omega}{\left(\omega_0^2 - \omega^2\right)^2 + \omega^2\gamma^2} \tag{2.34b}$$

where can be seen that, as $\gamma \to 0$, ω_0 corresponds to the transition energy, identified by a peak in absorption, namely in ε'', and that ω_p corresponds to the point at which $\varepsilon' \to 0$. Such model can be fit for describing a semiconductor, where there can be several characteristic frequencies; the dielectric function would be a superposition of the functions described above, each with proper normalization $n(\omega)$. In case of a metal, the electrons can be seen as free to move, namely not bound by the ion: to model them Drude considered the above equations, switching off the elastic force. The corresponding functions are plotted in the right panel of Fig. 2.1, highlighting the effect of having empty states just above the Fermi level.

The perturbative approach

Starting from Maxwell equations [50, 52], it is possible to show the correlation between the dielectric function ε, introduced as the electronic response triggered in the medium by an external potential V_{ext}, and some macroscopic properties observed from experiments such as the absorption coefficient or the reflectivity, which can be related to a complex refractive index $n = \sqrt{\varepsilon}$. Starting from Maxwell equations [50, 52], it is possible to properly introduce the response functions as:

$$D(\mathbf{r}) = \int \mathrm{d}\mathbf{r}'\, \varepsilon(\mathbf{r}, \mathbf{r}')E(\mathbf{r}') \tag{2.35a}$$

$$\rho_{ind}(\mathbf{r}) = \int \mathrm{d}\mathbf{r}'\, \chi(\mathbf{r}, \mathbf{r}')V_{ext}(\mathbf{r}') \tag{2.35b}$$

$$\varepsilon = \frac{\delta V_{ext}}{\delta V_{tot}} \tag{2.35c}$$

$$\chi = \frac{\delta \rho_{ind}}{\delta V_{ext}} \tag{2.35d}$$

for which we would be interested in the related "marcoscopic" quantities, like V_{ext}^M, namely their average in space; under this perspective, it would be best to move all equations in the reciprocal space (of basis vectors $\mathbf{G}_i$) through the Fourier transform, where taking an average in space correspond to taking the $\mathbf{G} = 0$ component of the transform, namely only focusing onto the first Brillouin zone. In this way, it can be

noticed that the way the the dielectric function is explicited may not be the most useful as the functional derivation would not be easily carried out in a non-local environment:

$$V_{ext}^{M}(\mathbf{q}) = \sum_{\mathbf{G}'} \varepsilon(\mathbf{q}, \mathbf{q}+\mathbf{G}') V_{tot}(\mathbf{q}+\mathbf{G}') \neq \varepsilon(\mathbf{q},\mathbf{q}) V_{tot}(\mathbf{q}) \tag{2.36}$$

Therefore, it would be of much use the definition of its inverse ε^{-1} through:

$$V_{tot}^{M}(\mathbf{q}) = \sum_{\mathbf{G}'} \varepsilon^{-1}(\mathbf{q}, \mathbf{q}+\mathbf{G}') V_{ext}^{M}(\mathbf{q}) \delta(\mathbf{G}') = \varepsilon_{\mathbf{0},\mathbf{0}}^{-1}(\mathbf{q}) V_{ext}^{M}(\mathbf{q}) \tag{2.37a}$$

$$\left(\varepsilon^{M}\right)^{-1} = \frac{V_{tot}^{M}}{V_{ext}^{M}} = \varepsilon_{\mathbf{0},\mathbf{0}}^{-1} \tag{2.37b}$$

where the long-wavelength approximation has been taken into account, namely that the perturbing potential is almost constant on the length scale of the simulated supercell; this fact, labeled "optical limit", holds indeed for optical excitations at the nano-scale. This last step allows for a definition of the dielectric function introduced in Eq. 2.35a in terms of the electronic response χ as:

$$\varepsilon^{-1} = \frac{\delta V_{ext} + V_{ind}}{\delta V_{ext}} = 1 + \delta\left(\int \mathrm{d}\mathbf{r}' \, \frac{\rho_{ind}(\mathbf{r}')}{|\mathbf{r}-\mathbf{r}'|} \right) \Big/ \delta V_{ext} = 1 + v_h \chi \tag{2.38a}$$

$$\chi_{\mathbf{G},\mathbf{G}'}(\mathbf{q},\omega) = \chi^{0}_{\mathbf{G},\mathbf{G}'}(\mathbf{q},\omega) + \chi_{\mathbf{G},\mathbf{G}'}(\mathbf{q})(v_{h;\mathbf{G},\mathbf{G}'}\chi^{0}_{\mathbf{G},\mathbf{G}'}(\mathbf{q},\omega) + v_{xc;\mathbf{G},\mathbf{G}'}\chi^{0}_{\mathbf{G},\mathbf{G}'}(\mathbf{q},\omega)) \tag{2.38b}$$

where v_h, v_{xc} are the kernels of the Hartree and exchange-correlation interaction, respectively. The last equation expresses the electronic response in the form of a Dyson equation [13], involving χ^0 which is the response of non-interacting particles. Under the independent-particle, random-phase approximations [53, 54], the potential terms are neglected, and $\chi = \chi^0$. Such term can be expressed by calculating the linear variation of the charge density in response to a perturbation as anticipated in Eq. 2.13:

$$\delta \langle \hat{n}(\mathbf{r},t) \rangle = \int \mathrm{d}\mathbf{r}' \, \mathrm{d}t' \, V_{ext}(\mathbf{r}',t') \, \langle \Psi_{gs} | T\big[\hat{n}(\mathbf{r}',t'), \hat{n}(\mathbf{r},t)\big] | \Psi_{gs} \rangle \tag{2.39}$$

Given the nature of the photon absorption, the creation/destruction of an electronic state in the conduction/valence bands may be effectively described through the electron-hole (e, h) formalism, for which it is possible to write, assuming $\mathbf{x} = (\mathbf{r}, t)$:

$$\hat{a}_{n,\mathbf{k}} = \hat{c}_{n,\mathbf{k}} \quad ; \quad \hat{a}^{\dagger}_{n,\mathbf{k}} = \hat{c}^{\dagger}_{n,\mathbf{k}} \tag{2.40a}$$

$$\hat{b}_{m,\mathbf{k}'} = \hat{c}^{\dagger}_{m,-\mathbf{k}'} \quad ; \quad \hat{b}^{\dagger}_{m,\mathbf{k}'} = \hat{c}_{m,-\mathbf{k}'} \tag{2.40b}$$

$$\hat{\Psi}_e(\mathbf{r}) = \sum_{n,\mathbf{k}>\mathbf{k}_F} u_{n,\mathbf{k}}(\mathbf{r}) e^{i\mathbf{k}\cdot\mathbf{r}} \hat{c}_{n,\mathbf{k}} \tag{2.40c}$$

$$\hat{\Psi}_h(\mathbf{r}) = \sum_{m,\tilde{\mathbf{k}}<\mathbf{k}_F} u_{m,\tilde{\mathbf{k}}}(\mathbf{r}) e^{i\tilde{\mathbf{k}}\cdot\mathbf{r}} \hat{c}^{\dagger}_{m,-\tilde{\mathbf{k}}} = \sum_{m,\mathbf{k}'<\mathbf{k}_F} u^{*}_{m,\mathbf{k}'}(\mathbf{r}) e^{-i\mathbf{k}'\cdot\mathbf{r}} \hat{c}^{\dagger}_{m,\mathbf{k}'} \tag{2.40d}$$

$$\hat{\Psi}^{H}_{e,h}(\mathbf{x}) = e^{i\hat{H}t} \hat{\Psi}_{e,h}(\mathbf{r}) e^{-i\hat{H}t} \tag{2.40e}$$

where $c^\dagger$ and c are electron construction and destruction operators and $u_{n,\mathbf{k}}(\mathbf{r})$ are functions introduced by the Bloch theorem. Remembering the definitions of $\hat{n}$ and $\tilde{n}$ introduced through Eq. 2.12 and below Eq. 2.13, the response function can be expressed [13] through the definition given in Eq. 2.35b as:

$$\chi^0(\mathbf{r},\mathbf{r}',\omega) = \frac{-i}{\sqrt{2\pi}} \int \mathrm{d}\big(t'-t\big)\, G_2^0(\mathbf{x},\mathbf{x}';\mathbf{x},\mathbf{x}') e^{-i\omega(t'-t)} \tag{2.41}$$

where the two-particle Green's function has been introduced as:

$$G_2^0(\mathbf{x},\mathbf{x}';\mathbf{x},\mathbf{x}') = \langle \Psi_{gs}|T[\hat{\Psi}_e^H(\mathbf{x}')\hat{\Psi}_h^H(\mathbf{x}')\hat{\Psi}_h^{\dagger H}(\mathbf{x})\hat{\Psi}_e^{\dagger H}(\mathbf{x})]|\Psi_{gs}\rangle \tag{2.42}$$

The completeness of many-particles Fock spaces $\sum_n = |Psi_n\rangle \langle Psi_n|$ can be exploited to decouple the action of the operators, obtaining the projection onto three many-body states $|\Psi_A\rangle$,$|\Psi_B\rangle$ and $|\Psi_C\rangle$. The action of the scalar product cancels all those states in the sums which do not respect creation/destruction of particles, for which the only states left the possible combinations of those with an additional electron and an additional hole. Therefore it is possible to assume the case where:

$$E_{gs} - E_A = E_N - E_{N+1}^{n,\mathbf{k}} = -\epsilon_{n,\mathbf{k}} \tag{2.43a}$$

$$E_B - E_C = E_{N'} - E_{N'-1}^{m,\mathbf{k}'} = \epsilon_{m,\mathbf{k}'} \tag{2.43b}$$

for which the Green's function for the and focusing on one component ($t'-t=\tau>0$) can be written as:

$$\begin{aligned} G_2^{+0}(\mathbf{x},\mathbf{x}') = \sum_{\substack{n,m \\ \mathbf{k},\mathbf{q}}} & e^{i(\varepsilon_{n,\mathbf{k}}-\varepsilon_{m,\mathbf{k}-\mathbf{q}})(t'-t)} e^{i\mathbf{q}\cdot\mathbf{r}'} e^{-i\mathbf{q}\cdot\mathbf{r}} \\ & u_{n,\mathbf{k}}(\mathbf{r}') u^*_{m,\mathbf{k}-\mathbf{q}}(\mathbf{r}') u_{m,\mathbf{k}-\mathbf{q}}(\mathbf{r}) u^*_{n,\mathbf{k}}(\mathbf{r}) \theta(t'-t) \end{aligned} \tag{2.44}$$

where $\mathbf{q} = \mathbf{k} - \mathbf{k}'$. Assuming the following equality:

$$\int_{-\infty}^{\infty} e^{i(\omega+\alpha)\tau}\theta(\tau)\,\mathrm{d}\tau = \frac{1}{\omega+\alpha+i\tau} \tag{2.45}$$

and moving to the reciprocal space, the above equation for G_2^{+0} becomes:

$$G_2^{+0}(\mathbf{G},\mathbf{G}',\omega) = \sum_{\substack{n,m \\ \mathbf{k},\mathbf{q}}} \Big| \langle m,\mathbf{k}-\mathbf{q}|e^{i(\mathbf{q}+\mathbf{G}')\cdot\mathbf{r}'}|n,\mathbf{k}\rangle \Big|^2 \left(\frac{1}{\omega + (\epsilon_{n,\mathbf{k}} - \epsilon_{m,\mathbf{k}-\mathbf{q}}) + i\tau} \right) \tag{2.46}$$

Under the optical limit, the matrix element in which the exponential operator is evaluated can be simplified as:

$$\lim_{\mathbf{q}\to 0} \langle n,\mathbf{k}|e^{-i(\mathbf{q}+\mathbf{G})\cdot\mathbf{r}}|m,\mathbf{k}-\mathbf{q}\rangle = -i\mathbf{q}\cdot\ \langle n,\mathbf{k}|\hat{\mathbf{r}}|m,\mathbf{k}\rangle \tag{2.47}$$

and it can be further optimized for the basis of plane wave, which are eigenvectors of the momentum operator, by considering:

$$\langle n,\mathbf{k}|[\hat{\mathbf{r}},H]|m,\mathbf{k}\rangle = \langle n,\mathbf{k}|\hat{\mathbf{r}}\epsilon_m|m\mathbf{k}\rangle - \langle n,\mathbf{k}|\epsilon_n\hat{\mathbf{r}}|m,\mathbf{k}\rangle = (\epsilon_m-\epsilon_n)\langle n,\mathbf{k}|\hat{\mathbf{r}}|m,\mathbf{k}\rangle \quad (2.48a)$$

$$\left[\hat{\mathbf{r}},\hat{T}+\hat{V}\right] = \hat{\mathbf{p}} \quad (2.48b)$$

To construct the full Green's function, both its causal components have to be taken into account, for which only the expansion in Eq. 2.45 differs; therefore the full equation can be written as:

$$G_2^0(\mathbf{q},\omega) = \sum_{\substack{n,m\\ \mathbf{k},\mathbf{q}}} \frac{\left|\mathbf{q}\cdot\langle m,\mathbf{k}|\hat{\mathbf{p}}+\left[\hat{\mathbf{r}},V^{NL}\right]|n,\mathbf{k}\rangle\right|^2}{(\epsilon_{m,\mathbf{k}}-\epsilon_{n,\mathbf{k}})^2}\left(\frac{1}{\omega-(\epsilon_{m,\mathbf{k}}-\epsilon_{n,\mathbf{k}})+i\tau}\right. \\ \left. -\frac{1}{\omega+(\epsilon_{m,\mathbf{k}}-\epsilon_{n,\mathbf{k}})+i\tau}\right) \quad (2.49)$$

where $\hat{V}^{NL}$ is the non-local operator included in the Hamiltonian of a single atom, which depends on the pseudopotential. Substituting the equation above into Eqs. 2.41, 2.38a and considering than in the IP-RPA approximation $\varepsilon^M = \varepsilon_{\mathbf{0},\mathbf{0}}$ the final equation for extracting the macroscopic dielectric function can be written as:

$$\varepsilon_M = 1+\frac{16\pi}{\Omega}\sum_n^{empty}\sum_m^{occ}\sum_{\mathbf{k}}\frac{W_nW_m}{\epsilon_{m,\mathbf{k}}-\epsilon_{n,\mathbf{k}}}\frac{\left|\langle m,\mathbf{k}|\hat{\mathbf{p}}+i\left[\hat{\mathbf{r}},V^{NL}\right]|n,\mathbf{k}\rangle\right|^2}{(\omega+i\tau)^2-(\epsilon_{m,\mathbf{k}}-\epsilon_{n,\mathbf{k}})^2} \quad (2.50)$$

where Ω is the volume of the primitive cell and the W_i are two weights, corresponding to the projection of the total wavefunction on the i-th atomic orbital.
Starting from this quantity, the construction of the complex refractive index [55], for a perturbing electromagnetic wave impinging at normal incidence with respect to the surface of the system, can lead the definition of several macroscopic properties, which will be of interest in the following: the first is the absorbance, representing the probability of a photon to be absorbed as it goes through the sample, which can be defined for a thin two-dimensional film in a supercell [56] as:

$$Abs(\omega) = \frac{\omega L}{c}\,\mathrm{Im}\{\varepsilon^M(\omega)\} \quad (2.51)$$

where c is the speed of light and L is the size of the supercell in the direction perpendicular to the axes of the surface. As a support to the absorbance, the spectral intensity can be defined as the probability, given a particular transition of frequency ω_i, for an excitation between two states, one in the valence band and the other in the conduction band, to occur. This probability can be calculated from the transition dipole matrix element

calculated from the macroscopic dielectric function under the IP-RPA approximation as:

$$S(\epsilon_{cv\mathbf{k}}) = f_{c\mathbf{k}} f_{v\mathbf{k}} w_{\mathbf{k}} W_c W_v \left| \langle c, \mathbf{k} | \hat{\mathbf{p}} + i\left[\hat{\mathbf{r}}, V^{NL}\right] | v, \mathbf{k} \rangle \right|^2 \tag{2.52a}$$

$$\epsilon_{cv\mathbf{k}} = \epsilon_{c\mathbf{k}} - \epsilon_{v\mathbf{k}} \in (\omega_i - \delta, \omega_i + \delta) \tag{2.52b}$$

where $f_{v\mathbf{k}}$, $f_{c\mathbf{k}}$ are the electron/hole occupation of the valence/conduction state given by the Fermi-Dirac distribution, $w_{\mathbf{k}}$ is the weight of the k-point and W_i are the weighting coefficients introduced for the Eq. 2.50. The parameter δ has been included as a broadening for the transition energies. From the above equations, the cumulative spectral intensity $s(E)$ can be calculated as a summation over k-points, while the k-resolved spectral intensity $S(\mathbf{k})$ can be calculated as a summation on all contributing pair of states for a fixed k-point. Therefore the two quantities can be written, introducing the Gaussian functions $G(E, \epsilon_{cv\mathbf{k}}, \sigma)$ centered in $\epsilon_{cv\mathbf{k}}$ with broadening σ, as:

$$S(E) = \int \mathrm{d}\epsilon_{cv\mathbf{k}}\, S(\epsilon_{cv\mathbf{k}}) * G(E, \epsilon_{cv\mathbf{k}}, \sigma) \tag{2.53a}$$

$$S(\mathbf{k}) = \sum_{\epsilon_{cv}(\mathbf{k})} S(\epsilon_{cv\mathbf{k}}) \tag{2.53b}$$

A second macroscopic quantity that will be looked into is the reflectivity. In the case of a thin film, a straightforward application of Snell's law for the refractive index cannot be carried out, as the experimental techniques would probe a region of the sample much thicker than the slab inserted in the computational supercell. Therefore the electronic response of the bulk must be included without actually having to enlarge the slab: one of the possible approaches is represented by modeling a real three-dimensional system as three coupled regions [57, 58], namely the vacuum, the bulk and in between the interface of interest. This approach exploits the reflection (in this case through Snell's equations) at each of the two surfaces separating the regions; at the vacuum-slab interface there will be the superposition of the reflected wave at such surface with the one that has been reflected at the slab-bulk interface, which has been transmitted through the slab region. At normal incidence the equations can be further simplified, although only a differential quantity, called surface differential reflectivity spectroscopy (SDRS), can be reconstructed as the modification $SDRS(\omega) = (R_{ads} - R_{clean})/(R_{clean})$ of the absolute reflectivity of the clean surface induced by the formation of the interface with the adsorbate. In this way the reflectivity would read:

$$SDRS(\omega) = \frac{4\pi L}{c}\left[A\Delta\varepsilon'' - B\Delta\varepsilon'\right] \tag{2.54a}$$

$$\Delta\varepsilon = \varepsilon_{adsorbate} - \varepsilon_{clean-surface} \tag{2.54b}$$

where ε', ε" are the two components of the complex dielectric matrix and A, B are two functions representing the contribution of the bulk as:

$$A(\omega) = \frac{\varepsilon'_{bulk} - 1}{\left(1 - \varepsilon'_{bulk}\right)^2 + \left(\varepsilon''_{bulk}\right)^2} \tag{2.55a}$$

$$B(\omega) = \frac{\varepsilon''_{bulk}}{\left(1 - \varepsilon'_{bulk}\right)^2 + \left(\varepsilon''_{bulk}\right)^2} \tag{2.55b}$$

2.5 Configurational Ground state

Thanks to the adiabatic approximation discussed at the beginning of the chapter, the atomic coordinates could be assumed fixed during the solution of the electronic problem. The configuration can often be constructed from a guess on the geometry, followed by the optimization on the coordinates of the ions based on the actual forces developed in the system. The ground state for the atomic degrees of freedom can be calculated through different methodologies, in which forces are calculated from first-principles through Hellmann-Feynmann theorem [59] as $\mathbf{F}_i = \delta E[\rho](\mathbf{R})/\delta \mathbf{R}_i$ and minimized. The simplest case is a relaxation, namely when the system is close to its ground state configuration, therefore the optimization can evolve following the gradient of the energy. However, the guess on the geometry can be far from the ground state or even not known; the exploration of the potential energy surface (PES) $E(\mathbf{R})$ can be a complex task [60]: there are several degrees of freedom and the properties of the PES cannot be calculated analytically. To overcome such a limitation, several approaches can be followed; among those, two are the ones which will be exploited in this thesis' work and will be described with more detail in the following: the first approach consists in giving some energy to the ions and letting them move, namely as a molecular dynamics (MD) simulation. The second one, instead, is based on genetic algorithms [61–63], namely a constrained iterative process in which a set of random initial configurations is evaluated and mated through a suitable transformation.

2.5.1 Molecular dynamics

In this kind of simulation, the ions are moved by solving Newton's equations; the kinetic energy introduced into the system by raising the temperature may allow to overcome small potential energy barriers between two configurations. Several algorithms can be applied to propagate the forces into the ionic motions via discrete time steps Δt; in this

work the velocity Verlet algorithm [64] has been exploited, as implemented in QuantumESPRESSO, which standard form reads:

$$\mathbf{x}_i^{n+1} = \mathbf{x}_i^n + \Delta t \mathbf{v}_i^n + \frac{\mathbf{F}_i^n (\Delta t)^2}{2m_i} \tag{2.56a}$$

$$\mathbf{v}_i^{n+1} = \mathbf{v}_i^n + \frac{\left(\mathbf{F}_i^n + \mathbf{F}_i^{n+1}\right)\Delta t}{2m_i} \tag{2.56b}$$

If the system is closed, namely the is no exchange of particles nor energy with any surrounding environment, the total energy must be conserved: in this case statistically the system is called an NVE ensemble, in which also the volume is conserved. The calculation has to be verified to conserve the energy, by carefully choosing the proper value for ΔT in which the forces do not change substantially. More practically, the temperature is the parameter that is kept fixed, analogously to what happens commonly in experiments; in this case the system is called an NVT ensemble and the temperature needs to be controlled via a proper thermostat. The boundary conditions of the motion are set by extracting the initial velocities of the particles from a proper distribution; each step the temperature has been conserved through a velocity-scaling algorithm [64], via a renormalization of the distribution of velocities.

2.5.2 Genetic algorithms

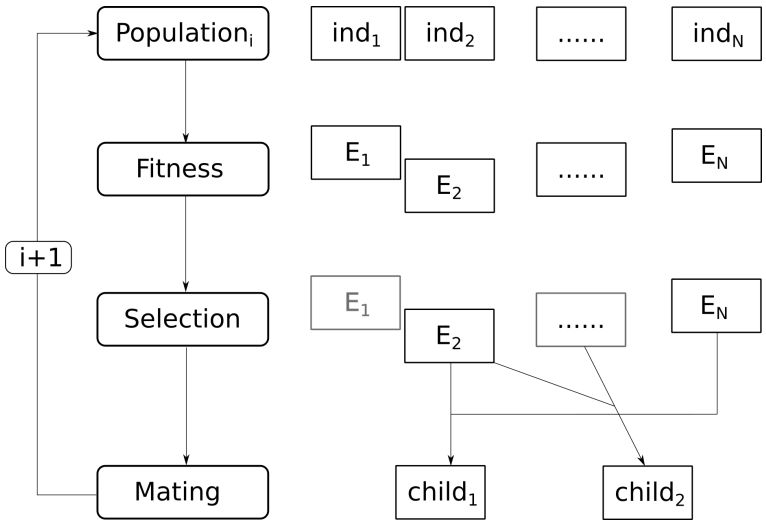

Figure 2.2: Representation of the main logical loop in a genetic algorithm.

In this approach, in analogy to the biological process, the ground state of the atomic configuration is searched by means of converged evolution [60, 65–67], which is sketched in Fig. 2.2, by the use of ASE python module [68]. The basic idea is that by repeatedly

selecting and mixing the coordinates of the most stable configuration, it is possible to have the process converging onto the (true) most stable geometry. The process starts with constructing the initial population, which must be large enough to allow for enough diversity in the configurations; in the work described here, the geometries have been constructed by collecting atoms at random coordinates within an user-defined region in the supercell. In this way some constraints, namely thickness, number of atoms or even symmetry, can be enforced in the configurations. In a second step, the fitness of all the individuals is evaluated simply as the total energy of a DFT relaxation, with the fittest being the most stable ones: a population of parents is then constructed by selecting a restricted group among the initial one. Then, the parents are mated to construct a population of children; this is done by splicing the coordinates [69], namely defining a cutting plane in the two configurations and taking half of the atoms from each parent. Again, the size of the parents' population and the offspring is important to avoid genetic stagnation, if too small. Finally, the population of children is promoted as the new starting population and the next iteration can begin.

Chapter 3

0D: Pentacene on Pt(111)

3.1 Introduction

Aromatic molecules are nowadays a widespread building block in the production of opto-electronic devices [70, 71], like light emitting diodes or organic thin-film transistors, as they can profit from a large number of large scale and industrial-grade techniques for their synthesis and the growth of an active layer within a device. Therefore, such compounds can allow the production of devices possessing novel properties at lower costs the traditional silicon-based processes [72, 73]. It is extremely important to fully characterize the interface formed in presence of the metallic surface, as it will act as a pattern for the growth of the organic layer and it governs the alignment of the energy levels. Among the many molecules that can be taken into account, aromatic molecules have attracted much attention, in particular pentacene (Pc, $C_{24}H_{12}$) and its derivatives have been widely employed [71, 74] thanks to their high charge-carrier mobility in their bulk phase [71, 75]. Moreover, Pc can be seen as a prototype of Π-conjugated system where the length of the molecule can be sufficient to unlock additional degrees of freedom. On the other end, platinum (Pt) forms high work function surfaces, the value of which is similar to the energy of the highest molecular orbital (HOMO) of Pc molecule [73, 75]; their coupling can therefore form a junction with low charge-injection barrier, and some devices based on such materials have already been fabricated [76, 77]. Moreover, Pt is one the most reactive metals among those of technologic relevance like gold or aluminum, thanks to its unfilled s and d states, and Pt surfaces are a known catalyst. The interface between Pc and Pt is expected to show the effects of a strong interaction between the surface and the molecule, therefore attracting interest not only from the point of view of a possible application, but also from an atomistic perspective, in which such a system

can be employed as a benchmark on some of the most recent developments in terms of long-range interactions. As described in the previous chapter, section 2.2, several approximations and flavors are available, the choice of which depends on the desired level of accuracy.

The smallest aromatic molecule, benzene (C_6H_6) has been already thoroughly investigated both in gas phase and adsorbed on different metals [78–82], which however could not address any geometrical effect, for example distortions of the aromatic ring, because of its single-ring structure. Regarding Pc, the formation of several thin-film phases have already been reported on several coinage metals [83–86], where the relaxation of polyconjugated aromatic hydrocarbons is driven by the maximization of the overlap of the molecular orbitals with metallic states at the surface in the vicinity of the Fermi energy. For weaker interactions, such as in gold or silver substrates, the formation of different phases is triggered by different molecular coverages, pointing to a molecule-to-molecule interaction comparable with the one with the surface [85,87–90]. In particular, on the reconstructed (1×2)-Au(110) surface the adsorption is driven more strongly by the anisotropy of structure of the substrate [83,91]. In the case of stronger interactions, on Cu surfaces [92], the Pc shows a slightly bent adsorption configuration, along with a vertical displacement (called buckling) of the atoms of the surface. Along with geometrical modifications, the coupling of the molecule with the substrate is accompanied by the hybridization of their respective electronic states, namely their density of states are broadened and shifted, effectively pointing to a chemisorption picture [84,93,94]. In case of the Al(001) surface [86,95], the interaction is catalyzed by the central carbon atoms of Pc, resulting in a V-shaped molecule at most of the adsorption sites.

The goal of the study described in this thesis was to fully characterize the adsorption of Pc onto the Pt(111) surface by both experimental and theoretical means, through several techniques as STM, XPS and NEXAFS, accessible to our collaborators. A first set of preliminary results, which will be briefly resumed shortly after, was obtained during the Master's thesis [96], which was focused on the adsorption geometry; the study has been later expanded by investigating the excited states of the system through measured and simulated core hole spectroscopies. This latter part is the actual goal of the project included in this thesis.

Computationally, the system has been constructed as a slab with a 7×4 repetition of the Pt(111) unit cell, including three layers of Pt, where the topmost one has been left free to relax in order to mimic the behavior of the bulk. A vacuum region of 14 Å has been included in the supercell on top of the surface to reduce the interaction of the slab with its replica. However, such size is not large enough to restore the proper

boundary conditions for the electrostatic potential along the direction perpendicular to the surface, therefore a saw-tooth electric field [97] has been added in the vacuum region, the magnitude of which has been calculated based on the actual charge distribution of the system. The Brillouin zone has been sampled by a 2×3×1 k-points grid, off the Γ point. The DFT scheme has been solved using the PBE exchange-correlation functional and ultrasoft pseudopotentials, which properly described the ground state with a cutoff of 31 Ry on the wavefunctions and 321 Ry on the charge densities. The metal has been constructed using a lattice constant $a_0 = 4.00$ Å, obtained through the minimization of the energy-volume curve, larger than the experimental value $a_0 = 3.92$ Å [98], as expected from the PBE functional. For additional details about this investigation, the results of this project are collected and discussed in Ref. [99].

3.2 Adsorption properties

I recall here the results of the preliminary investigation on the Pc/Pt(111) system, which have been focused on the adsorption configuration has been explored by optimizing different sets of initial coordinates, differing by the position of the center of the molecule with respect to the lattice of the surface and their relative orientation. The role of the inclusion of diverse dispersion terms has been thoroughly investigated, by incorporating additional van der Waals (vdW) components as Grimme-D2, vdW$_{surf}$ [100,101] or non-local vdW$_{nl}$ functionals. In all these cases, the most probable adsorption site found in the calculations is in between two Pt atoms, along their bonding direction (the so-called bridge site), with the long molecular axis oriented along the lattice vector of the surface. Such configuration, labeled 'bri0', is reported in Fig. 3.1. The adsorption energy for the same site is strongly dependent on the flavor of vdW correction accounted for in the simulations: without any long-range term (i.e. only PBE) the value is notably smaller than the others, suggesting that the substrate is highly interacting through deeper layers of the slab. However, the D2 term strongly overbinds the molecule, which can be tracked down to the static atomic coefficient embedded in the method itself. In between, the dynamic pairwise term (vdW$_{\mathrm{surf}}$ and the non-local functional term (vdW$_{\mathrm{nl}}$) are in good agreement, indicating the need for an electronic coupling based on the actual charge configuration. The changes of the electronic properties of the molecule upon adsorption have been investigated by calculating the difference of spatial distributions of the charge density between then final configuration and the isolated ones $\Delta\rho = \rho_{Pc/Pt} - \rho_{Pt} - \rho_{Pc}$, as reported in Fig. 3.1. The structure of the lobes suggests the formation of bonds between C and Pt atoms; this hypothesis is further confirmed by investigating, at the bri0

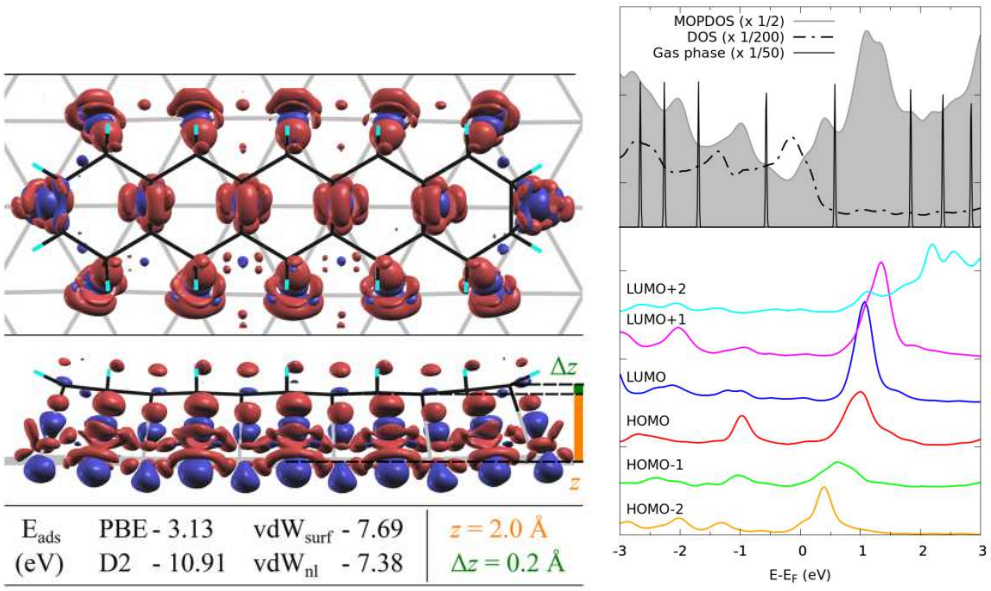

Figure 3.1: Left panel: schematic representation of Pc molecules adsorbed on Pt(111) in the 'bri0' configuration. The molecular carbon backbone is shown as black segments, while the surface lattice is shown as gray ones. Top and front view of the configuration are reported. In the lower panel, the adsorption energy for different vdW terms is reported, as well as the geometrical details, namely the average bond length z and the buckling Δz of the Pc. The distribution $\Delta\rho$ is shown as red/blue lobes corresponding to the isovalue of 0.01 e/Bohr^3. Right panel: DOS of the system and projection on the molecular orbitals (MOPDOS). The contribution of selected atomic orbitals of gas phase Pc is reported along the energy spectrum of the states.

site, the density of states (DOS) of the full system and its projection along the orbitals of the molecule (MOPDOS), which are reported in Fig. 3.1. The contributions of gas phase orbitals of Pc are spread all over the energy spectrum of the DOS, indicating a strong hybridization of Pc states with the ones of the surface. By further processing the charge densities by the means of Löwdin analysis [102], it has been possible to estimate that the molecule gains $\simeq 1.5$ e$^-$ through adsorption.

The results of the simulations find a confirmation with room temperature STM experiments, which have been carried out by ESISNA group at ICMM-CSIC in Madrid. In the low-coverage limit, which is reported in Fig. 3.2(a), it is possible to identify the molecules as individual straight lines, the length of which is $\simeq 2$ nm, oriented along three different directions. Such three-fold symmetry corresponds to the Pt lattice $[10\bar{1}]$, $[01\bar{1}]$ and $[1\bar{1}0]$ directions, as confirmed by tunneling-enhanced close up, shown in Fig. 3.2(d-e). As a

full monolayer is grown, as shown in Fig. 3.2(b), the formation of a disordered film is observed, suggesting that the interaction of the molecule with the substrate is stronger than the intermolecular one and strong enough to prevent its further diffusion on the surface. This reason explains the formation of small clusters of second-layer molecules before the monolayer is fully completed. Such a strong interaction of organic molecules on Pt(111) surface is already known in literature as adsorbed hydrocarbons have been seen to led the formation of graphitic domains [103]. By zooming in on isolated molecules and extracting the eight profiles of their charge distribution it is possible to measure the buckling of Pc, which is in good agreement with the result of the calculations for the bri0 configuration, for isovalues corresponding to isosurfaces which are at least 2 Å apart from any atom and within a broadening of 0.1Å.

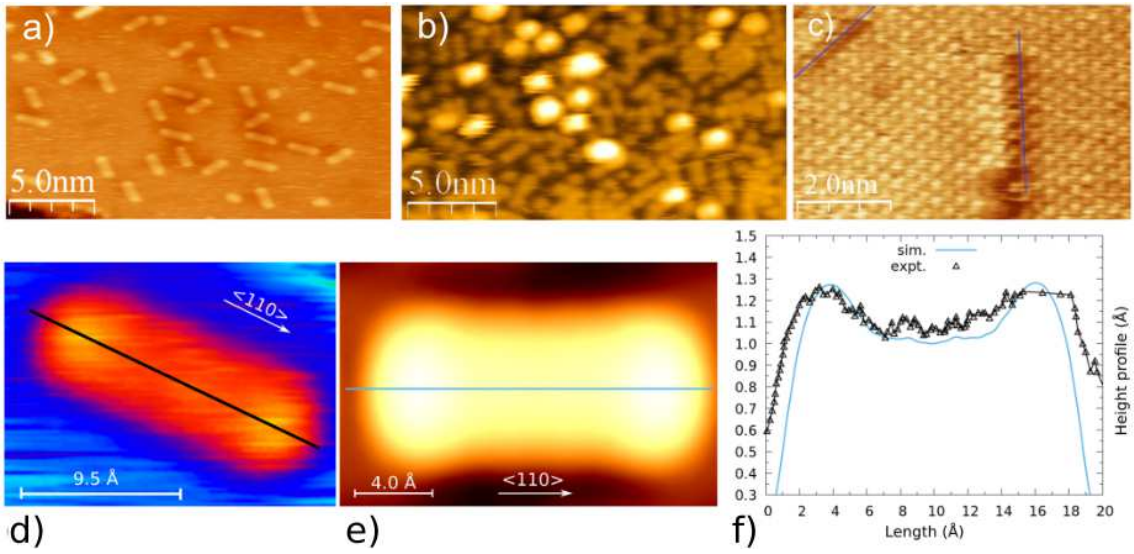

Figure 3.2: Experimental STM images of Pc/Pt(111). Panels a),b) report the low and $\simeq$ 1 ML coverage imaging, respectively (sample bias 1 and 1.5 V, respectively, 25 nm $\times$ 12.6 nm). Panel c) reports the tunneling-enhanced zoom on an isolated molecule, in which the lattice of the surface can be identified (sample bias 0.5 V). Panel d) reports experimental high-resolution imaging (sample bias 0.5 V, 0.396 nA tunneling current). Panel e) reports the simulated data for the bri0 configuration. Panel f) shows the comparison between the experimental height profile with the one simulated (for the same bias) for the bri0 configuration. The data is extracted from the scanning along the lines reported in panels d) and e).

3.3 Spectral properties

From the results collected above, the chemisorption of a molecule on the surface can be suggested, but not strictly proven. In order to finally verify such hypothesis, an investigation of the different chemical environments and the empty states of the system has been carried out, by the means of XPS and NEXAFS spectroscopies. The photon absorption has been focused onto the carbon K edge; the experiments have been carried out by our collaborators at the ALOISA beamline of the ELETTRA synchrotron facility in Trieste (Italy) [104]. The deposition of the molecules has been monitored through a quartz microbalance, allowing to define the nominal coverage of 1 ML corresponding to a 2.5Åthick film. The XPS spectrum was recorded at three coverage steps, namely the sub-monolayer (0.6 ML), the monolayer and 5 ML. NEXAFS spectra were instead recorded at 1 ML and 5 ML. In both cases, the sample was further annealed by heating it up to 130 °C. From the computational point of view, the two spectra have been calculated through full core hole and half core hole pseudopotentials generated within the norm-conserving formalism, which required an higher cutoff of 62 Ry and including the PAW reconstruction of the all-electron wavefunction. XPS spectra have been constructed by broadening the delta-like contributions of the different core level shifts (CLSs) with a pseudo-Voigt scheme, applying a Gaussian profile with σ 0.38 eV and a Lorentzian one with width γ 0.17 eV, mixed by parameter the value of which is 0.47. These values have been obtained by fitting the experimental data. NEXAFS spectra have been constructed using the XSpectra package [44] included in the QuantumESPRESSO distribution, through a broadening based on an energy-dependent scheme [105] with a width γ of 0.2 eV for energies up to $E_F + 5$ eV, γ=1 eV for energies above $E_F + 25$ eV and a linear dependence in between, in order to mimic the effect of vibrational contributions.

The XPS spectrum has been calculated for the two most stable configurations, the bri0 and the so-called fcc0, which differ by the position of the center of the molecule; the results are reported in Fig. 3.3 along with the experimental data for the nominal coverage of 1 ML. At first inspection, the bri0 case, as suggested by the adsorption energy investigated in the preliminary results, is in much better agreement with the experiments, corresponding to the most stable configuration. Because of this comparison, further investigations will be carried out on the bri0 case only. The XPS spectrum shows two close but resolved peaks at the binding energy of 284.25 and 284.75 eV respectively, which are originated by two groups of CLSs components calculated by the simulations. The spectral shape found here is different from the one reported for a

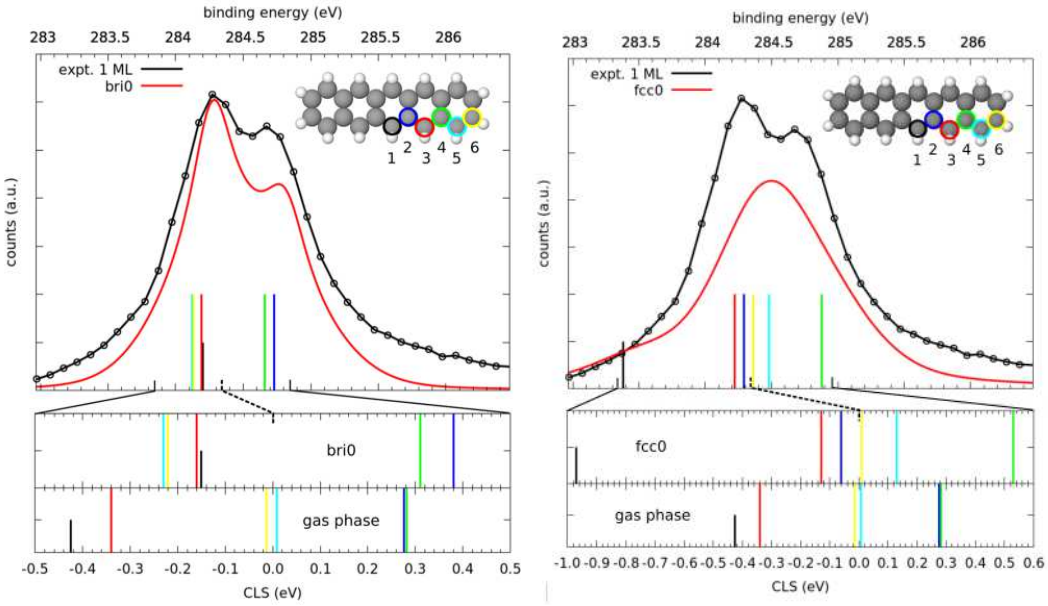

Figure 3.3: Experimental and simulated XPS spectra for the two most stable configurations: bri0 (left panel) and fcc0 (right panel). The number of the inequivalent carbon atoms and the relative colors are reported on top of each plot. At the bottom of both panel, the individual CLSs are compared between the adsorbed case and the gas phase values.

gold substrate [83] but is in better agreement with those reported for Pc adsorbed on Cu [106, 107] or on Al [95]. The carbon atoms with a similar CLS are C1, C3, C5 and C6, which are the one bound to H atoms, and C2, C4 which are bound to C atoms only. It is possible to associate the former group of C atoms which are assuming an sp^3 hybridization scheme for their atomic orbitals and the latter one corresponding to sp^2 hybridization. The comparison with the CLSs of the molecule in gas phase helps also to highlight the influence on the photoionization due to the adsorption on the metal, namely the charge transferred to the molecule and the image potential created by the surface. Recalling the description of ΔSCF method given in the Sect. 2.4.1, the former effect results in smaller CLS, while the latter effect results in larger CLS. Since the use of pseudopotential doesn't allow for an absolute comparison of the calculated CLS, it can be useful to fix the CLS of C2 and C4, which can be thought as less reactive that the others; in this way C1 and C3 would be shifted to more negative CLSs, while C5 and C6 contributions would be shifted towards more positive CLSs. Such result is in agreement with what is expected theoretically as C1 and C3 are the atoms most involved in the chemical reactivity of the molecule [108, 109], while C5 and C6 would be mostly

experiencing the effect of the surface, thanks to the almost planar adsorption geometry of the molecule. The CLSs calculated for the bri0 configuration are reported in Table

Atom	CLS^{IS} (eV)	CLS^{FCH} (eV)
C1	-0.29	-0.13
C2	0.69	0.38
C3	-0.31	-0.14
C4	0.59	0.31
C5	-0.47	-0.21
C6	-0.21	-0.20

Table 3.1: CLSs calculated for the Pc adsorbed on Pt(111). The different approaches in calculating the CLS are reported: the initial-state one (IS) and the use of a full core hole pseudopotential (FCH).

3.1, for both the initial state approach and the full core hole pseudopotential described by Eqs. 2.23, 2.24 respectively. Such comparison allows for the evaluation of the effect of fully relaxing the Kohn-Sham eigenvalues in the presence of the core state: in the majority of the atoms an important reduction of the CLS can be observed. The agreement with experimental and the simulated XPS spectra is indeed not perfect. In particular the relative intensity of the two main peaks in not well reproduced and there is a tail of counts at higher binding energies which cannot be accounted for just changing the broadening of the CLS contributions. As for the latter, a residual CO contamination can be addressed [110], coming from the heating filament inside the Pc crucible. Such component can be identified from the comparison of XPS spectra at different coverages shown in Fig. 3.4, where it disappears after the annealing steps. The former discrepancy, instead, cannot be addressed by considering the formation of a mixture of bri0 and fcc0 phases, nor by the effect of second layer clusters. Such stacking effects are observed in STM but those molecules are desorbed after the annealing as well, which can be observed in Fig. 3.4, too. Instead, by further inspecting the STM images it is possible to recognize smaller molecules, possibly shorter acenes, which are found as contaminants in Pc powder. The XPS of such molecules could ideally be constructed by removing to the Pc/Pt(111) spectrum the contribution of some of the CLS from the carbon atoms which would not be present in a shorter molecule, as C1 or C5 and C6. Therefore the majority of the remaining contributions would come from atoms like C2 or C4, thus changing the relative intensity of the peaks.

Moving to the investigation of the conduction band of the system, the NEXAFS

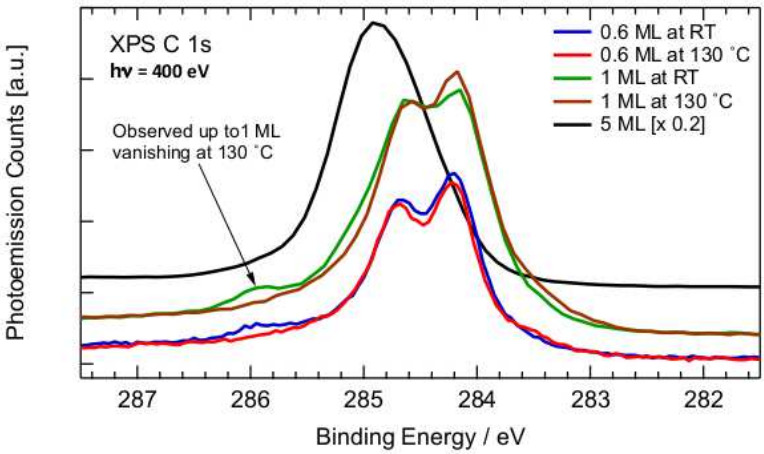

Figure 3.4: Experimental coverage-dependent XPS spectra. The effect of multi-layer stacking can be evaluated by comparing the spectra before and after annealing and the multilayer spectrum.

spectra are reported in Fig. 3.5; the agreement with the simulated spectrum and the experimental data is good. The photon absorption has been measured at two different polarization vectors, with respect to the surface: in-plane (labeled 's') and out-of-plane (called 'p'). In the results, two broad structures can be seen around 286.5 and 292.5 eV for the two polarizations, respectively: this energy splitting, or dichroism, has already been reported in literature [111,112] and is to be expected in the case of planar aromatic molecules. In fact, in the electronic structure of a conjugated system, like Pc, the atomic orbitals of C atoms are organized through an sp^2 hybridization, forming a characteristic bonding-antibonding structure. Its molecular orbitals, in case of a planar structure, are structured with a lowest-lying unoccupied Π^* system, made mainly by electron delocalized onto atomic p_z orbitals, followed by the less bound Σ^* system. The observed dichroism confirms, along with the high intensity ratio of the p component over the s one, that the Pc molecules are adsorbed mainly in a planar fashion, as predicted by the bri0 configuration. Focusing onto the p-polarization spectrum, the plot shows a resolved structure, with two broad peaks at $\simeq$ 285 and 287 eV which are well described by the simulated data, which we would be tempted to associate with excitation of the core electron into one of the molecular orbitals, for example a LUMO or LUMO+1 states, as has been done in gas phase [95, 112]. However, as suggested from the hybridization of such orbitals with Pt states seen in the previous section, a similar correlation has to be ruled out. Actually, this fact can be easily shown by investigating the NEXAS component calculated for each inequivalent carbon atom, which are shown in Fig. 3.6. The two

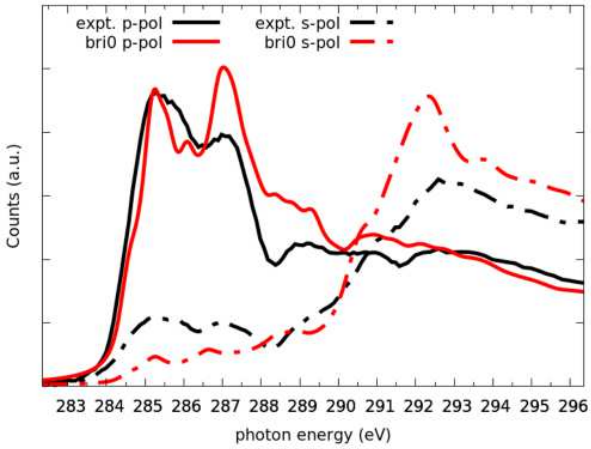

Figure 3.5: Experimental and simulated NEXAFS spectra, for the in-plane(s) and out-of-plane(p) polarization.

peaks which are observed in the spectra are actually due to the contribution of different C atoms, in particular the feature closer to the edge of excitation edge gets contributions from all C atoms, while the feature at higher energy is contributed only from C2, C4 and C6. These results finally prove the strong modifications of the electronic structure of the molecules given by their adsorption on the metal surface. In can be noted that, even in NEXAFS spectra, the agreement of simulated results with experimental data is not perfect and there is a discrepancy in the relative intensities of the two main peaks within the p polarization, as well as e different p-to-s ratio. Similarly to the XPS spectroscopy, this fact can be ascribed to the role of shorter acenes: such molecules would show a NEXAFS spectrum possibly without a C6 or even a C4 component. In p-polarization, these atoms are seen to contribute strongly to the higher energy peak; therefore the remaining atoms would lift the intensity on the lower-energy feature, therefore changing the spectral shape in better agreement with the experiments.

3.4 Conclusions

Theoretical modeling of excited state properties has been successfully carried out in order to investigate the electronic properties of a hybrid metal-organic molecule interface: in particular the changes induced by adsorption. Several evidences pointing our a strong interaction between Pc and Pt(111) have been thoroughly evaluated, such as the formation of bonds and the charge transfer at the interface. Such a chemisorption picture has been verified by inspecting the chemical environments and the conduction

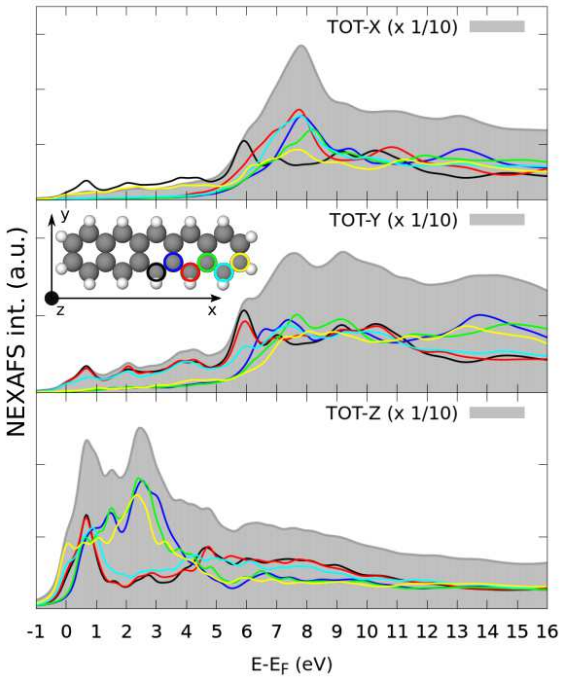

Figure 3.6: Contribution of the inequivalent carbon atoms to the simulated NEXAFS spectra, for excitations along the three cartesian axes. The correspondence of between the colors of the spectra and the C atom for which the spectrum has been calculated is given by the inset in the middle panel.

band structure through the modeling of the core hole excitation as measured in experimental XPS and NEXAFS spectroscopies, focused on the carbon K edge. In the former technique, the fingerprint of the sp^2 to sp^3 re-hybridization has been observed, as well as the role of adsorption-related effects, i.e. the charge transfer and the screening from the surface. In the latter technique, the effect of the hybridization of the molecular orbitals with the Pt states has been observed. In both cases, the results confirm the adsorption configuration, namely site and geometry, found by previous simulations as the one called 'bri0' and observed with STM measurements.

Chapter 4

1D: Carbon chains sp^1/sp^2

In the previous study, the fingerprints of the hybridization of carbon atoms have been identified in an isolated molecule by the means of core hole spectroscopies. The target on this investigation is the identification of similar features for the case of mono-dimensional system as the linear chains of carbon atoms, which are the archetype of sp^1 hybridized organic compounds. The near-edge x-ray absorption fine structure (NEXAFS) spectrum of organic molecules with C atoms with different hybridization states will be investigated with theoretical models based on ideal systems, especially in the case of an hybrid interface, to identify unique spectral features which allow the experimental discrimination of the chemical state. My contribution to this project was mostly in providing analysis tools and investigating the results; therefore I will only briefly introduce its results. For further reading, the complete discussion is collected in Ref. [113].

After the discovery of graphene, the investigation of carbon allotropes focused also on carbynes, i.e. infinite carbon chains based on sp^1 hybridization [114–119]. Despite the interesting properties predicted by several theoretical calculations [120,121], stability issues in the synthesis of carbynes deemed such process unlikely [122]. Nevertheless, more recent achievements in chemical and physical processing of carbon compounds allowed to include finite size carbon chains into larger nanostructures [123–129]: such systems have been experimentally imaged by the means of STM or atomic force (AFM) microscopies, effectively resolving single atom wires [130–132]. These techniques, however, cannot give additional insight about the chemical state of C atoms, nor about the interaction with the substrate, which are instead the main target of NEXAFS spectroscopy.

In this work, the electronic and spectral properties of a prototype of such systems, obtained by polymerization of the (4,4'-di(bromoethynyl)-1,1'-biphenyl, bBEBP) molecule, are investigated by theoretical means through (half) core hole absorption methods. The

interface between the polymer and the Au(111) surface is taken into account: its structure, as constructed in the simulations, and the simulated NEXAFS spectrum are reported in Fig. 4.1. Several features can be observed in the spectrum, most notably a broad peak at $\simeq$ 2 eV for polarization along z axis and two sharp peaks at around 2 eV and 5 eV for the polarization along y axis. It is possible to address the origin

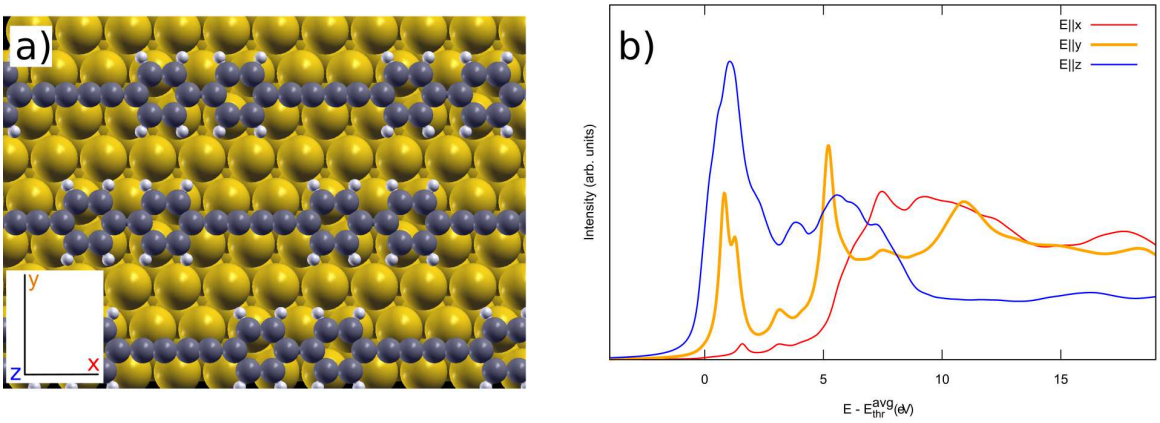

Figure 4.1: Structural model (left panel) and NEXAFS spectrum of the bBEBP polymer deposited on Au(111). Images adapter from Ref. [113].

of these absorption peaks by investigating the band structure of the system, which is reported in Fig. 4.2, in particular the projections on the atomic orbitals belonging to the linear chair of four atoms (labeled C4) and to the phenyl groups (labeled BP). Three almost flat bands can be observed around 2 eV above the Fermi energy that can be directly associated with the LUMO+1, LUMO+2 and LUMO+3 molecular orbitals. Their shape, reproduced in the same figure, indicate that such states belong uniquely to C4 (first band) or BP (second and third band), independently from the interaction with the metal surface. This orbital localization can be exploited to address the fingerprint of the different chemical environments of carbon in the NEXAFS spectrum.

To investigate the C4 region of bBEBP, the ideal chain of single C atoms is modeled both as cumulenes, which is a sequence of equal double C-C bonds, or as polyynes, in which C-C bondlengths alternate in a sequence of single and triple bonds. The calculated band structures and spectroscopic properties are collected in Fig. 4.3. In both cases, the lower lying states in the conduction band are originated from antibonding states with p_y and p_z symmetry, which explains the strong dichroism observed in NEXAFS spectra for the corresponding components with respect the one related to polarization along x direction. In particular for polyynes, the absorption shows a sharp onset, related to

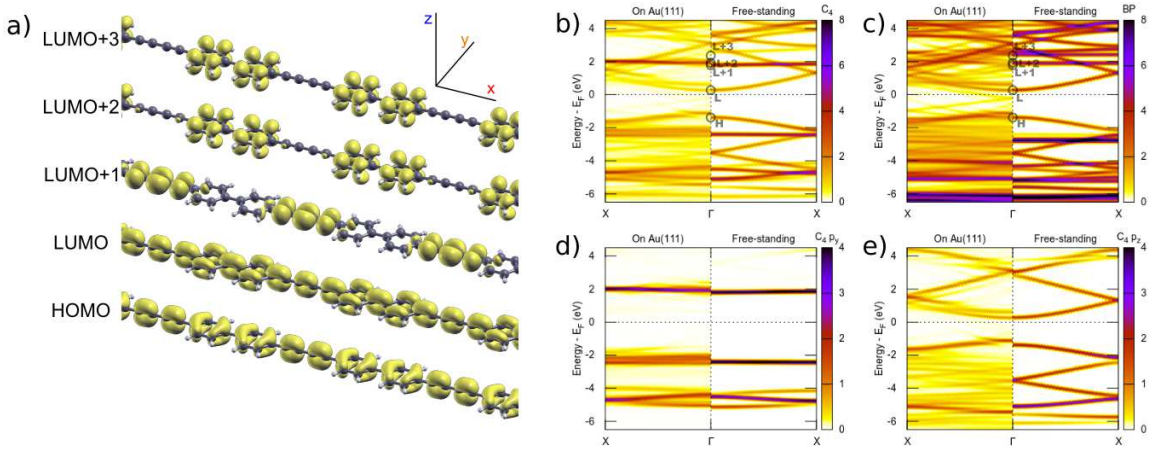

Figure 4.2: Panel a): spatial representation of the molecular orbitals of free-standing bBEBP polymer around Fermi energy (Isosruface=0.01Å^{-3}) The wave amplitude of the LUMO of the isolated C_4H_2 fragment is shown at the bottom. Panels b), d), e): band structure of bBEBP/Au(111) projected on the C4 section and on the C4 p_y, p_z orbitals. Panel c) reports the same band structure projected onto BP atomic orbitals. In all panels the comparison between the free-standing bands and the adsorbed ones is shown. Images adapter from Ref. [113].

the different band structure in the vicinity of the Fermi level, which is compatible with the sharp peak observed in bBEBP/Au(111) for the same polarization. To investigate

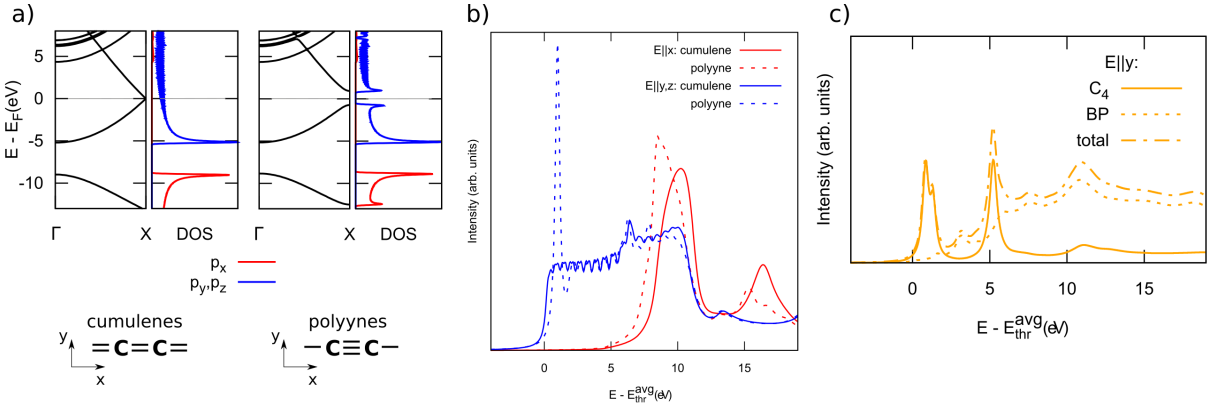

Figure 4.3: Calculated electronic properties (a) and NEXAFS spectra (b) of ideal infinite sp^1 carbon chains with different orbital pairing. The decomposition of the calculated bBEBP/Au(111) NEXAFS spectrum onto its C4 and BP parts is reported in c) for the x-ray polarization along y axis. Images adapter from Ref. [113].

instead the absorption of sp^2 C atoms from the phenyl rings of the polymer, the model of

an infinite chain of poly(p-phenylene) rings has been constructed, as shown in Fig. 4.4. The related NEXAFS spectrum is characterized by a sharp peak, close to the absorption

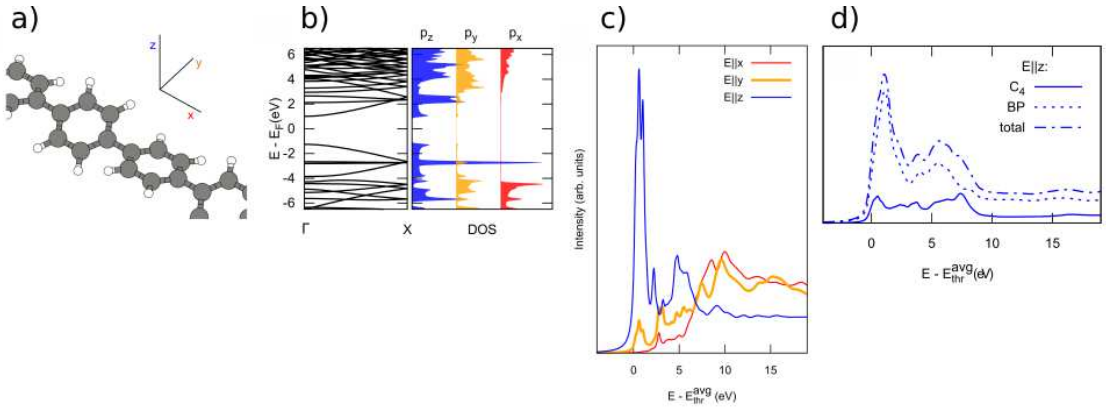

Figure 4.4: Structural model of the free-standing poly(p-phenyl) chain (a). In (b) its band structure and DOS, projected onto p_i orbitals is shown. Panel c) reports the calculated NEXAFS spectra, along the three cartesian directions. Panel d) shows the decomposition of the calculated bBEBP/Au(111) NEXAFS spectrum onto its C4 and BP parts for the x-ray polarization along z axis. Images adapter from Ref. [113].

edge, in the z-polarized component, which can be directly related to the lower-energy conduction band states, which posses p_z symmetry. This feature is in good agreement with the spectral shape, for the same polarization, calculated for the absorption of the atoms of the BP component of bBEBP/Au(111).

In conclusion, a monodimensional system, namely a nanostructured organic compound of recent synthesis possessing mixed sp^1/sp^2 hybridization, has been investigated by theoretical means through core hole calculations within the DFT framework. The spectral features of its polarized NEXAFS spectrum with polarization along or orthogonal to the support used for growth have been investigated, where it has been possible to address unique fingerprints of both sp^1 or sp^2 C hybridization through the comparison with prototypical case studies.

Chapter 5

2D: Functionalized Silicene on Ag(111)

5.1 Introduction

Despite a theoretical modeling of the electronic properties of atomically-thin, two-dimensional, graphite structure has been known since several decades [133, 134], the onset of thermo-dynamical instabilities prevented the synthesis of a graphene layer for many years [135]. Once such samples could be grown, several unique properties could be investigated, for example a high charge carrier mobility [135, 136] or the opportunity to deal with quantum effects [137, 138], which are related to the two-dimensional honeycomb structure of the system. Given the great innovation potential in the field of opto-electronics, much research efforts have been spent to search for materials which could inherit the same features. As a natural extension of graphene, one of the first to be taken into account are those structures made of elements sharing a similar electronic structure, namely those in the same group in the periodic table, labeled Xenes [139]. Most notably, Si is not only the closest to carbon, but is one of the most important materials in current technology.

Theoretical investigations of free standing (FS) silicon two-dimensional self-assembled structures show not only the formation of the two-dimensional honeycomb geometry [140], called 'silicene', but also the inheritance of the electronic [140–142], optical [143–145] and topological effects [146, 147]. However, the synthesis of silicene proved more complicated than expected and, despite the number of suitable substrates fit for the proper self-assembly of Si atoms [139], a characteristic fingerprint of the formation of silicene hasn't been unequivocally detected. Focusing on silver surfaces, which are among

the first and most investigated ones, along the(111) facet several results from STM and LEED [148–150] or Raman [151]techniques suggest the formation of a silicene layer, although with a buckled structure which reconstructs as different phases. Nonetheless, the experiments probing the electronic structure, namely XPS and angle-resolved photoemission spectroscopy (ARPES), actually suggest a more complex picture where Si and Ag atoms strongly interact and their states hybridize and exchange charges [152]. More recently, such hypothesis has been further validated by experimental and theoretical means through either a combined STM/reaction pathway analisys [153] and an optical investigation [154, 155]. The former shows how a single Si adatoms are energetically pavoured to substitute Ag atoms of the surface, eventually forming islands; the latter instead addresses the formation of bonds at the interface between the Ag and Si layers. Tackling with the unoccupied states of Si in silicene may be a practical way to address tuning its interaction with a substrate, namely saturating Si dangling bonds through the chemical functionalization of silicene. Among the simplest modifications, the adsorption of single H or F atoms has been widely investigated from first-principles methods in the FS case [156–162]. Depending on the coverage, several H-passivated silicene phases have been reported in literature, in which the adatoms help stabilize the buckling of the Si atoms but actually do not weaken their reactivity [163–166]. Nonetheless, such regularization of the overlayer formed onto the surface can pave the way to an ordered platform to further processing [167].

This present work focuses onto the $\sqrt{7}\times\sqrt{7}/2\sqrt{3}\times2\sqrt{3}$R30° phase of silicene/Ag(111), which has been proven one of the most homogeneous configurations [168]. Three other passivation steps have been taken into account: the adsorption of a single adatom in the cell, an intermediate coverage, called 'half silicane' and the full passivated silicene, called 'silicane'. While for the latter the adatoms are bound to all Si atoms in an alternate fashion covering both the upper and the lower facet of silicene, in the former the adatoms cover only the lower surface of silicene, namely that facing the surface of the substrate. For every system, the ground state properties have been simulated by the means of DFT calculations, the results being compared with each other in order to highlight the effects of the change in both the degree of passivation and the chemical properties of the adatoms. In order to bridge theoretical insights with experimental measurements, optical excitations have been taken into account within the many-body perturbation theory framework, where the response of the system has been calculated through the independent-particle random phase approximation (IP-RPA). Among the goals of this study, there is to show that such techniques, which can be carried out in-situ for the

characterization of the sample, can directly probe the changes in the electronic structures which are normally interpreted through the assumption of a theoretical model. In particular the final target is focused on optical absorption and, more importantly, on reflectivity, obtained in terms of the surface differential reflectivity spectroscopy (SDRS), which may be the actual investigation method in case of a metallic surface.

The ground state calculations have been carried out with QuantumESPRESSO suite, using a norm-conserving pseudopotential with a kinetic energy cutoff of 86 Ry and a Grimme-D2 term accounting for the Van der Waals interaction. The system has been constructed as an asymmetric slab with five layers of Ag, the topmost two left free to relax; a vacuum region of at least 14 Å has been added on top of the surface to reduce the interaction of the slab with its replicas. The structure of the slab has been built using a lattice constant a_0=4.164 Å for bulk Ag, as obtained by minimizing the energy-volume curve. The Brillouin zone of the supercell has been sampled through an unshifted 6×6×1 k-points mesh, enlarged to 17×17×1 (31×31×1 for FS systems) for calculating electronic and optical properties. The Yambo code has been employed to process the ground state in order to calculate the macroscopic dielectric function, in this case with a cutoff on the wavefunction basis set of 44 Ry. For the calculation of absorbance and SDRS(see Eqs. 2.51 and 2.54a respectively), the value of the L in Eqs. 2.51 and 2.54a corresponds to 30 Å. All the optical excitations have been calculated at normal incidence, not only to obtain a better matching with experimental findings, but also to minimize the error introduced through the IP-RPA approximation [155].

5.2 Free standing silicene

5.2.1 Construction of the film

First the structure of the silicene layer has been investigated in the FS case, in particular the structure of the buckling of Si atoms, which will be later act as a pattern for introducing the adatoms. As already known from literature [140], a silicene layer can be formed with three different buckling configuration, depending the strain on the unit cell: planar (PL, without buckling), low buckling (LB) and high buckling (HB). The converged silicene system, constructed from the 1×1 cell with two inequivalent Si atoms, is calculated with a 12×12×1 k-points mesh, for which the resulting parameters are collected in Table 5.1. The two most stable configurations are the buckled ones, the energies of which are equivalent within the assumed numerical accuracy. Additional buckling patterns can be

Si configuration	ΔSi-Si (Å)	Δz (Å)	ΔE (eV)
PL	2.24	0.00	0.05
LB	2.27	0.47	0.01
HB	2.61	2.16	–

Table 5.1: Geometrical parameters and energetics of the optimized silicene 1×1 layer. ΔSi-Si is the first neighbor distance and Δz is the vertical displacement of the two atoms in the cell.

identified as the supercell is enlarged to a 2×2; these structures can be constructed by considering the possible combination of 'atom-low'/'atom-high' for all 8 atoms in the cell, as shown in Fig. 5.1. An example of the related configurations, labeled 'chair-like' (CL),

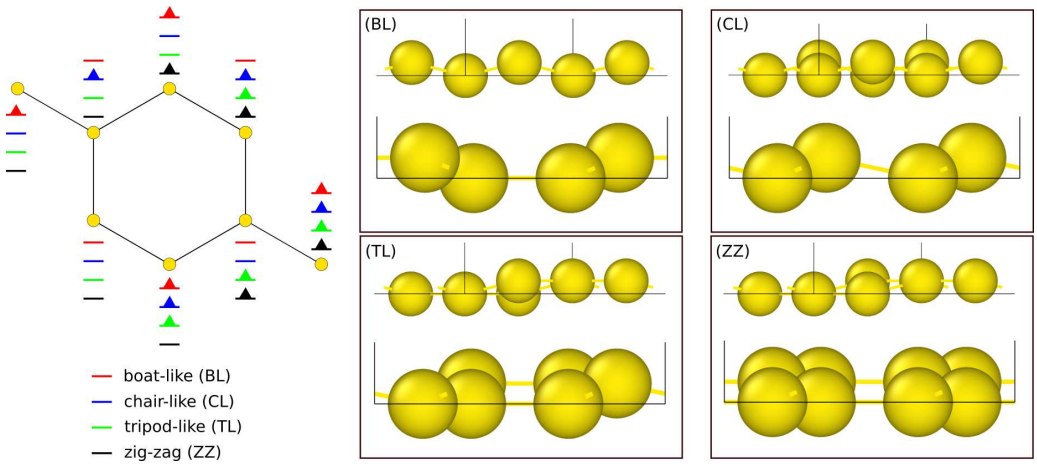

Figure 5.1: Schematic representation of buckling patterns for silicene layer. The left panel shows how the possible patterns can be constructed by combining the dislocation (upward arrows) at different atomic sites. In the right panel, the front and left views of the different patterns are rendered (for LB silicene).

'boat-like' (BL), 'tripod-like' (TL) anz 'zig-zag' (ZZ), is reported in the same figure. For LB and HB structures the buckling pattern listed above have been constructed and optimized with DFT relaxations: the results are collected in Table 5.2. For LB silicene, the most stable structure is most simply constructed from a CL pattern, therefore as an alternation of low/high buckling Si atoms; HB silicene instead can display different phases, although separated by quite a large gap in energy. More importantly, the LB and HB stable configurations are characterized by very different electronic properties, as it is shown in Fig. 5.2: the former behaves like a semiconductor with zero gap, due to the formation of the Dirac cone, while the latter like a metal. The change in the

Pattern	LB silicene			HB silicene		
	ΔSi-Si	Δz	ΔE	ΔSi-Si	Δz	ΔE
CL	2.27	0.47	–	2.6	2.1	1.25
BL	Relaxed into PL silicene			2.5	2.1	–
TL	Relaxed into LB-CL			2.4	1.3-2.0	2.72
ZZ	Relaxed into LB-CL			2.5	2.1	1.30

Table 5.2: Geometrical parameters for relaxed LB and HB free-standing silicene buckling patterns in the 2×2 supercell. ΔSi-Si reports the average interatomic distance in Å, Δz reports the average buckling along z direction in Å; ΔE reports the energy difference in eV.

electronic properties is driven by an increased sp^3 hybridization which is accompanied by a change in the geometry and in the coordination between Si atoms, as the buckling increases. Therefore the LB-silicene is the most favorable platform between the two to

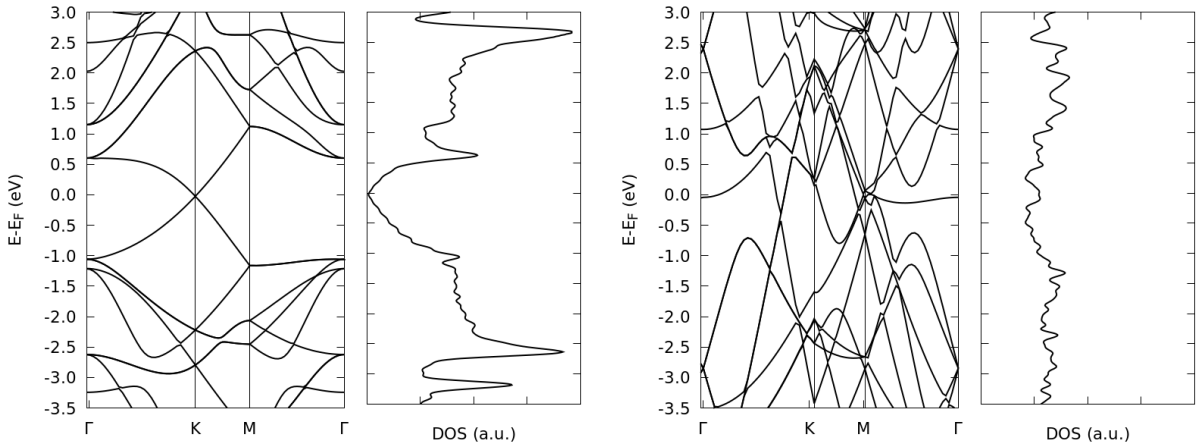

Figure 5.2: Band structure and density of states of LB-CL (left panel) and HB-boatlike (right panel).

study the novel properties introduced with a two-dimensional honeycomb system and is in better agreement with the structure of the phases experimentally observed as grown on Ag(111); in particular its CL buckling pattern will be the focus on the following investigation.

5.2.2 Properties of $\sqrt{7} \times \sqrt{7}$ silicene

The $\sqrt{7} \times \sqrt{7}$ reconstructed supercell of silicene has been constructed; its properties are reported for reference in Fig. 5.3. The differences that can be spotted with the band structure reported in Fig. 5.2 are due to the band folding of the first Brillouin zone of the primitive cell in the newer one; this effect will be discussed with more detail later on.

The absorbance of the FS silicene layer is reported in the left panel of Fig. 5.4; the

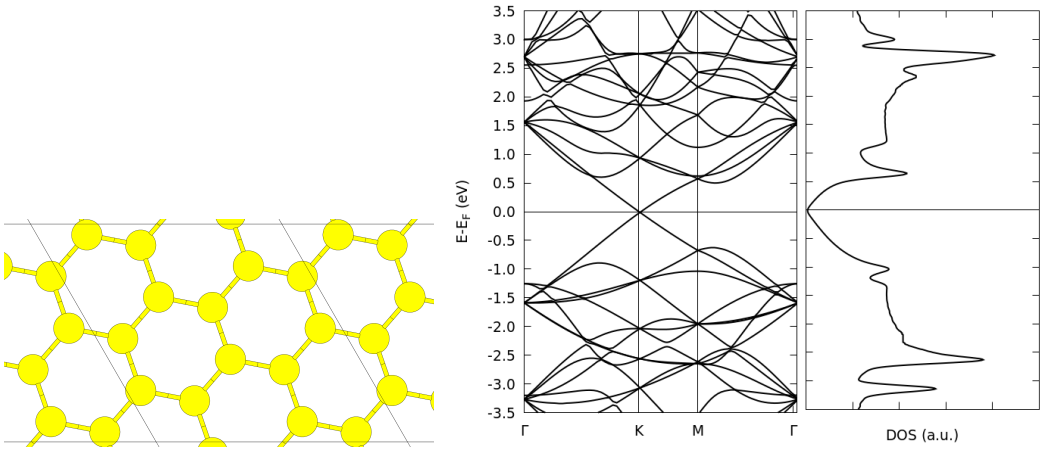

Figure 5.3: Structural model, band structure and density of states of FS LB-CL in the $\sqrt{7} \times \sqrt{7}$ phase.

most important features are two peaks at $\simeq$1.6 and 3.9 eV respectively, which are in good agreement with the results already published in literature [143–145]. The infrared region has been excluded on purpose, since its investigation would require a much denser sampling of the Brillouin zone [143], increasing the computational costs beyond the scope of this study.

The absorbance spectrum has been further investigated to extract additional insights on the electronic properties of the system. The joint bands have been calculated from the electronic structure as the k-dependent difference of the eigenvalues of conduction and valence states. To each point of the joint bands has been associated a transition probability, which is proportional to the transition dipole matrix element between the given pair of valence/conduction states. The spectral intensity has been therefore calculated, as described in Eq. 2.52, by selecting those points of the joint band structure whose energy belongs to the range $(\omega_i - \delta, \omega_i + \delta)$. To highlight the pair of states involved in the electron excitation, the cumulative spectral intensity has been constructed, through the Eq. 2.53a, as the summation on the k-points of the spectral intensity; the results for

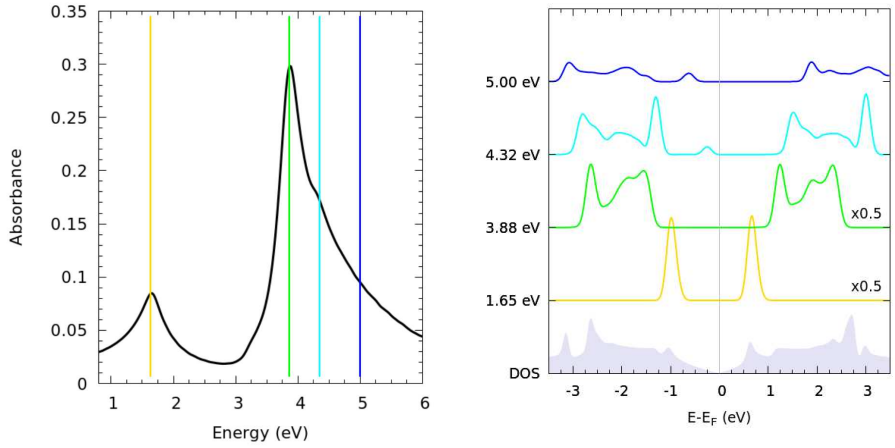

Figure 5.4: Optical properties of FS LB-CL in the $\sqrt{7} \times \sqrt{7}$ phase: absorbance (left panel) and cumulative spectral intensities (right panel). The energy of the transitions for which the contribution of valence-to-conduction pairs is calculated is reported on the y-axis of the spectral intensities; the same are marked on the absorbance spectrum as lines of the corresponding color.

silicene are reported in the right panel of Fig. 5.4.

The dependency of the spectral intensity on the electronic band structure is instead investigated by calculating the k-resolved spectral intensity, which associates to each k-point of the two-dimensional reciprocal space of the slab system the spectral intensity of all the selected valence-conduction pairs. For the LB-silicene, the topmost panels of Fig. 5.5, show in gray all the points in the mapped Brillouin zone, onto which the k-resolved spectral intensity for two different transition energies has been overlapped. In the figure it can be noted that it is not possible to select only a path among high-symmetry points, the whole Brillouin zone has to be taken into account because of Yambo's necessity to deal with a uniform k-point grid.

The peak around ω_i=1.65 eV can be clearly addressed to transitions taking place from the bands just outside the Dirac cone; in literature such transitions are related to a Van Hove singularity in the joint density of states in the vicinity of the high-symmetry M point [140]. To correctly address such property in the spectral intensity, it is useful to recall that a Van Hove singularity is associated with a critical point in the joint band structure [51]. The type of critical point is reflected on the shape of the singularity, in particular, for a two-dimensional system like the one under investigation, a minimum is correlated to a step in the joint density of states, whereas a saddle point is correlated to a divergence. As a most direct investigation, the three-dimensional joint bands can be

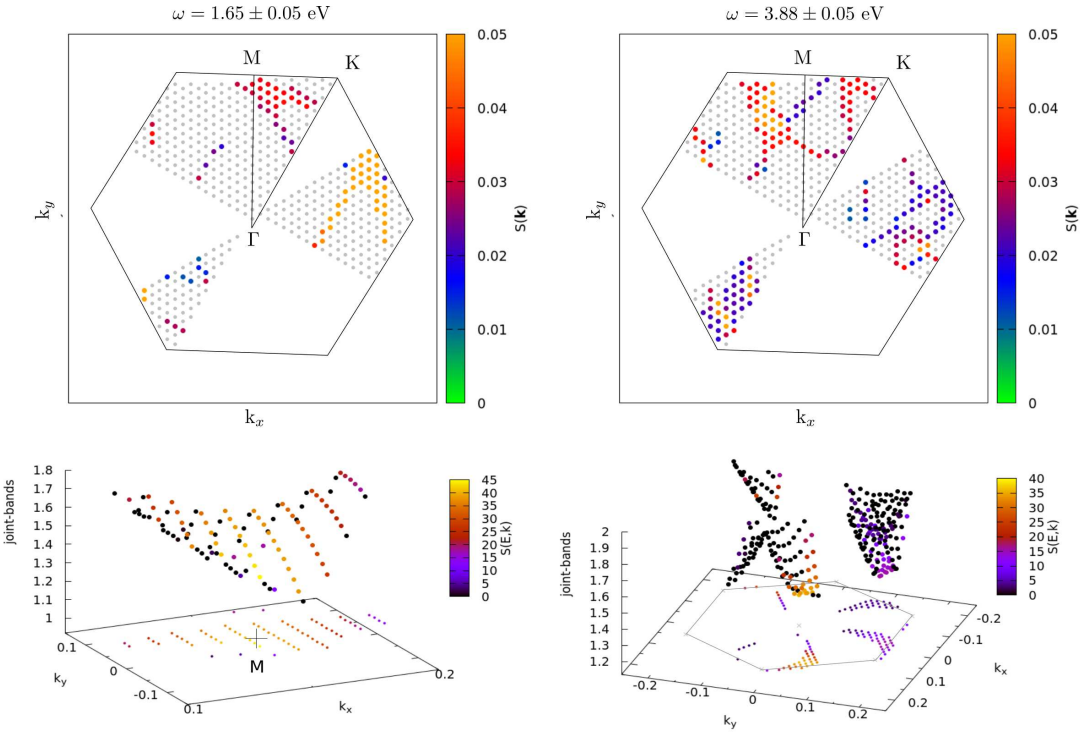

Figure 5.5: Top panel: k-resolved spectral intensity of FS LB-CL silicene in the $\sqrt{7}\times\sqrt{7}$ phase, reported for two transition energies, corresponding to the peaks in the absorbance. The grey dots represent the grid of k-points, mapping the Brillouin zone (superimposed as black line). At each point, the colors represent the spectral intensity, for a given transition, summed over all the involved valence-conduction pairs. Bottom panel: the points represent the joint band structure; the color of which reports the spectral intensity for the valence-to-conduction pairs with the highest transition dipole for the transition at ω_i=1.65 eV. The left panel shows a zoom around an M point, while the right panel shows the entire Brillouin zone. In both cases, a cutoff is introduced, corresponding to ∼10% of the maximum, for the lowest spectral intensity in order to report only the most intense contributions.

represented, where the spectral intensity can be reported for every point: this is shown in the lower panels of the Fig. 5.5 for the transitions at ω_i=1.65 eV. The surface of two sections of joint bands is shown, for the choice of two different valence-conduction indexes in the regular band structure, with a similar contribution to the same transition. The one reported in the lower left panel has a saddle shape, as expected from theory; the corresponding k-resolved spectral intensity, shown in the upper left panel of the same figure carries a distinctive cross-like shape. The surface section reported in the lower

right panel of Fig. 5.5 shows instead a parabolic shape of the spectral intensity, which can be distinguished in the k-resolved spectral intensity reported in the upper right panel of the same figure as a circular spot, and corresponds to a minimum point of the joint band structure.
In both cases, the transitions take place almost around the high symmetry M point in the reciprocal space, although not around all of the ones in the Brillouin zone. This apparent symmetry breaking in the cell is most probably the result both the band folding from the 1×1 lattice and numerical issues in mapping the Brillouin zone for a non-integer reconstruction. A similar analysis for the transitions with frequency ω_i=3.88 eV suggests that in this case the excitation takes place at several spots in the reciprocal space and the overall absorption is not related to a Van Hove singularity but instead to the overlap of different transitions.

5.2.3 Hydrogenation

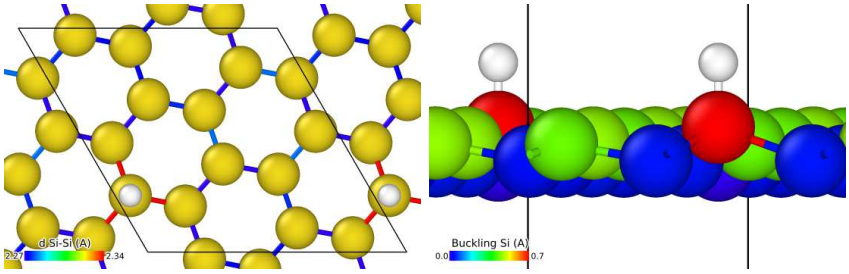

Figure 5.6: Geometrical model of optimized FS LB-CL silicene with an adsorbed H atom. Left: top view, the color scale indicates the different Si-Si bond lengths. Right: front view, the colors address the height of Si atoms. The white spheres represent H adatoms.

Low H coverage

The first step in the functionalization of silicene, is to add a single H atom on top of the surface of the LB-CL silicene. Several starting configurations have been optimized for different adsorption sites, however all the systems relax to the H atom sitting on a top site, with the Si atoms underneath it protruding upwards. The relaxed geometry, as reported in Fig. 5.6, is showing a silicene-like configuration, locally perturbed around the H atoms: the H-Si distance is 1.50 Å, the Si-Si distance increases around it to 2.34 Å, while the buckling of the Si atom bound to the H one is 0.79 Å. The adsorption energy of the adatom, calculated as $E^H_{ads} = (E_{\text{tot}} - E_{\text{Si:H}})/N_{\text{H}} + N_H * E_{\text{H}}$ with $N_{\text{H}} = 1$, is -2.46

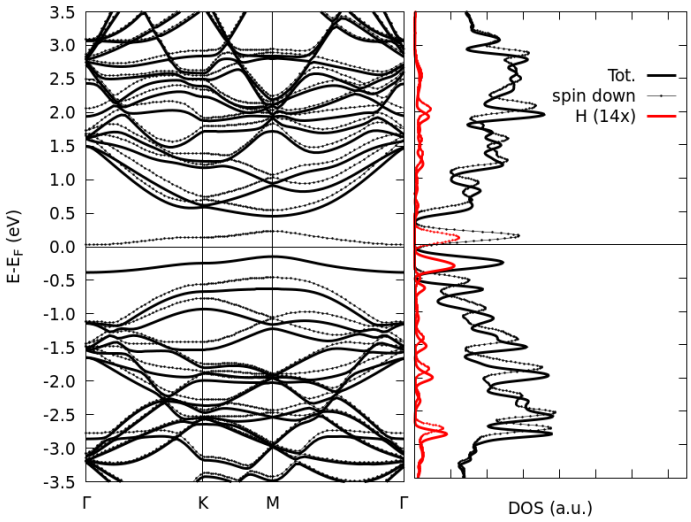

Figure 5.7: Spin-dependent band structure and density of states of FS LB-CL silicene with an adsorbed H atom. The solid and the dotted lines show the contributions of the two spins, respectively. The red lines report the projection of the density of states onto the H atomic orbitals.

eV. The electronic properties show instead a much pronounced changed, as shown in Fig. 5.7: even with just one H atom the bands forming the Dirac cone are opened up to form a (spin-dependent) delocalized state around the Fermi energy, to which both Si and H are contributing, sign of a certain amount of hybridization. A direct band gap is opened of $\simeq$ 1 eV, with the two new states located within it, separated by $\simeq$ 0.5 eV.

The optical absorption spectrum is reported in Fig. 5.8: three features can observed at 1.50, 2.20 and 3.85 eV, respectively. Investigating the cumulative spectral intensities at such transition energies, which are reported in the right panel of the same figure, the states at the top of the valence band are mostly involved in the lowest energy transitions. The main peak in absorption is instead formed by the superposition of several transitions originating deeper in valence and conduction bands. The k-resolved spectral intensities don't show any localized contribution in the first Brillouin zone and are not reported here.

Half Silicane

When the coverage is increased, the adatoms can be arranged into different patterns, which can be exploited in a fashion similar to the buckling of Si atoms. Systematically probing such configurations, on the LB-CL silicene the most stable adsorption pattern

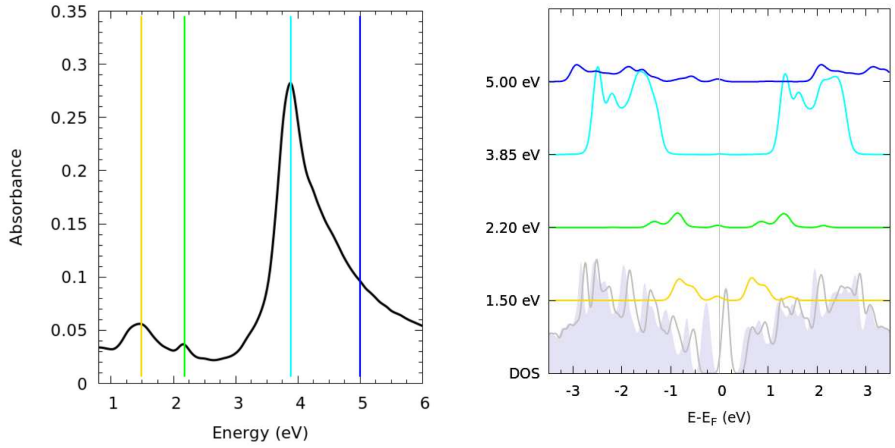

Figure 5.8: Left panel: optical absorption spectrum for the simulated spin-dependent FS LB-CL silicene, functionalized with a single H adatom. Right panel: cumulative spectral intensity of the transition marked in the absorption spectrum, the energy of which is reported on the y-axis. At the bottom of the plot, the spin-dependent DOS is reported; the spectral intensities of spin majority and minority coincide on the scale of the figure.

is the zig-zag one, followed by the chairlike pattern with an energy difference of 0.04 eV. Since the goal of this part of the investigation is to study the free-standing systems as a reference for the subsequent growth onto the silver surface, the CL arrangement of adatoms only has been taken into account. In this case the optimized geometry of half silicane is shown in Fig. 5.9. Its structure is similar to the silicene one perturbed

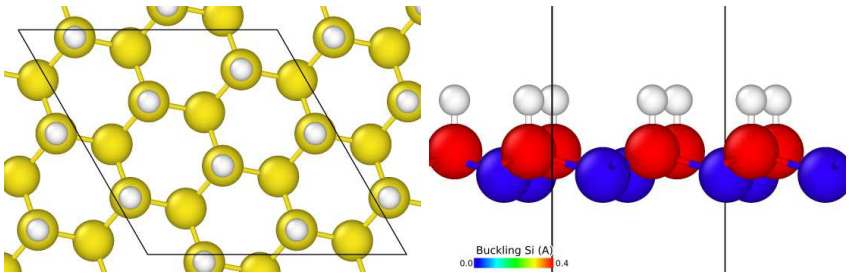

Figure 5.9: Geometrical model of optimized FS LB-CL half silicane: top view (left panel)and front view (right panel), where the colors address the height of Si atoms. The white spheres represent H adatoms.

by the single H atom: the Si-Si distance is 2.33 Å and the buckling of the layer is 0.40 Å; the adsorption energy E^H_{ads}=-2.50 eV/H suggests that the formation of a higher coverage overlayer of H adatoms is favored. In comparison with the single H adatom, because of the increased passivation of Si atoms driven by adsorption, more states from

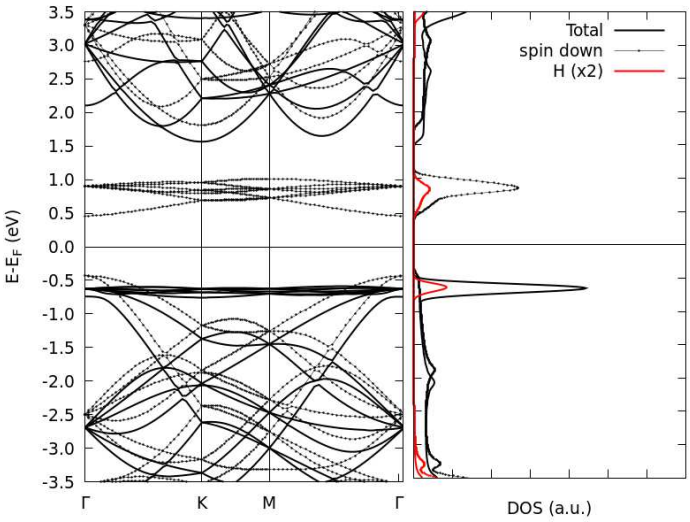

Figure 5.10: Spin-dependent band structure and density of states of FS LB-CL half silicane. The solid and the dotted lines show the contributions of the two spins. The red lines report the projection of the density of states onto the H atomic orbitals.

both the bottom of the conduction band and the top of the valence band of silicene are hybridized with H states. Therefore, as shown in Fig. 5.10, the band gap is further opened up to $\simeq 2$ eV while additional states within the gap are formed, increasing the width of the intragap band. These newer states show a contribution from both Si and H atoms and a bonding/antibonding structure, where the occupied ones overlap with the top of the valence band. The other bands are minimally contributed by H orbitals and can be recognized in the band structure of silicene. In the case of a spin-independent calculation with the same geometry, which is the same way the half silicene is treated (and behaves) when grown on the Ag surface, the bands structure differs only for the position of the mid-gap states, that are shifted just below the Fermi level.

The optical absorption, reported in Fig. 5.11, reflects the change in the electronic properties, as the spectrum is almost flat for energies up to the size of band gap. Moreover, a double-peak feature can be observed around 4 eV: the calculation of the spectral intensities, reported in the right panel of the same figure, allows to track different spin-dependent transitions. The peak at $\simeq 3.7$ eV is originated from the topmost states in the valence band, almost independently from the spin polarization. The broader peak around 4.30 eV is instead characterized by a stronger asymmetry in the contributions of spin-dependent states, due to the involvement of the midgap, spin-dependent states. The k-resolved spectral intensity, which is shown in Fig. 5.12, agrees with the flat shape

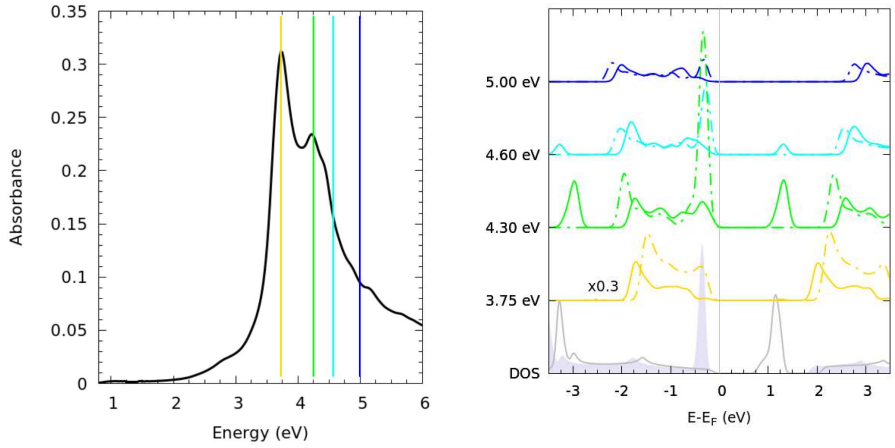

Figure 5.11: Left panel: optical absorption spectrum for the simulated spin-dependent FS LB-CL half silicane. Right panel: cumulative spectral intensity of the transition marked in the absorption spectrum, the energy of which is reported on the y axis. The spin majority component is represented by dot-dash lines, while the minority component is represented by solid lines.

of the band structure, as no particular fingerprint of minimum points or saddle points can be tracked.

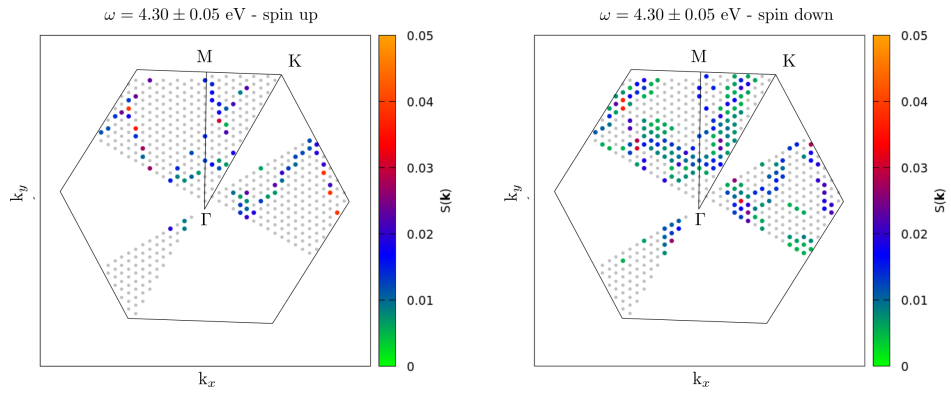

Figure 5.12: K-resolved spectral intensity for for the simulated spin-dependent FS LB-CL half silicane, at the transition energy ω_i=4.30 eV. The grey dots represent the k-point grid mapping the Brillouin zone, which is superimposed as the black line, along with the high symmetry points. The colored points represent the summed intensity of all transitions, for a given frequency, at the selected k-point. A lower cutoff for the spectral intensity > 0.01 has been introduced.

Silicane

As the last coverage step, the full passivation of the free-standing silicene layer is investigated. The optimized geometry of silicane, which is shown in Fig. 5.13, is similar to the one reported previously for half silicane, although with a larger buckling, here of 0.75 Å. The adsorption energy for this system is -2.89 eV/H atom, hence larger than the previous cases. The band structure of silicane is similar to that of half silicane, with an

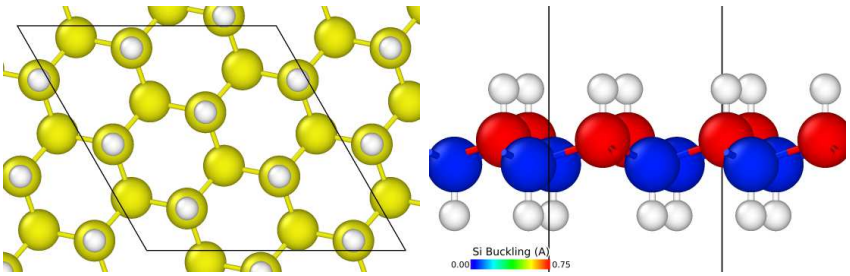

Figure 5.13: Geometrical model of optimized FS LB-CL silicane: top view (left panel)and front view (right panel), where the colors address the height of Si atoms. The white spheres represent H adatoms.

almost unperturbed valence and conduction band derived from silicene but the intragap band is here shifted deeper in the valence band, namely around 3 eV below the Fermi level. The indirect band gap opened through the full passivation of Si atoms is $\simeq$ 2 eV.

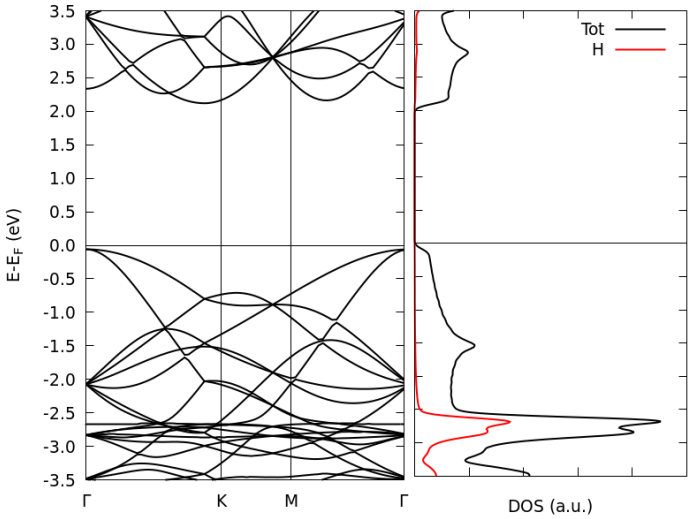

Figure 5.14: Spin-dependent band structure and density of states of FS LB-CL half-silicane. The solid and the dotted lines show the contributions of the two spins. The red lines report the projection of the density of states onto the H atomic orbitals.

Such modifications of the electronic structures can be observed in the absorption spectrum, shown in Fig. 5.15: the size of band gap corresponds to the position of the onset of the absorption, while the energy difference between several peaks in the density of states corresponds to the position of the main absorption peak at $\simeq$ 3.60 eV. From the

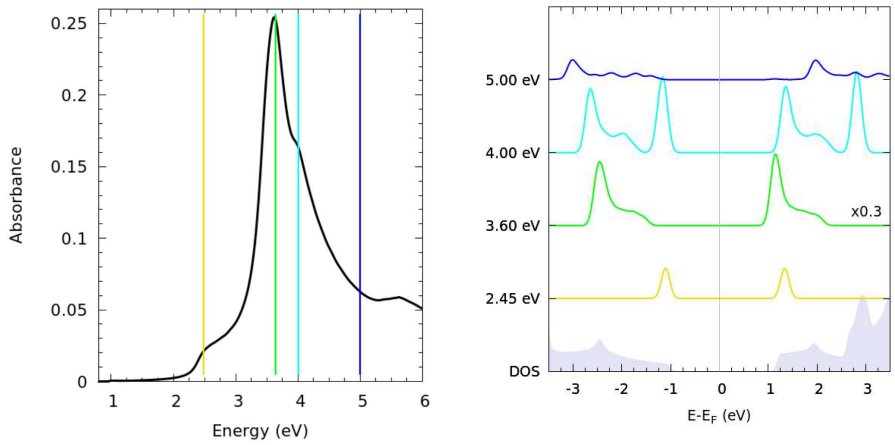

Figure 5.15: Optical properties of FS LB-CL silicane: absorbance (left panel) and cumulative spectral intensities (right panel). The energy of the transitions for which the contribution of valence-to-conduction pairs is calculated is reported on the y-axis of the spectral intensities; the same are marked on the absorbance spectrum as lines of the corresponding color. The position of the Fermi energy is different from the one reported in the band structure because of the electronic broadening introduced by Yambo and because of its arbitrariness within the band gap.

spectral intensity, reported in the same figure, the transitions originate mainly from the edge of the valence and conduction bands and from the peaks in the density of states at around -2.8, -1.5, 2.6, 4.0 eV. The analysis of the k-resolved spectral intensity, which is shown in Fig. 5.16 confirms that these transitions are related to Van Hove singularities in the joint band structure. The same analysis on the feature in the absorption at 2.45 eV confirms that the transitions take place from a minimum of the joint band structure, which corresponds to a minimum/maximum in the conduction/valence bands.

5.2.4 Fluorination

Low F coverage

In the case of the adsorption of a single atom of fluorine, the optimized geometry, which is reported in Fig. 5.17 is similar to the one with a single hydrogen atom, although with

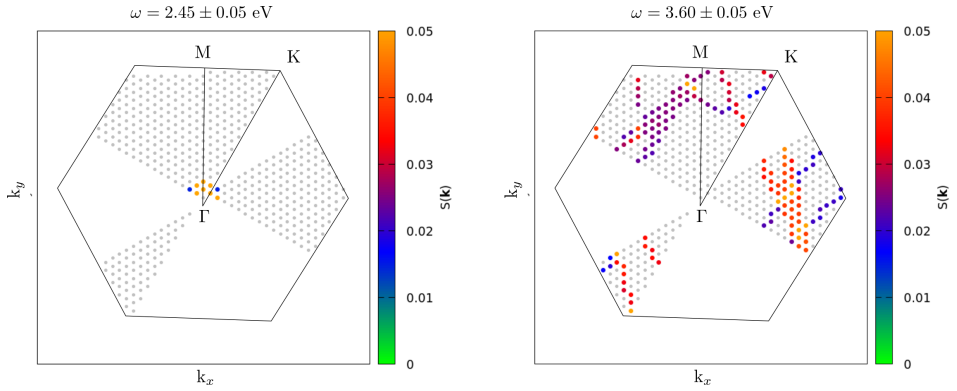

Figure 5.16: K-resolved spectral intensity of FS LB-CL silicane, reported for two transition energies, corresponding to the peaks highlighted in the absorbance. The grey dots represent the k-point grid mapping the Brillouin zone, which is superimposed as the black line, along with the high symmetry points. The colored points represent the summed intensity of all transitions, for a given frequency, at the selected k-point. A lower cutoff for the spectral intensity > 0.01 has been introduced.

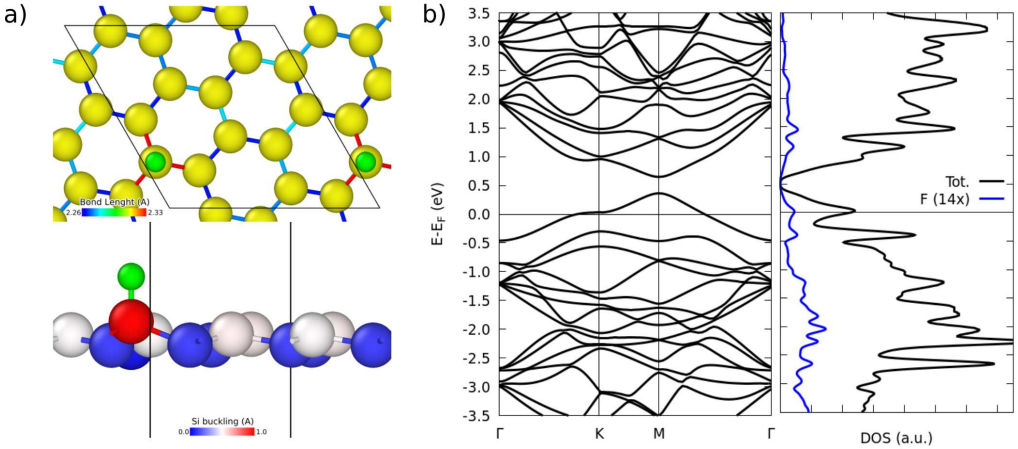

Figure 5.17: Panel a): geometrical model of optimized FS LB-CL silicene with an adsorbed F atom: top view (top) and front view (bottom), where the colors address the bond length or the height of Si atoms, respectively. The color code is reported in each panel. The green spheres represent F adatoms. Panel b): calculated band structure and density of states. The blue line reports the DOS projected onto F atomic orbitals.

a larger Si-F distance of 1.63 Å. The buckling of Si atoms is larger, with an average of 0.5 Å, while it grows to around 1 Å for the atom underneath the F one. Overall, the adsorption of F is more stable compared with H, with an adsorption energy of -6.40 eV. The band structure, reported in the same figure, shows the disappearance of the

Dirac cone, in favor of two additional bands, closer to valence and conduction bands maximum/minimum and the opening of a small band gap of $\simeq 0.4$ eV. In this case the

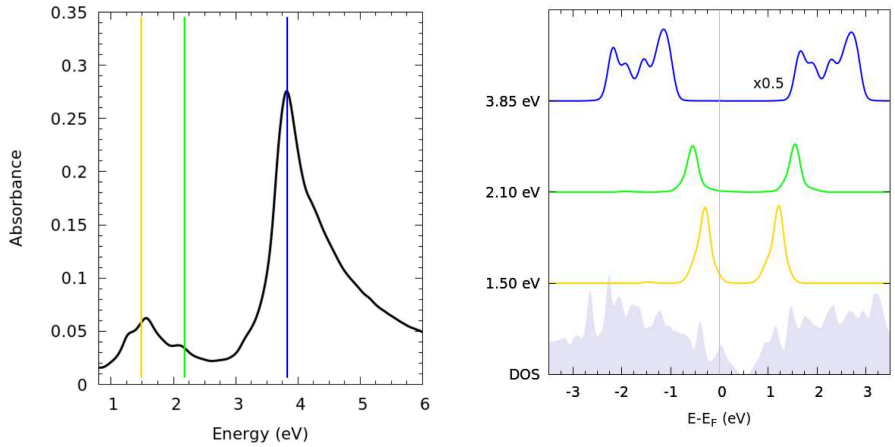

Figure 5.18: Optical properties of FS LB-CL silicene with an adsorbed F atom: absorbance (left panel) and cumulative spectral intensities (right panel). The energy of the transitions for which the contribution of valence-to-conduction pairs is calculated is reported on the y-axis of the spectral intensities; the same are marked on the absorbance spectrum as lines of the corresponding color.

projection of the new states onto the atomic orbitals of the F atom is negligible, showing a different behavior compared with the functionalization with H adatoms. This fact suggests that the hybrid bonding/antibonding states are formed at much lower/larger energies at the newer states close to Fermi level are perturbed silicene states.

The optical absorption spectrum is reported in Fig. 5.18, where two main features can be observed: one broad around 1.5 eV and a sharp one at 3.85 eV. Their spectral intensities are investigated in the same figure: both features are similar in energy and origin to the one observed with H and are due to non-localized transitions (in reciprocal space) from the edge of valence and conduction bands and from deeper states within them, respectively.

Half Fluoro-Silicane

The passivation of Si atoms only on one side leads to a much more irregular Si layer, as the optimized geometry of the system shows in Fig. 5.19. The increased corrugation is accompanied by a perturbation in the band structure, reported in the same figure. Similarly to the half silicane, a band gap of around 2.5 eV is opened and an intragap band is formed, although such states are not hybrid Si-F ones. Differently from half silicane,

instead, the adsorption energy (per F atom) of the functionalised layer E_{ads}^{F}=-5.92 eV is lower than the one of a single adatom, because some energy is spent in deforming silicene.

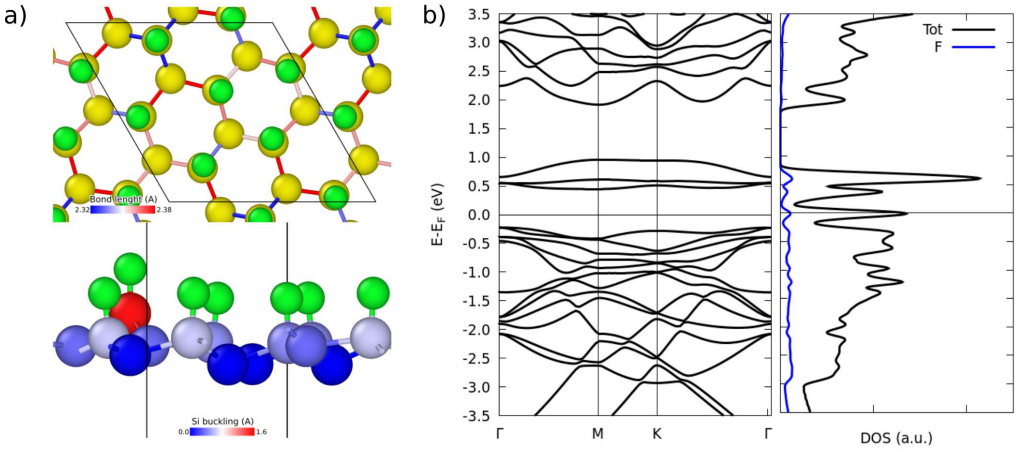

Figure 5.19: Panel a): geometrical model of optimized FS LB-CL half fluoro-silicane: top view (top) and front view (bottom), where the colors address the bond length or the height of Si atoms, respectively. The color code is reported in each panel. The green spheres represent the F adatoms. Panel b): calculated band structure and density of states. The blue line reports the DOS projected onto F atomic orbitals.

The optical absorption properties of half fluoro-silicane are reported in Fig. 5.20, where two main features can be observed: a broad one around 1 eV and a sharp one at 3.25 eV. The latter has the same spectral intensity components of that observed in half silicane at 3.75 eV; such redshift accounts for the different perturbation introduced by F atoms; the former instead is related to transitions ending in the intragap band. The investigation of the k-resolved spectral intensity, reported in Fig. 5.21, suggests that the lower-energy feature is related to absorption from bands minima around the Γ point, while for the higher-energy feature, the absorption can be tracked towards the edge of conduction band, especially at the minima close to M points.

Fluoro-Silicane

The optimized structure for the free-standing fluoro-silicane, which is reported in Fig. 5.22, shows a more regular geometry than the previous case, with a buckling of Si atoms of 0.9 Å, larger than the one calculated for silicane. In this case the adsorption energy is -6.47 eV/F atom, larger than the one obtained for the two previous coverage steps

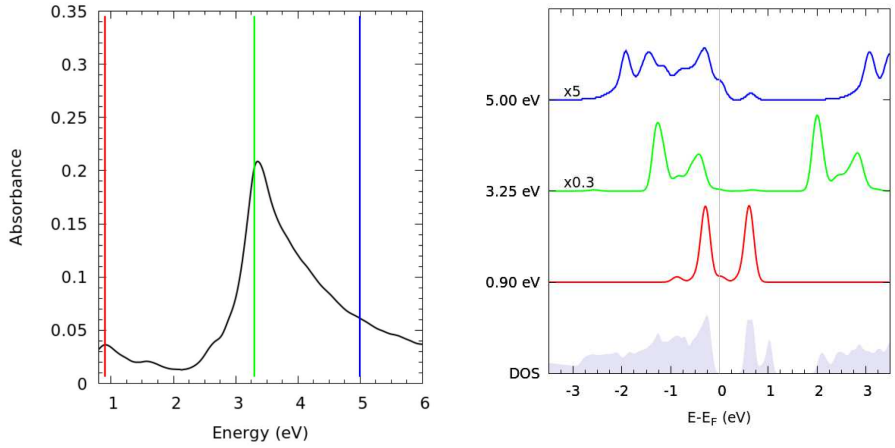

Figure 5.20: Optical properties of FS LB-CL half fluoro-silicane: absorbance (left panel) and cumulative spectral intensities (right panel). The energy of the transitions for which the contribution of valence-to-conduction pairs is calculated is reported on the y-axis of the spectral intensities; the same are marked on the absorbance spectrum as lines of the corresponding color. The position of the Fermi energy is different from the one reported in the band structure because of the electronic broadening introduced by Yambo and because of its arbitrariness within the band gap.

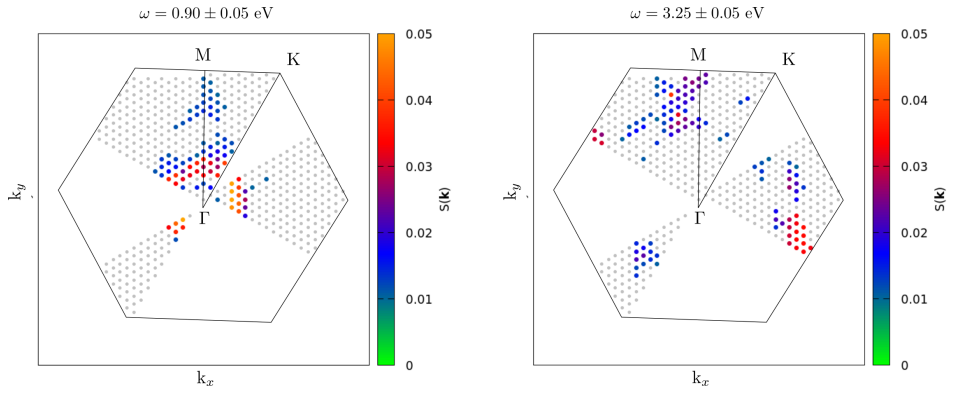

Figure 5.21: K-resolved spectral intensity of FS LB-CL half fluoro-silicane, reported for two transition energies, corresponding to the peaks highlighted in the absorbance. The grey dots represent the k-point grid mapping the Brillouin zone, which is superimposed as the black line, along with the high symmetry points. The colored points represent the summed intensity of all transitions, for a given frequency, at the selected k-point. A lower cutoff for the spectral intensity > 0.01 has been introduced.

of F adatoms, which is expected for the fully passivated silicene. The band structure is shown in Fig. 5.22, where a comparison with the one of silicene and silicane, reveals that

while the valence band is almost unchanged, the conduction band differs as its lower-energy states are those originating from the perturbation of Si atoms, which formed the intraband in half fluoro-silicane, while the higher-energy states are the same found in silicane and silicene. Because of these new states, the band gap is remarkably direct, with an amplitude reduced to 0.5 eV. The optical absorption spectrum is then reported

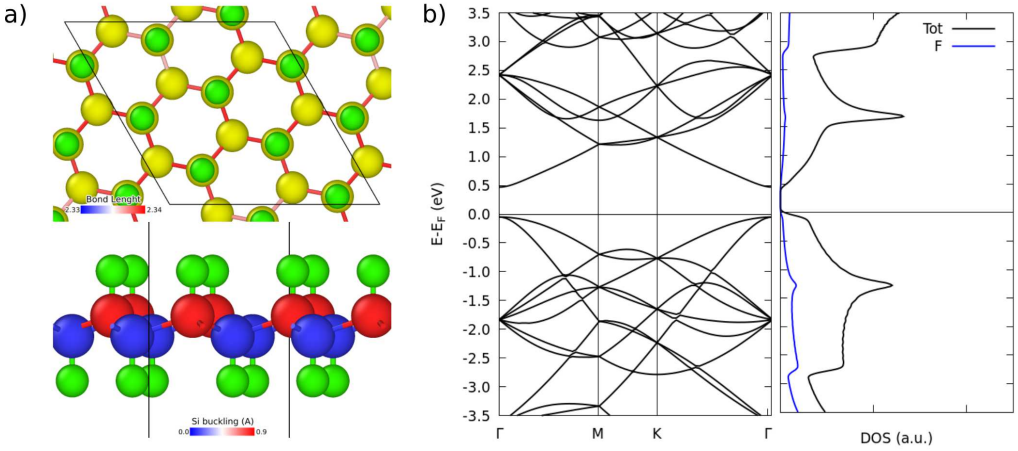

Figure 5.22: Panel a): geometrical model of optimized FS LB-CL fluoro-silicane: top view (top) and front view (bottom), where the colors address the bond length or the height of Si atoms, respectively. The color code is reported in each panel. The green spheres represent the F adatoms. Panel b): calculated band structure and density of states. The blue line reports the DOS projected onto F atomic orbitals.

in Fig. 5.23: two sharp peaks can be observed at 2.90 and 3.75 eV, which have been investigated calculating the cumulative spectral intensity at such energies. The former is due to transitions taking place between states deeper in valence and conduction bands; while the latter is due to electrons excited from the topmost levels of the valence band. Their k-resolved spectral intensities, shown in Fig. 5.24, reveal the electronic nature of the two absorption peaks along the reciprocal space: the one at at 2.90 is mostly related to a Van Hove singularity in the joint band structure almost at the M points, while the one at 3.75 eV is related to saddle points, which are close to the K points.

5.3 Ag properties

5.3.1 Bulk dielectric function

The dielectric function of bulk Ag is required to correctly calculate the reflectivity spectrum of the surface through the three-regions model; in the bulk, however, the intraband

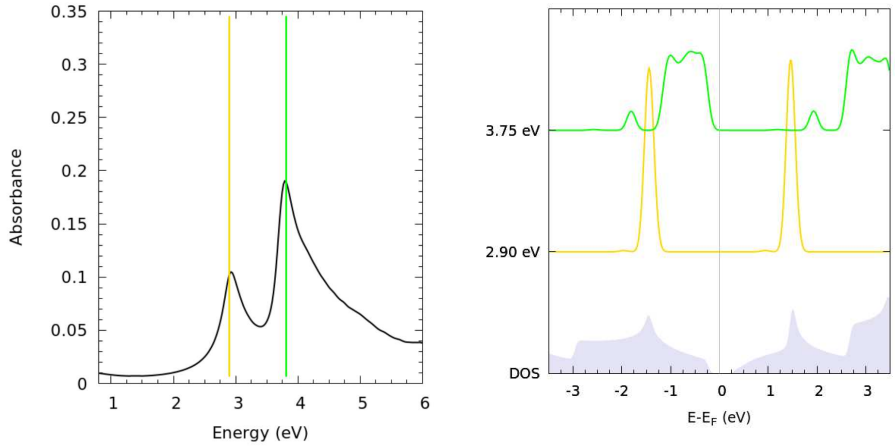

Figure 5.23: Optical properties of FS LB-CL fluoro-silicane: absorbance (left panel) and cumulative spectral intensities (right panel). The energy of the transitions for which the contribution of valence-to-conduction pairs is calculated is reported on the y-axis of the spectral intensities; the same are marked on the absorbance spectrum as lines of the corresponding color.

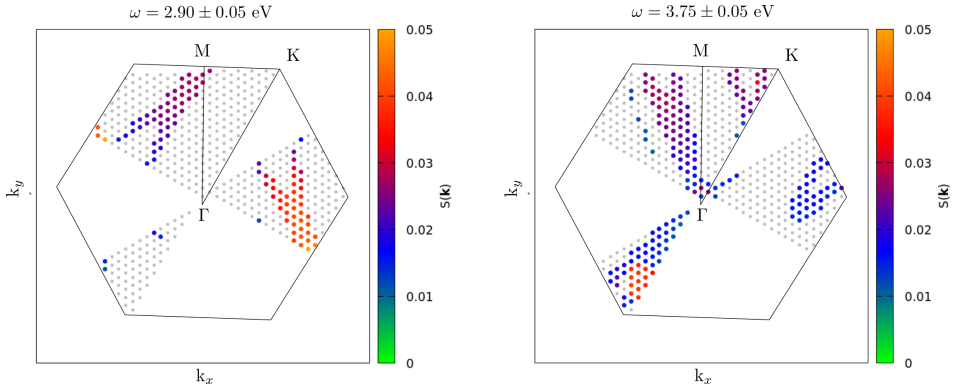

Figure 5.24: K-resolved spectral intensity of FS LB-CL half fluoro-silicane, reported for two transition energies, corresponding to the peaks highlighted in the absorbance. The grey dots represent the k-point grid mapping the Brillouin zone, which is superimposed as the black line, along with the high symmetry points. The colored points represent the summed intensity of all transitions, for a given frequency, at the selected k-point. A lower cutoff for the spectral intensity > 0.01 has been introduced.

transitions have to be properly accounted for. Physically, such excitations take place very close to Fermi energy, where the electrons behave as free particles. Within the periodically repeated supercell which is constructed to run the bulk simulation, such band is not thick enough to properly map such transition with direct transitions. Only in the

case of a larger supercell, the band folding of the Brillouin zone of the primitive cell into the smaller Brillouin zone of the new cell, fictitiously increases the number of bands, in particular around the Fermi energy, allowing to partly include the intraband transitions. An accurate simulation of these would therefore require an extremely large supercell. As a more affordable solution, the contribution of such near-Fermi level electron is introduced numerically, by adding to the dielectric function the real and imaginary parts obtained through the classical Drude model, described in Eqs. 2.1, which require the plasma frequency ω_p. Its value has been obtained by finding the frequency through which the real part of the dielectric function got the better agreement with experimental results [169], especially around the point where it changes sign. In particular, we found ω_p=8.90 eV, slightly smaller that what found in Ref. [155]. The effect on the macroscopic dielectric function of this Drude term is shown in Fig. 5.25: the largest change is introduced into its real component, which gets a negative divergence and a crossing point is allowed, where the function can change sign, as expected. In the same panel it is shown the effect of neglecting the non-local term of the potential, including the electronic correlation term provided by the DFT exchange-correlation functional. The reflectivity of bulk Ag, calculated through Snell equations and show in Fig. 5.25, agrees with the one reported in the same study; the small difference between the two results is due to the different exchange and correlation functional, as the PBE accounts for a slightly larger electronic correlation than LDA. However, both results slightly differ from the experimental spectrum [169], namely a redshift in the onset of the plasma oscillations: this is due to neglecting electron correlation effects as done through the independent particle approximation. The bulk characteristic functions $A(\omega)$, $B(\omega)$ introduced for obtaining the surface differential reflectivity spectroscopy (SDRS) (Eqs.2.55) obtained from this work are reported in Fig. 5.25

5.3.2 Clean Ag(111) surface

The clean surface is the support for the grown of the silicene overlayer and its subsequent functionalization. Its band structure, shown in Fig. 5.26, is characterized by *sp* states around the Fermi level and by the thick band of *d* states for energies lower than 3 eV below it. Its optical absorption spectrum is reported in Fig. 5.27, along with the one calculated for the bulk system without any Drude correction: the two spectra are in good agreement. As previously introduced, the slab allows a partial introduction of the intraband transitions because of the band folding, given by its large size compared with the bulk cell. Investigating the cumulative spectral intensities of the system, shown in

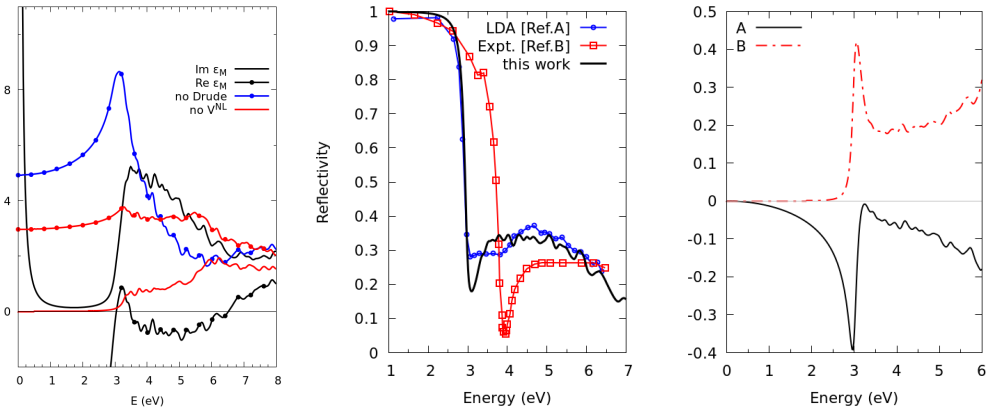

Figure 5.25: Left panel: real and imaginary part of the macroscopic dielectric function for bulk Ag, calculated with different approximations, namely without the Drude contribution (blue line, real component only) or without the non-local term of the potential (V^{NL}, red lines). Middle panel: reflectivity of Ag, as calculated with different DFT approximations, compared with experimental results. Data in Ref. [A] taken from [155], Ref. [B] taken from [169]. Right panel: auxiliary functions $A(\omega)$, $B(\omega)$ from the three-regions model as characteristic bulk functions.

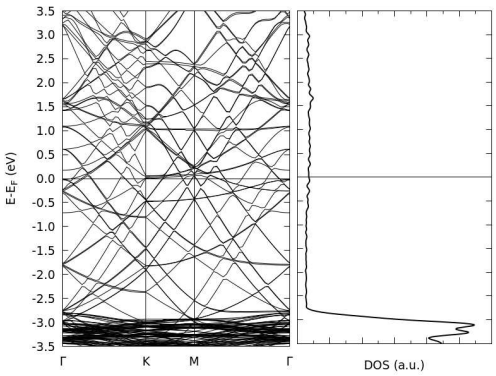

Figure 5.26: Band structure and density of states of the clean Ag(111) surface.

the same figure, the infrared absorption is connected with intraband transitions around the Fermi energy, while for higher energies the electrons get excited from the onset of the large band of atomic d orbitals.

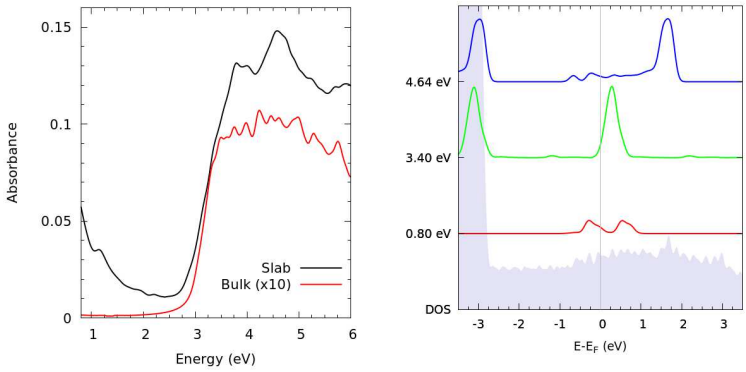

Figure 5.27: Optical absorption spectrum (left panel) and cumulative spectral intensities for the clean Ag(111) surface. The absorption spectrum calculated for the bulk system is show for comparison.

5.4 Silicene grown on Ag(111)

5.4.1 Adsorption configuration

Now that the role of the functionalization of pristine silicene has been discussed, it is possible to introduce the effect of the adsorption of such layers onto the silver surface. The free standing systems have been coupled with the Ag slab and the coordinates have been optimized through a DFT relaxation; the results for hydrogenated phases are collected in Fig. 5.28 whereas those for fluorinated phases are qualitatively equivalent. The adsorption energy has been calculated in order to express the energy balance (per silicon atom) of adsorbing the whole overlayer on top of the surface, namely $E_{ads} = \left(E_{SiX/Ag} - E_{SiX} - E_{Ag}\right)/N_{Si}$. Here SiX labels the generic functionalized silicene phase and E_{SiX} is the corresponding total energy calculated for the free-standing layer. The values extracted from the optimized coordinated are collected in Table. 5.3, along with several parameters describing the relaxed geometry, namely the average interatomic distances d_{X-Y} and the average buckling of the Si layer b_{Si}. For pristine silicene, the presence of the surface increases the corrugation of the adlayer, while for half silicane, for both H or F adatoms, the effect of the surface is to stabilize the structure of buckled Si atoms, as the value of average buckling decreases. More importantly, the average bond length of the atoms in each system is around 2 Å, suggesting a mixed chemical-physical nature of the interactions at the interface, independently from the chemical species of the passivating adatom. At the same time, the adsorption energies of silicane and fluoro-silicane on Ag are considerably smaller then the other silicene phases, as expected from a passivated overlayer, still indicate a much weaker interaction of the adlayers with the

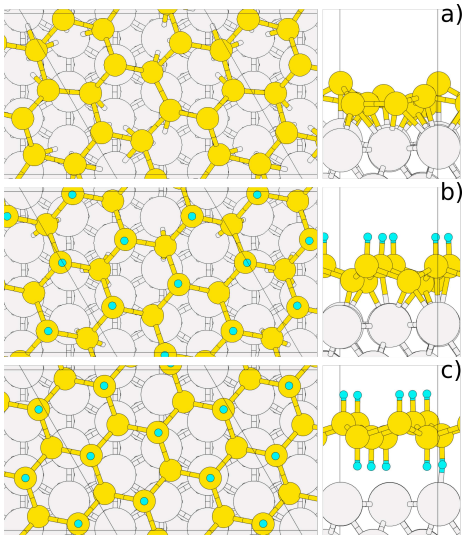

Figure 5.28: Top and side view of the optimized coordinates of silicene (a), half silicane (b) and silicane (c) adsorbed on Ag(111). The grey spheres represent Ag atoms, the yellow ones Si atoms and the cyan ones H atoms. The results for the corresponding fluorinated systems are equivalent.

surface.

5.4.2 Electronic properties

To investigate in detail the coupling of the interface, the several electronic properties have been calculated and compared between different coverages. First, the change of the spatial distribution of the electron density induced by the adsorption has been extracted as $\Delta n(\mathbf{r}) = n_{Tot}(\mathbf{r}) - n_{SiX}(\mathbf{r}) - n_{Ag}(\mathbf{r})$ and it is reported in Fig. 5.29. At all coverages, the largest modifications can be observed between the metallic surface and the functionalized silicene overlayer, indicating that new bonds are formed between Ag atoms and the chemical species facing it. Such changes can be still tracked both in the silicon backbone and the first layer of the slab, even for fully passivated silicenes. For a more qualitative approach, the charge transfer Δn between the layers has been investigated by the means of Löwdin analysis [170], the results of which are collected in Table 5.4. Even though such a projection scheme cannot efficiently assign the charge to one atom or another in the case of rapidly varying wavefunctions, it allows to confirm the mixed chemical/physical nature of the interaction at the surface.

The band structure of coverage-dependent functionalized silicene, either hydrogenated or fluorinated, are collected in Fig. 5.30. To address the level of hybridization between

on Ag(111)	**Si**	**hSiH**	**hSiF**	**SiH**	**SiF**
E_{ads}/Si	-0.70	-0.95	-1.03	-0.17	-0.19
d_{Si-Ag}	2.47	2.69	2.65	3.85	4.58
d_{X_u-Si}	-	1.90	2.00	1.85	1.97
d_{Si-X_d}	-	-	-	1.86	1.97
d_{X_d-Ag}	-	-	-	1.98	2.61
b_{Si}	1.15	0.89	0.98	0.79	1.01

Table 5.3: Geometric and energy details for silicene (Si), half silicane (hSiH). half-fluoro-silicane (hSiF), silicane (SiH) and fluoro-silicane (SiF) adsorbed on Ag(111). Energies E are reported in eV per Si atom, inter-atomic distances d and buckling b_{Si} in Å. X_u/X_d label the H or F passivating atoms adsorbated on the upper/lower face of the silicene sheet.

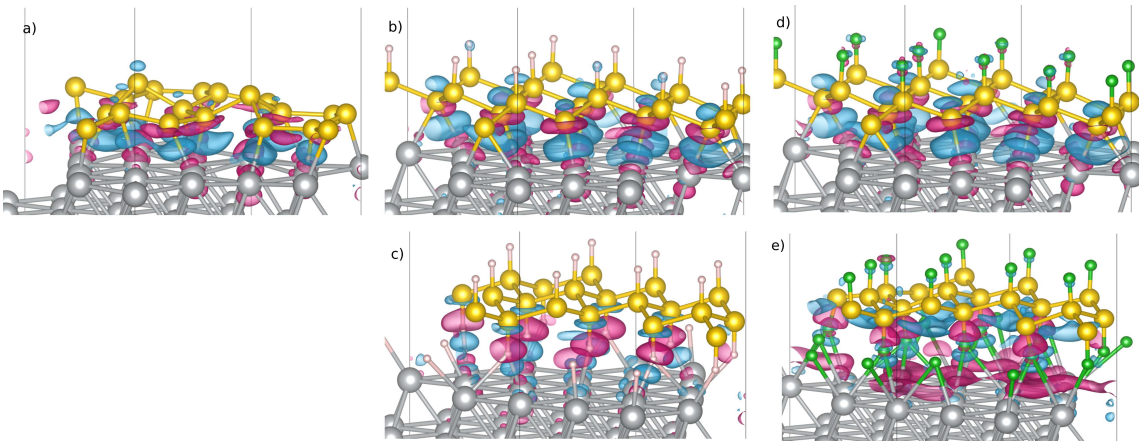

Figure 5.29: Perspective view of the electron density change Δn of silicene (a), half silicane (b) and silicane (c) after the adsorbption on Ag(111) for an isovalue of 0.003 e^-/A^3. The grey spheres represent Ag atoms, the yellow ones Si atoms and the white/green ones H/F atoms. The blue/magenta lobes correspond to electron density accumulation/depletion.

the metal and the adlayer, the projection of every eigenstate onto the atomic orbitals of Si and H or F has been calculated and superimposed to all eigenvalues. For silicene/Ag(111), the contribution of Si orbitals is small but almost constantly spread on the bands, as expected from a strongly interacting system. As the coverage increases, and independent from H or F functionalization, such weights are more and more in-

on Ag(111)	**Si**	**hSiH**	**hSiF**	**SiH**	**SiF**
Δn_{SiX}	0.4	0.4	0.2	1.8	-0.2
Δn_{Si}	0.4	0.2	0.3	-0.3	0.1
Δn_{X_u}	-	0.2	-0.1	-0.0	-0.1
Δn_{X_d}	-	-	-	2.1	-0.2

Table 5.4: Charge differences Δn for silicene (Si), half silicane (hSiH). half-fluoro-silicane (hSiF), silicane (SiH) and fluoro-silicane (SiF) on Ag(111), expressed in number of electrons per cell, as calculated from Löwdin analysis. X_u/X_d label the H or F passivating atoms adsorbated on the upper/lower face of the silicene sheet.

tense, suggesting a more localized state onto the adlayer and therefore a less coupled interface. For silicane of fluoro-silicane the band structure is in good agreement with the bare superposition of the bands of the clean Ag(111) slab with those of free-standing silicanes. Such behavior is more evident around the Fermi level, since band gaps seem to appear, as highlighted in the calculated density of states of the full system and its projection onto the atomic orbitals of the adlayer, which is reported in Fig. 5.31. For silicene/Ag(111) the DOS is metallic, much different from the free-standing silicene, as expected. For half silicane and half fluoro-silicane the DOS diminishes around Fermi energy, but not completely: the adlayer behaves as a semi-metal. At full coverage, instead, the projection of the DOS on Si,H and Si,F orbitals shows that a band gap is opened of $\simeq 2$ and 0.5 eV, respectively, in good agreement with the values previously found in the free-standing systems.

5.4.3 Optical properties

The optical absorption spectra of the silicenes, adsorbed in the Ag(111) surface, are collected in Fig. 5.32: the total probability of absorption is decomposed into the transitions originating from and ending to atomic orbitals from different chemical species. This result can be obtained by extracting the projection of the Kohn-Sham eigenstates, from which the transition dipole matrix elements are calculated, onto selected atomic orbitals and insert those values as the weights W_l introduced in the equation 2.50 for the dielectric function. In this way it is possible to evaluate which fraction of the excitation takes place between Si states only, or between Ag states only, for example. In silicene/Ag(111), because of the strong hybridization of electronic states, the spectral features of the absorption observed in free-standing silicene and in the clean surface are

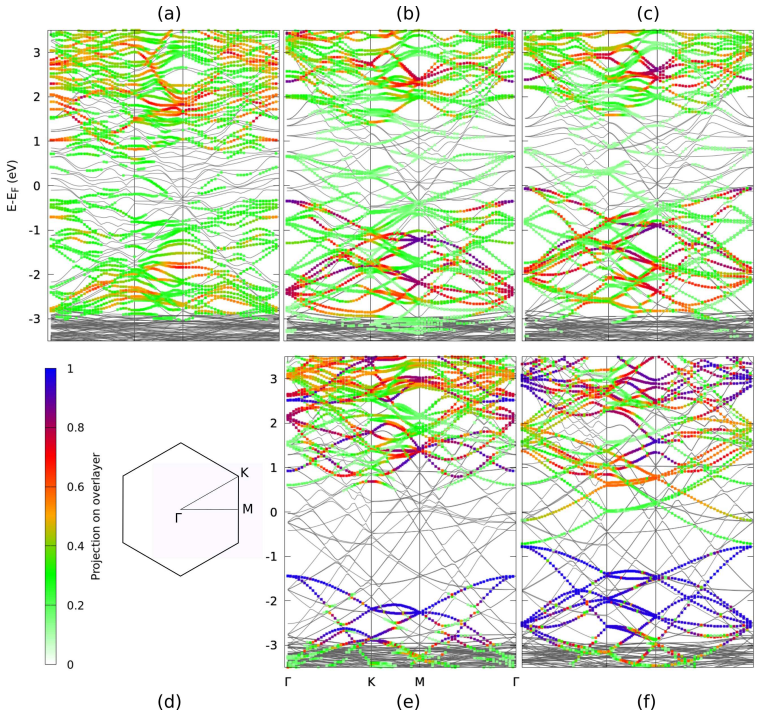

Figure 5.30: Band structure (gray lines) of silicene (a), half silicane (b), half-fluoro-silicane (c), silicane (e) and fluoro-silicane (f) after the adsorption on Ag(111). For each eigenvalue, the weight of the projection of the corresponding eigenstate onto the atomic orbitals of Si, H and F are reported, accordingly. The color scale of such weights and a schematic representation of the Brillouin zone of the system with the high symmetry path onto which the bands are calculated are reported in panel (d).

mixed together. This results is in good agreement with the one already discussed in Ref. [154] for the same system. The spectrum shows an important intraband component, more intense than the one calculated for the clean surface, because of the larger number of states created around the Fermi level. Additionally, a broad feature can be observed between 3 and 4 eV, in which the Si-to-Si component is weak and very different from the one calculated for the free-standing silicene. As the coverage is increased, the intraband component is progressively reduced to that of the clean slab, while the main absorption peak gets narrower and blueshifted. The Si-to-Si projection gets stronger and increasingly similar to that of the free-standing phase of the corresponding functionalized silicene. Such changes are better highlighted instead in the coverage-dependent comparison of the components of the absorption, which is presented in Fig. 5.33. In such a plot, for example, it is easier to track the absorption due to Ag-to-Ag transitions, which tend to agree with the one of the clean surface for the functionalized silicanes.

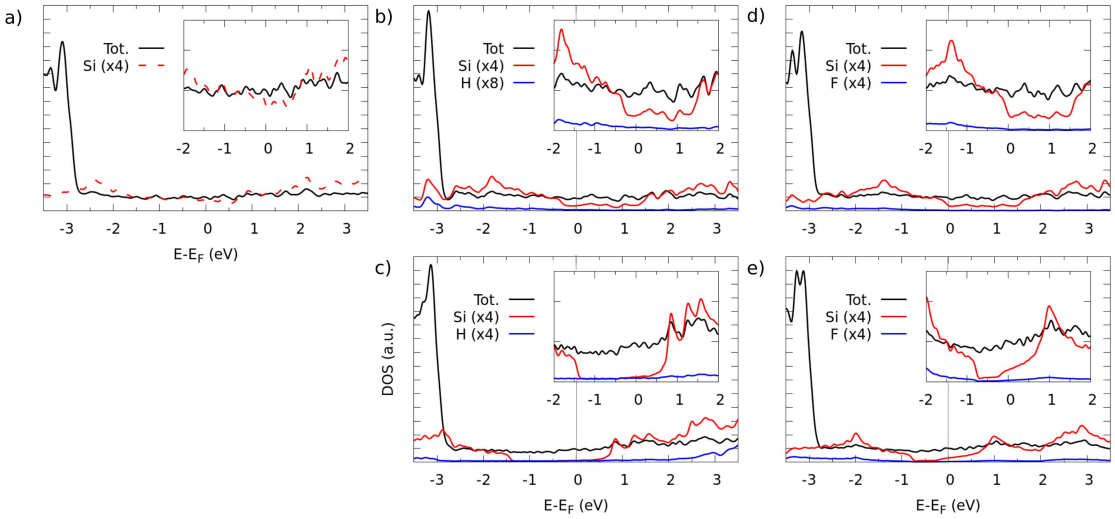

Figure 5.31: Density of states of silicene (a), half silicane (b) and silicane (c) after the adsorption on Ag(111). For each, a zoom around the Fermi level is given. Red/blue lines report the projection onto Si/H(or F) atomic orbitals, respectively.

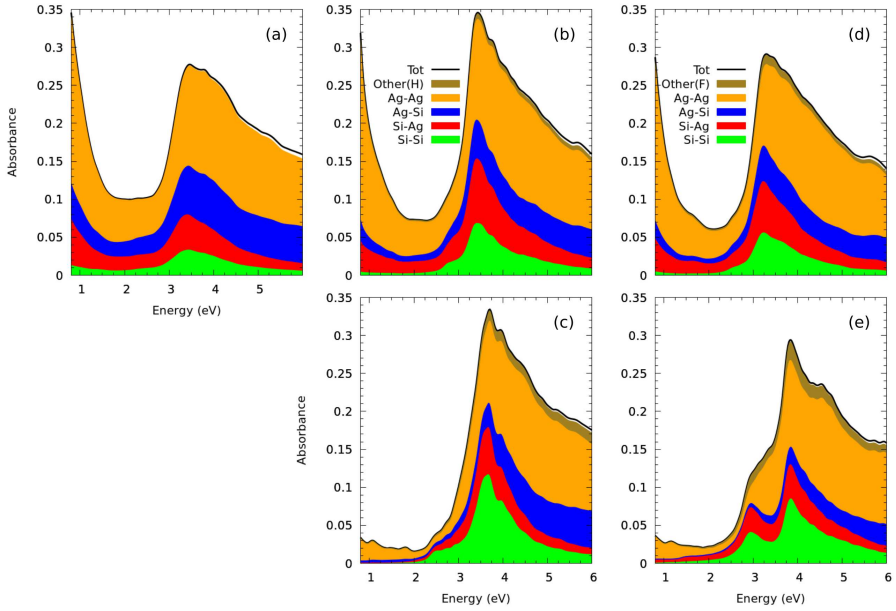

Figure 5.32: Comparison of the calculated optical absorption spectra for silicene (a), half silicane (b), silicane (c), half fluoro-silicane (d) and fluoro-silicane (e) adsorbed on Ag(111). For each system, the total spectrum is decomposed into the possible transitions localized onto atomic orbitals of different chemical species as initial/final states.

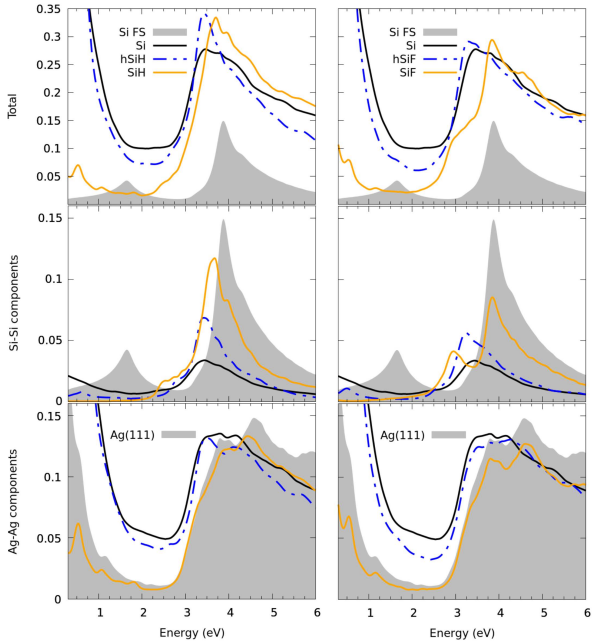

Figure 5.33: Comparison of the calculated optical absorption spectra for silicene (a), half silicane (b), silicane (c), half fluoro-silicane (d) and fluoro-silicane (e) adsorbed on Ag(111). Each panel compares the coverage-dependency of a selected component of the absorption spectrum.

The results collected up to this point are not still giving a definitive insight on the strength of interaction between the adlayer and the metal, since the two pristine systems have very strong absorption peaks in the same energy position. Therefore we further investigated it by calculating the cumulative spectral intensities and their projection onto the atomic orbitals of the overlayer, which are collected in Fig. 5.34. In all low-energy transitions below 1 eV, it is possible to verify that the contribution from the overlayer is almost disappearing as the degree of passivation is increased, as expected from a less coupled interface. At the same time, at the absorption frequencies characteristic of the free-standing overlayers, the transitions can be seen to be more intense in the projection of the spectral intensity, confirming that the degree of hybridization is reduced.

If the reflection is investigated instead of the absorption, the SDRS spectra calculated for the functionalized silicene phases adsorbed on Ag(111) are collected in Fig. 5.35. In all systems, the reflectivity is reduced between 5-10% for energies around 3 eV, however the shape of SDRS at low coverages differs from that at full coverage. In the former, for energies below 3 eV, the reflectivity is decreased, while it is higher than the one of the bare substrate for energies larger that 3 eV. In the latter, namely silicane and fluoro-

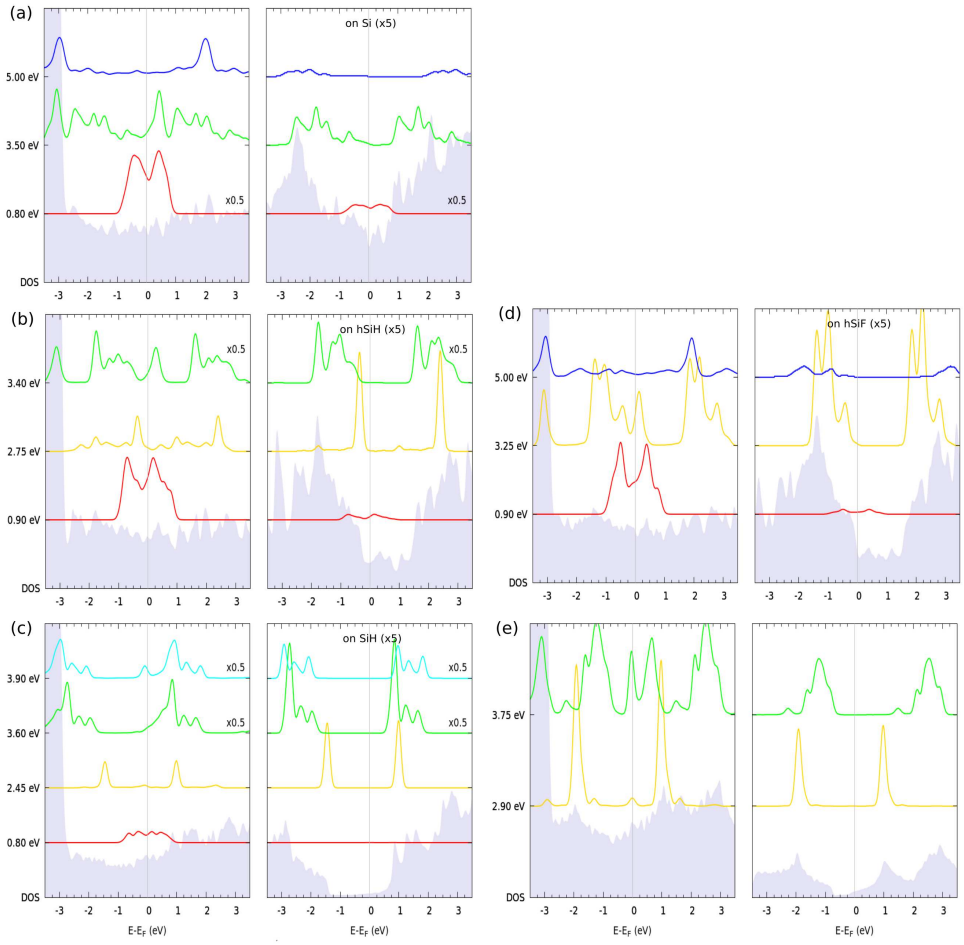

Figure 5.34: Comparison of the cumulative spectral intensities for silicene (a), half silicane (b), silicane (c), half fluoro-silicane (d) and fluoro-silicane (e) adsorbed on Ag(111). For each system, the left panels report the total intensities and the right panels report the projection of the transition dipole matrix elements (and of the DOS) onto atomic orbitals of Si and H/F.

silicane, around 3 eV a broad negative feature can be observed, while the reflectivity is almost unchanged elsewhere. Such difference in spectral shape is a first fingerprint of a different level of passivation of silicene. The origin of this behavior can be identified by investigating the two component which form the SDRS signal, as they are related to changes in the real or in the imaginary part of the dielectric function. In the first case, up to 3 eV the main contribution to SDRS comes from an increase in the absorption, while above that energy the main contribution is related to a reduction in the real part of the dielectric function. It is possible to propose an explanation of this fact by considering

the Drude model described in Sect. 2.4.3, as it can be done in a similar fashion in the investigation of the density of a material for strained systems [171] or of the effect of ionic collisions [172] using the Lorentz-Lorenz relationship (assuming an homogeneous electronic response for every atom). For the results reported in this work, the lowered dielectric function would cross the origin at an energy higher than that of the clean substrate. That would correspond to a blueshift of the plasma frequency which, within the Drude model would correspond to an increased number of metallic electrons, which agrees with the effect of the strong interaction taking place between Ag and the adlayer. Conversely, for the case of silicane and fluoro-silicane, the increase in absorption is paired by a reduction in the number of metallic electrons, as the real component of the dielectric function shows an increase after the adsorption of the functionalized silicenes.

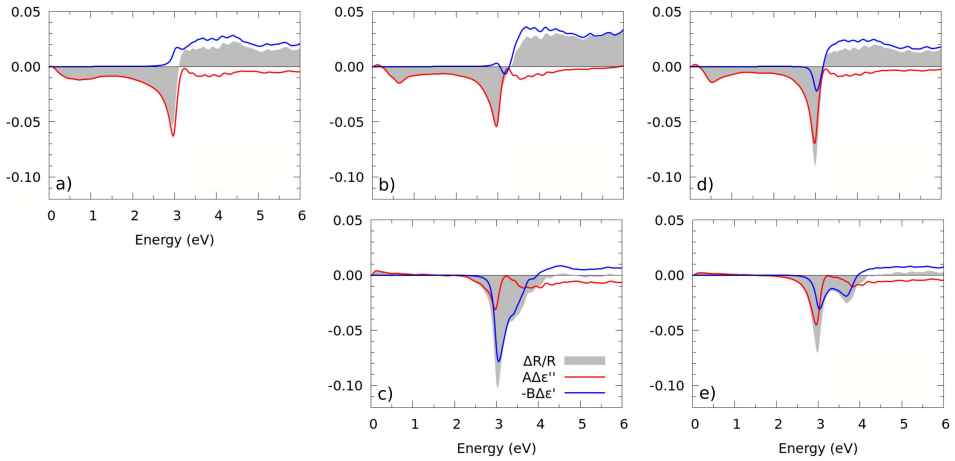

Figure 5.35: Comparison of the surface differential reflectivity spectroscopy for the adsorption of silicene (a), half silicane (b), silicane (c), half fluoro-silicane (d) and fluoro-silicane (e) on the clean Ag(111). In each panel, the two components which are summed to obtain the full SDRS spectrum are reported. The A and B functions are the ones described in Fig. 5.25.

5.5 Conclusion

In this work, the electronic properties of a two dimensional system, a silicene layer functionalized with single H or F adatoms, adsorbed onto the (111) surface of Ag and their coverage dependency have thoroughly studied. The aim of the investigation has been to theoretically characterize such systems through optical spectroscopies, namely absorption and reflection at normal incidence. As the ground state of each system is

constructed and optimized through DFT simulations, the excited states are taken into account by calculating the macroscopic dielectric function within the many-body perturbation theory under the independent particle - random phase approximation framework. The investigation is focused first on the unsupported phases of functionalized silicene, where the role of the adatoms is seen to be the removal and the shift of the electronic states related to the Dirac cone in silicene. Moreover, the new states form a band, the alignment of which depends both on coverage and the chemical species of the adatom; in same cases a band gap of different size is opened in the structure. Such changes are then correlated with the shape of the absorption spectrum and the contributions of each pair of valence and conduction band states is addressed through the investigation of the spectral intensities, which are calculated from the transition dipole matrix elements. Such investigation allows to directly connect the shape of the band structure with the peaks in the absorption spectrum and, for the free-standing systems, several unique fingerprints can be identified. The study then focuses on the adsorption of such functionalized silicene onto the (111) surface of Ag. The geometrical parameters from the optimized configurations and their energetics have been inspected and several trends have been identified suggesting a mixed chemical/physical nature of the interactions at the surface, with a weakening of the coupling with the surface as the silicene overlayer is more passivated. Such hypothesis is further supported by investigation of the electronic properties of the systems, namely band structure, density of states and charge transfer. The optical characterization through the absorption spectrum is performed, in which the shape of the spectra and their decomposition is investigated, with the aid of the calculated spectral intensity, in order to address the single Si-to-Si or Ag-to-Ag transitions. As the interaction between the metal and the adlayer is weakened, a reduced low energy absorption is observed as well as an increased agreement with the aforementioned components with the free-standing results. Finally to fully address such systems from an experimental point of view, the reflectivity spectrum is worked out as differential spectroscopy. In this case, the calculated results suggest that within such technique the differences both in coverage and in functionalization can be experimentally resolved.

Chapter 6

2D vs 3D: Silicon reconstruction on NaCl/Ag(110)

6.1 Introduction

In the previous chapter, the two-dimensional honeycomb of Si atoms, called 'silicene', has been introduced as an appealing material for opto-electronic applications, because of the formation of a peculiar structure, the Dirac cone, around the Fermi level. Such a behavior is directly connected to the sp^2 hybridization of Si atomic orbitals; experimentally, silicene may be obtained through epitaxial growth on those substrates with proper lattice matching, for example Ag [173–175], Au [176, 177], ZrB_2 [178] or Ir [179]. For all those cases, a strong interaction of silicene with the metal surface is reported [154, 180, 181], which destroys the Dirac cone; because of the reported hybridization of the states at the interfaces, even the results regarding the band structure of those systems [182, 183] had to be looked again with a new perspective. These evidences question whether the actual reconstruction of Si atoms can be rightfully called 'silicene'. For example, in the previous chapter, the investigation of functionalized silicene confirmed that the main culprit of such behavior is the reactivity of Si atoms themselves, which tend to prefer the sp^3 hybridization scheme for their orbitals, instead of the almost pure sp^2 of silicene. The research for the synthetization of the ideal silicene therefore moved, in recent years, to search other potential candidates of good growth substrates among those with more insulating character. In particular, alkali metal halides such as NaCl, have shown to effectively act as neutral spacers, allowing to decouple the electronic states of adsorbed species from those of the metallic substrate [184–186]. Moreover, the growth of an ordered and large area thin film of NaCl has already been reported in literature very

recently on the Ag(110) surface [187].

This work started during my secondment at the University of Central Florida in Orlando (US) in collaboration with Prof. A. Kara; this ongoing investigation aims to determine, through first-principles methods, the correct structural model for the reconstruction of Si atoms deposited the NaCl/Ag(110) substrate. Part of the computational resources used for this study have been granted through the ISCRA C project SNCA - HP10C0JWZW.

6.2 Experimental data

The investigation relies on a set of experimental measurements, worked out by one of Prof. Kara's collaborators, Dr. Oughaddou, (ISMO-CNRS, Université Paris-Sud, Orsay (FR)) and co-workers [188]. On the clean Ag(110) surface, first the NaCl monolayer is grown, then Si atoms are deposited on the substrate; the sample has been monitored through several techniques to characterize the surface by structural and chemical means. The crystallographic structure of the sample has been verified at each deposition step

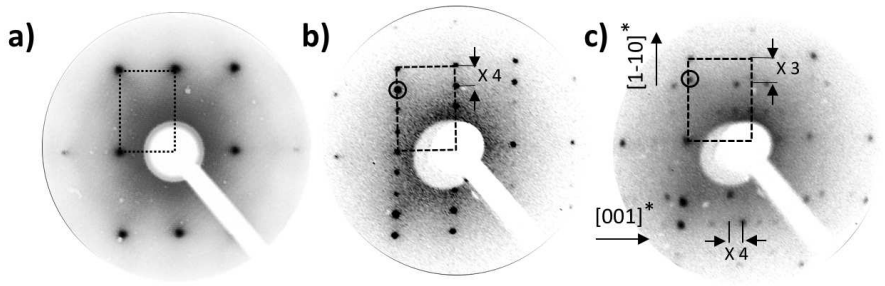

Figure 6.1: Experimental LEED patterns of (a) bare Ag(110) substrate, (b) after a deposition of $\sim$ 1 ML of NaCl, (c) after the deposition of $\sim$ 1 ML of silicon on NaCl/Ag(110), recorded at an energy of 70 eV. Brillouin zone of the Ag(110) unit cell is highlighted in all panels by a rectangle with dashed lines. The circle in panel (b) and (c) marks the diffraction spot originated by the formation of NaCl crystalline lattice. In panel (c) the periodicity of Si reconstruction is reported. Images taken from Ref. [188].

by observing the formation and the evolution LEED patterns, which are reported in Fig. 6.1. The diffraction spots of the clean Ag(110) surface are identified and monitored during the growth of subsequent layers to address the periodicity of their reconstructions. As already known from literature [187], the monolayer of NaCl forms a rectangular-cell lattice which is $4/3 \times 1$ times the unit cell the Ag(110); the same diffraction spot is observed as the Si atoms are deposited, suggesting that its structure is preserved during

the growth of Si phase. The new overlayer self-assembles in an crystalline fashion, with a (3×4) periodicity.

The topography of the self-assembled Si atoms deposited on top of NaCl/Ag(110)

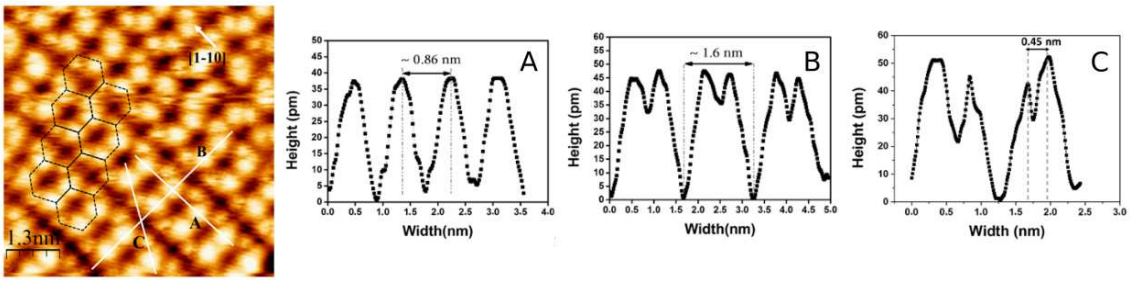

Figure 6.2: Experimental high-resolution STM images corresponding to 1 ML of silicon deposited over the NaCl film (6.5×6.5 nm^2, V_{bias}= -0.04 V,I= 2.6 nA). The height profiles extracted from the line scan along A,B and C transepts are reported in the right side panels of the figure. Images adapted from Ref. [188].

substrate is investigated through STM imaging, as shown in Fig. 6.2. A regular superstructure of spots can be observed, the periodicity of which matches the (3×4) one extracted from the diffraction pattern. The line profiles measured between the structure of the spots indicate a smooth surface, with a buckling of the order of 0.4 Å. Despite the hexagonal arrangement of the spots, their distances are not symmetric, as the sides of the polygon are ∼ 7.0 and 4.5 Å long; moreover, two sizes of the spots can be distinguished, which can be estimated from the FWHM of the peaks in the line profiles as 3.5 and 1.5Å. Therefore the STM topography doesn't resolve individual atomic orbitals.

Additional structural information can be extracted from the analysis of the EXAFS

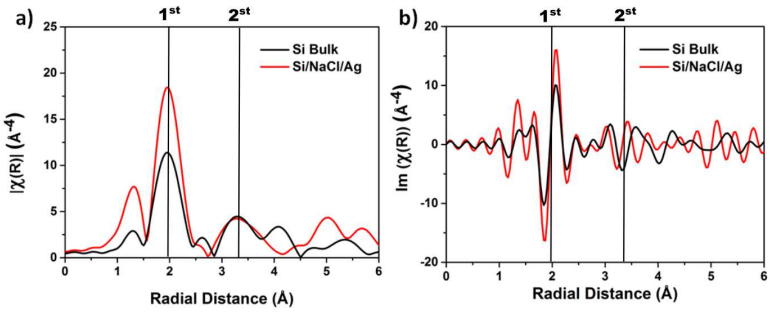

Figure 6.3: Experimental (a) modulus and (b) imaginary parts of the Fourier transform of the oscillatory component χ of the x-ray absorption spectrum of bulk silicon and 2D Si sheet deposited on NaCl/Ag(110). The marked peaks correspond to the first and second neighbor distances between Si atoms are marked. Images taken from Ref. [188].

spectrum, for which the Fourier transform of the oscillatory component of the x-ray absorption spectrum is reported in Fig. 6.3 for both its modulus and phase. The points of constructive interference correspond to the average of first and second neighbor Si-Si distances; the collected EXAFS spectrum is in good agreement with the spectrum measured for bulk silicon, and the values of 2.35 and 3.83 Å, respectively, can be extracted for the interatomic distances. The chemical structure of the sample is investigated through

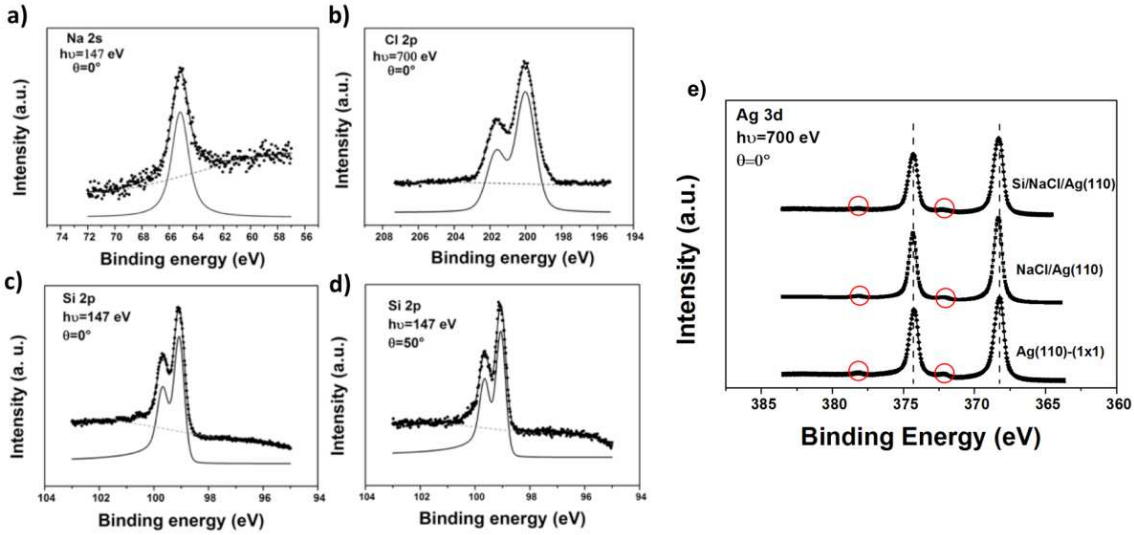

Figure 6.4: Experimental XPS spectra at (a) Na 2*s* edge and (b) at the Cl 2*p* edge, after the growth of the NaCl film. Panel (c) and (d) report the spectra at Si 2*p* edge, measured at two different photo-emission angles, measured after the deposition of Si atoms. Panel (e) shows the XPS spectrum at the Ag 3d edge, collected during different stages of the epitaxial growth. The red circles mark the plasmon peaks of Ag. Images adapted from Ref. [188].

the XPS spectroscopy as the core level of the different chemical species are selectively excited; the resulting spectra are shown in Fig. 6.4. The binding energy of Ag core states doesn't show any appreciable changes as Na, Cl and Si atoms are deposited, suggesting that the interaction between the different layers is weak. The doubly-peaked spectrum in $2p$ states is an expression of the spin-splitting of such orbitals between $h = l - 1/2$ and $h = l + 1/2$ and can be interpreted with the presence of a single chemical environment. Therefore either Na, Cl and Si atoms do not show sign of chemical bonding between different species.

Globally these results suggest the formation of a silicene-like overlayer, namely almost flat and with Si atoms experiencing only one kind of local charge, although the topog-

raphy of such surface doesn't correspond to the one of silicene.

6.3 Investigation of the reconstruction

To try solving the puzzle of the reconstruction of Si atoms, their self-assembly has been investigated through a multi-scale approach, where each set of simulations targeted a specific property. The simulations have been carried out using both VASP or QuantumEspresso codes; in the former through the optB88-vdW-DF functional [189] which includes the dispersion forces through a non-local functional term, while in the latter the PBE has been employed, along with the Grimme D2 Van der Waals pairwise term. The Ag(110) substrate has been constructed as a slab with four layers, based on an optimized bulk lattice constant a_0 of 4.145 Å when calculated in VASP and of 4.164 Åwhen calculated with QuantumEspresso. The NaCl/Ag(110) substrate has been constructed based its most stable (4×1)/(3×1) phase, as discussed in literature [187]. Because of the periodicities observed for the NaCl and Si thin films, the minimal supercell that has to be constructed for simulating the complete system has a size 12×4 times the Ag(110) unit cell. Given the computation load required to work with such a model, an accurate screening of the candidates has to be carried out before relaxing them through DFT calculations. Because of the same reason, the simulations have been interrupted before achieving a full convergence of the forces in those cases where the resulting configuration or STM profile didn't match the experimental results.

6.3.1 Lattice matching

As a first approach to identify the correct reconstruction model, the most promising structures to be optimized have been searched among those with best lattice matching with the substrate. The lattice of the Ag substrate has been constructed as well as that of NaCl, and those structures have been compared with the pattern of bright spots observed in the STM measurement, as shown in Fig. 6.5: as expected from the different periodicities, no matching can be observed with the NaCl structure.

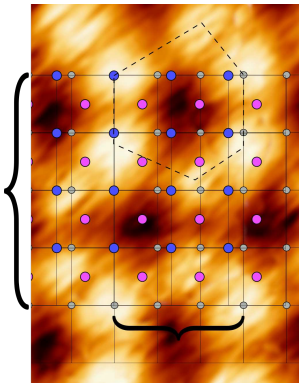

Figure 6.5: Comparison of the lattice of NaCl/Ag(110) substrate with the one experimentally measured with STM, from Ref. [188]. The pattern of the STM spots is highlighted with a dashed-line hexagon. The grey circles represent Ag atoms from the first layer, blue circles Cl atoms and magenta circles Na atoms. The curly brackets remark the periodicity of the Si reconstruction.

Regular silicene

Similarly, the regular silicene lattice has been constructed and compared with the one of the bare Ag(110) and the experimental one; no comparison with NaCl film structure seems necessary, as shown before. These structures have been overlapped, even allowing the two layers to be rotated one with respect to the other, to find the configuration with minimal strain. Different buckled phases of silicene (as discussed in the previous chapter), namely the low buckling (LB) and high buckling (HB) ones, have been taken into account: some examples are reported in Figs. 6.6 and 6.7 respectively. As those two figures show, Ag(110) surface and silicene hardly match their lattices, because of the different sizes and symmetries; moreover the additional agreement of silicene with the experimental STM spots is non-straightforward. In the reported examples, the best matching, coming from the rotated silicene LB lattice, has a compressive strain of 13.2% and 9.5% along the two directions. In the other two cases, the periodic structures overlap at longer distances, hence requiring a larger strain to fit the periodicity observed experimentally. Considering a regular lattice of silicene as a building block, four configurations have been optimized and are reported here, which are shown in Fig. 6.8. The first two reported the figure have been constructed from the non-rotated LB silicene; the one in panel (a) is relaxed as-is while the one in panel (b) has been first optimized in free-standing, before putting it on the substrate. The former configuration ends in a stable geometry, where however one row of Si atoms is subsided under the neighboring

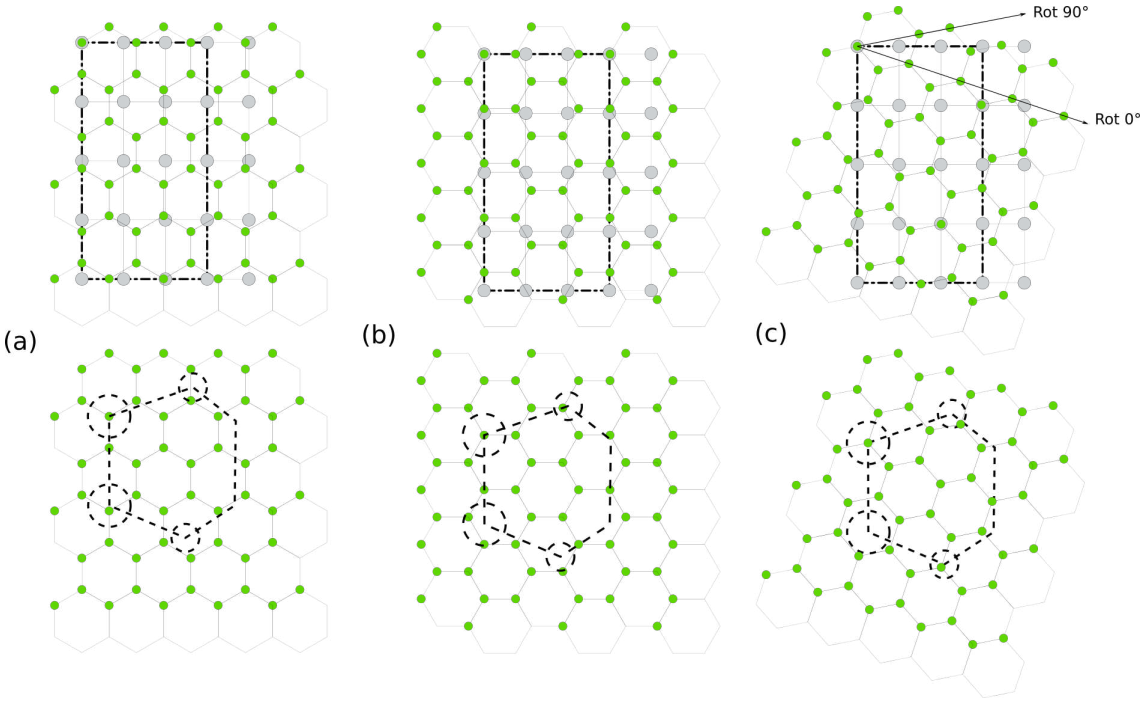

Figure 6.6: Lattice models of Ag(110) surface and LB silicene for three different relative orientations of the structures: (a) 0°, (b) 90° and (c) -18.6°. The reference angles are reported in panel (c). The green circles mark Si atoms, the gray ones mark the Ag atoms from the first layer. The upper panels show the matching of Ag and Si lattices, where the (3×4) periodicity is reported as a dot-dash line rectangle; the lower panels compare the silicene lattice with the experimental periodicity, marked by the dashed line hexagon. The circles reported in there, mark the size of the STM spots.

one and a ripple is formed. The atoms along such ripple are buckled $\pm \sim 1$ Å in an alternate fashion, with respect to the average of Si layer. This result is much different from the reference experimental pattern. The latter configuration instead already starts with a ripple, even though the Si atoms are all buckled upward by ~ 1 Å. Its optimized configuration is not a stable one, as Si atoms seem to aggregate in an amorphous layer. The third configuration, as reported in Fig. 6.8(c) has been constructed from the HB silicene rotated by 90°; despite the relatively good matching of Si/Ag lattices, the structure relaxes towards an amorphous structure. The last configuration reported in Fig. 6.8(d) has been constructed from a LB silicene rotated by -10.9° and already optimized in FS, which matches the whole 12×4 supercell (not the 3×4 one though): the configuration is stable, although the formation of wave-like corrugations can be observed, triggered by the compressive strain acting on the lattice. As an additional regular structure, the

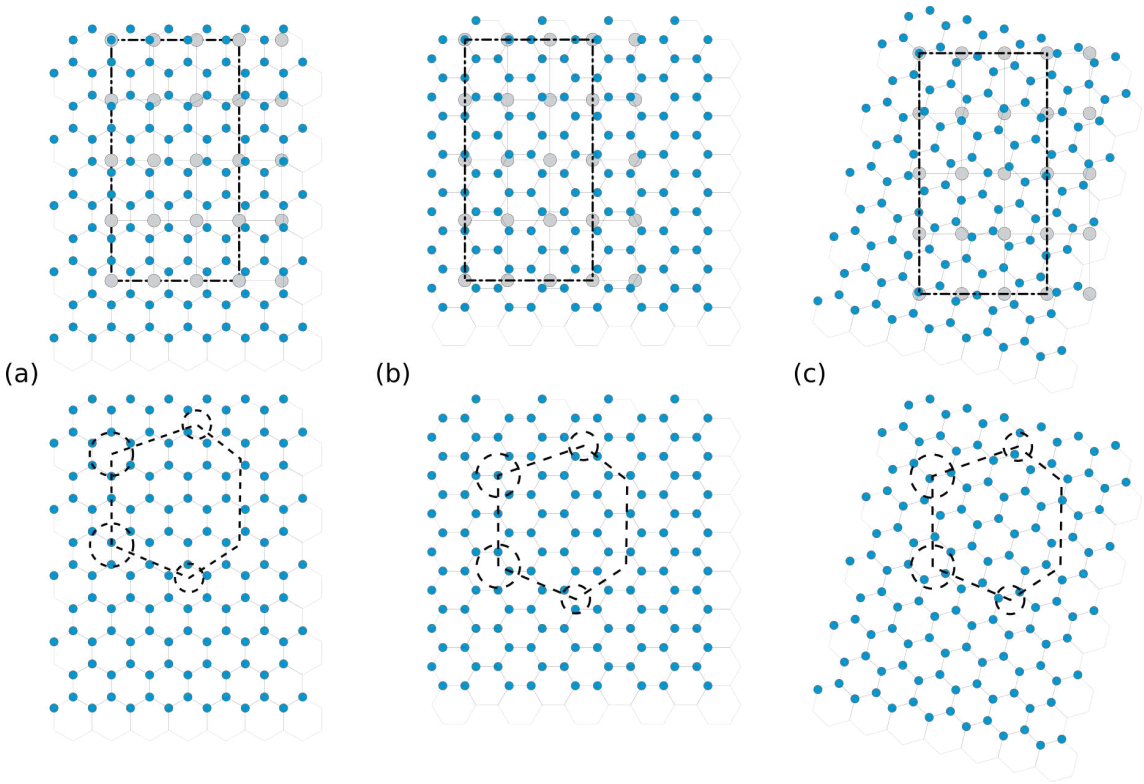

Figure 6.7: Lattice models of Ag(110) surface and HB silicene for three different relative orientations of the structures: (a) 0°, (b) 90° and (c) -14.0°. The reference angles are reported in panel (c) of Fig. 6.6. The blue circles mark Si atoms, the gray ones mark the Ag atoms from the first layer. The upper panels show the matching of Ag and Si lattices, where the (3×4) periodicity is reported as a dot-dash line rectangle; the lower panels compare the silicene lattice with the experimental periodicity, marked by the dashed line hexagon. The circles reported in there, mark the size of the STM spots.

dumbbel (DB) reconstruction has been investigated as one of the most stable modified phases of silicene [190–192]. Its structure, as shown in Fig. 6.9, has been constructed by setting the different bond-lengths equal to those of 1st and 2nd neighbors in silicene/bulk Si, as experimentally observed; the relaxation in this case is carried out for the unsupported layer, optimizing also the lattice vectors. The model for this reconstruction is similar to that of LB silicene, therefore not matching the (3×4) Ag periodicity, although with a much different buckling.

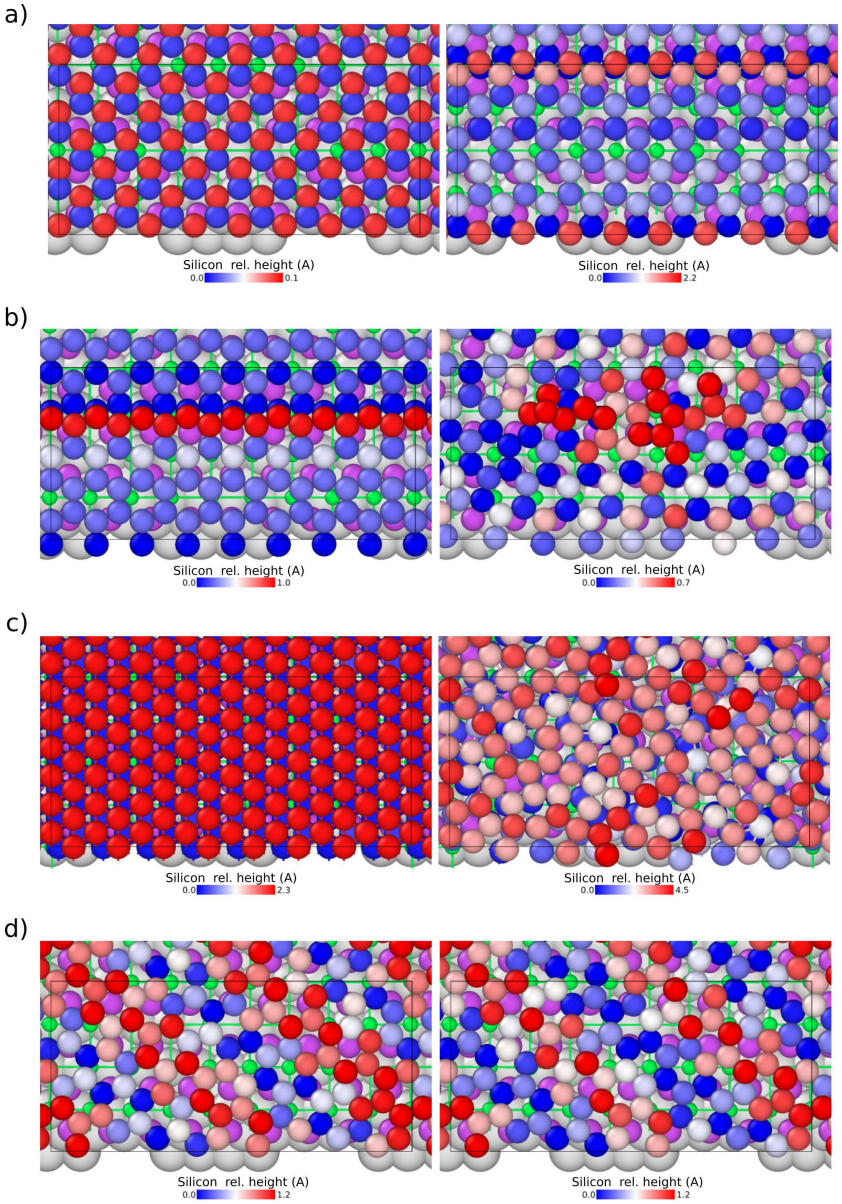

Figure 6.8: Initial (left) and final (right) snapshots of the optimization of four configurations constructed from regular silicene lattices, adsorbed on NaCl/Ag(110) substrate. (a) LB silicene first optimized in FS, (b) LB silicene and (c) HB silicene rotated by 90° and (d) LB silicene, rotated by -10.9°. Ag atoms are represented by grey spheres in background, Na and Cl atoms by purple and green spheres, respectively. The Si atoms are reported with blue-white-red spheres, the color of which depends on the buckling of the layer; the color code is reported at the bottom of every image. The supercell is shown as a black rectangle.

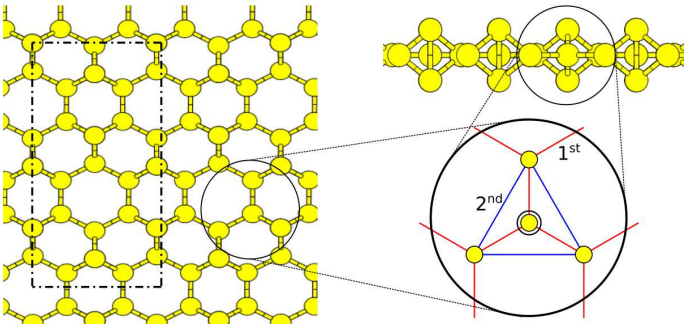

Figure 6.9: Representation of the optimized model for the dumbbell silicene. The left and right panels report the top and front view of the structure. The (3×4) Ag periodicity is reported by a dot-dash rectangle. In the zoomed area, the different bond lengths through which the model has been constructed are reported, corresponding to the silicene 1st (red lines) and 2nd (blue lines) neighbors distances. The circled atom on the middle of the triangle marks the position of the upwards/downwards distorted atoms.

Defective silicene

To try reducing the strain in the silicene overlayer, induced by the Ag lattice, the inclusion of defects in the honeycomb structure have been taken into account. In a first case, the non-rotated LB silicene has been modified by removing either one row of zig-zag atoms or a single bond from the configuration including 3 repeated (along y direction) hexagons. As seen in Fig. 6.6, such structure can fit the (3×4) periodicity observed experimentally along the x axis with some strain, but the mismatch along the y axis is important. The candidates reported in Fig. 6.10 a) - b) are constructed by removing an entire line of Si atoms from the reference structure; the two cases differ only by the relative position of the overlayer with respect to the substrate. The candidate reported in Fig. 6.10 c), instead, is constructed by removing the bond connecting the last and first hexagons in the reference geometry. The optimized configuration of such systems is indeed a stable one, with one or two lines of Si atoms upward buckled with respect to the rest of the layer. The magnitude of such a dislocation is $\sim$ 1.3, 0.4 and 0.7 Å, respectively; their pattern partly agree with the bright spots in the experimental STM. Comparing the latter with the simulated image from the three configurations, reported in the right side of the panels of Fig. 6.10 the agreement is not good; the better match is observed for the last candidate, but even in that case the height of the simulated features is much larger than the experimental buckling.
To further inspect defective structures, the effect of single or double vacancies has been

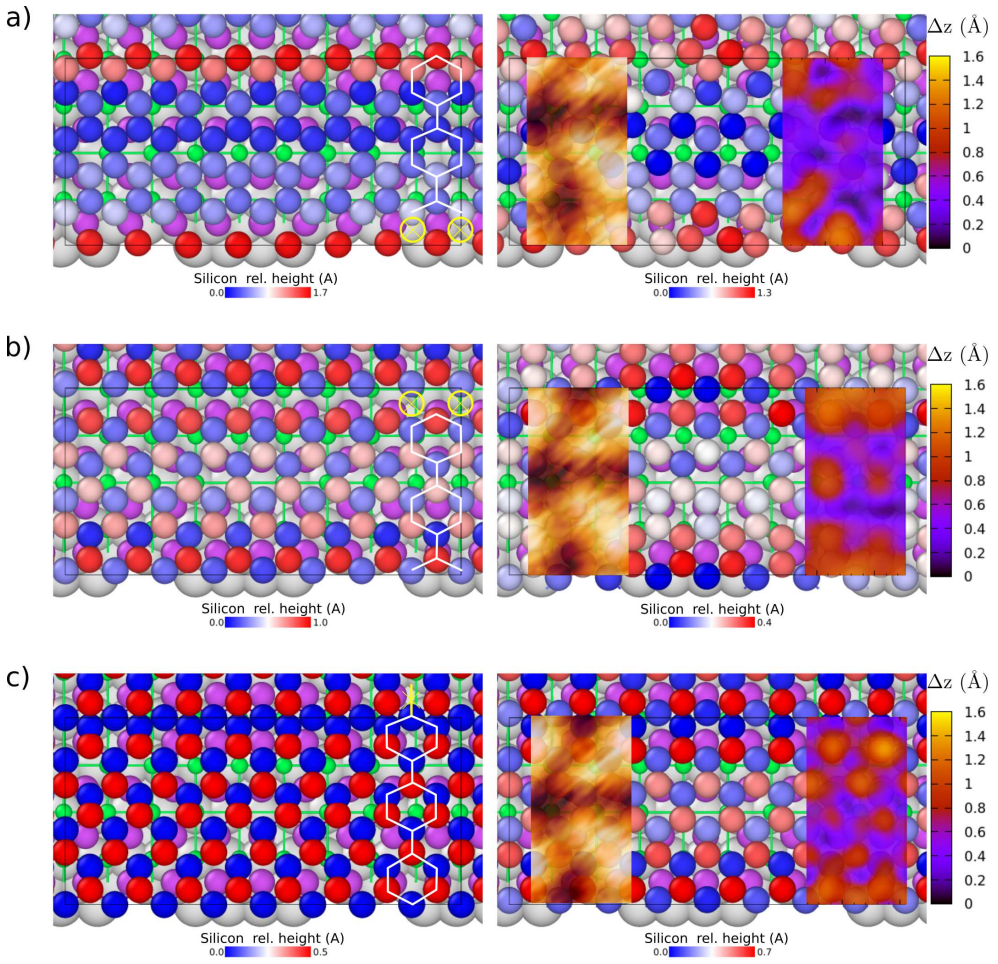

Figure 6.10: Initial (left) and final (right) snapshots of the optimization of the configurations constructed from silicene lattices with a missing row, adsorbed on NaCl/Ag(110) substrate. The structure of Si atoms is reported in the left panels through white lines; the crossed yellow circles/stick highlight the position of the removed atoms/bond. In the panels on the right, the structural models are overlapped with the experimental STM (inset, left rectangle, from Ref. [188]) and with the calculated STM (inset, right rectangle). With Δ z, the calculated V_{bias}=-0.04 V STM height is reported for an isovalue of 0.00001 states/Bohr^3. Ag atoms are represented by grey spheres in background, Na and Cl atoms by purple and green spheres, respectively. The Si atoms are reported with blue-white-red spheres, the color of which depends on the buckling of the layer; the color code is reported at the bottom of every image. The supercell is reported as a black rectangle.

taken into account [193] by relaxing both the atomic coordinates and the axes of the

supercell. To reduce the computational load, such optimizations have been carried out without the substrate: from a 5×5 silicene one or two atoms have been removed, as shown in Fig. 6.11. In case of a double vacancy, four different configurations have been taken into account, in which the defects affect inequivalent nearby sites. All configura-

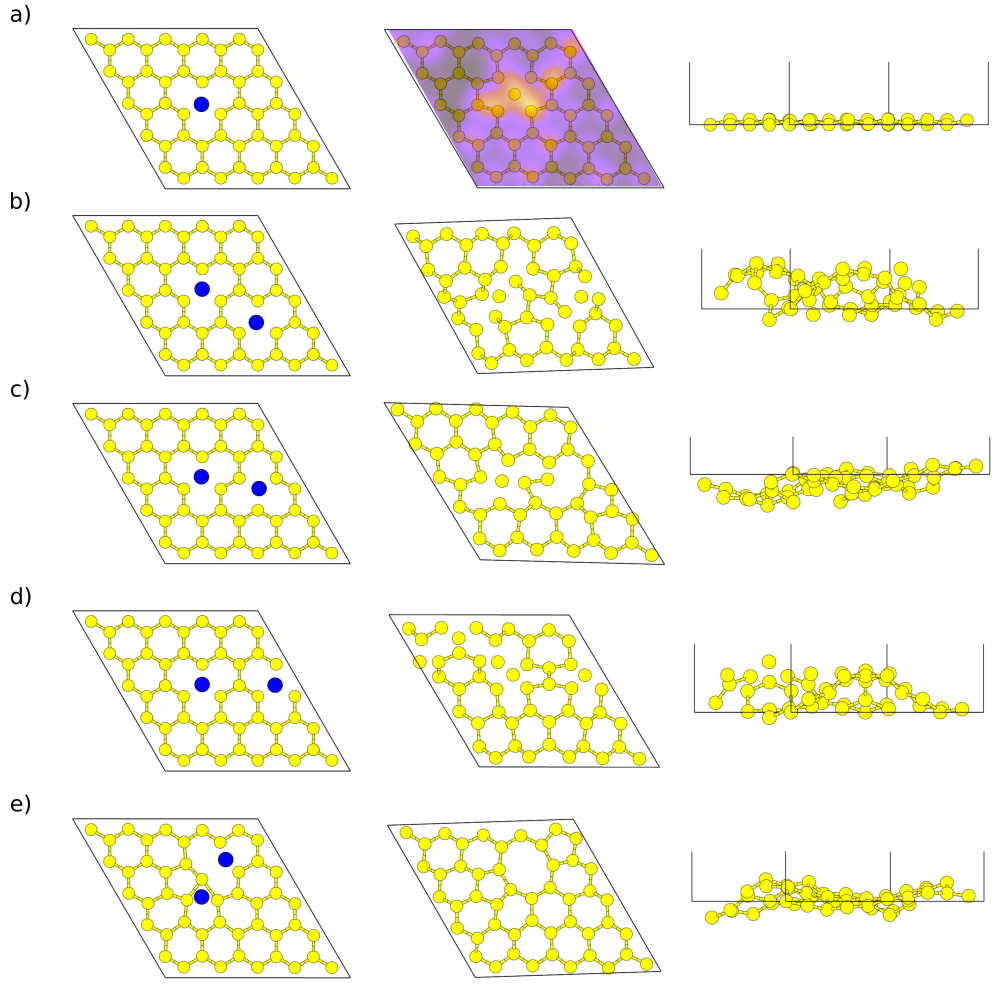

Figure 6.11: Initial (left panel) and final (middle and right panels, top and front view, respectively) snapshots of the optimization of the 5×5 silicene with single (a) or double (b-e) vacancies. Si atoms of the lattice are shows as yellow circles, the removed atoms are shown as blue circles. For the single vacancy, the simulated STM image at $V_{bias} = -0.04$ eV is overlaid on the top view of the relaxed structure.

tions are equally stable, within the numerical accuracy of the simulation, as far as the formation energy is concerned. The structure of the layer with a single vacancy is almost flat; its simulated STM image at the experimental bias shows a broad spot, which can

be compatible with the size of the bright spots observed in experiments. Its lattice, however, and the corrugation of the other optimized structure, cannot match the (3×4) periodicity of Ag substrate.

Silicene nanoribbon

As more regular arrangements of Si atoms do not seem able to reproduce the geometrical features of experimental findings, the formation of nanoribbons has been investigated. In analogy of the structures formed directly on the Ag(110) surface [194, 195], these ribbons would be ideally infinite in length along x axis, namely the $[1\bar{1}0]$ direction of the Ag surface, but with a width of few atomic-lines along the y axis or the [100] direction of the substrate. The detailed structure of the ribbon, however, strongly depends on the growth conditions and its optimized configurations can be dramatically different from the silicene hexagonal structure [196–198]; all such structures, however, are driven by the strong interaction with the Ag. Here, on the NaCl/Ag(110) substrate, the self-assembly of Si atoms must be correlated only to the periodicity induced by the Ag lattice, as not signs of interlayer interaction could be spotted. However, as the defective silicene investigated in the previous section, the loss of translation invariance along y direction can help to stabilize the structure and overcome the lattice mismatch. Therefore three configurations have been constructed and optimized on the NaCl/Ag(110) substrate, as shown in Fig. 6.12, including zig-zag nanoribbons made of four silicon chains of atoms, which have been reported as the most stable ones compared with those of larger height [199]. The first two have been cut from LB silicene and have different positions with respect to the underlying substrate, namely there is a different matching between the Cl atoms and the center of the hexagons of silicene. In this case, as suggested in the defective silicene, the mismatch of silicene with the NaCl film drives the formation of a stable overlayer, otherwise the ribbons seems to break up. However, even for the stable structure, the simulated STM at $V_{bias} = -0.04$ V doesn't agree with the experimental one: not only single atoms are imaged, but the lowest height of the charge density, which forms a darker stripe which can actually be observed even in experiments, would result in a too buckled profile. The last configuration, instead, is constructed from cutting the ribbon from the DB silicene, hence with a different buckling and Si bond length that the previous case.
In this case, the ribbon is shrank along the y direction; because of that, the simulated STM has an excessive buckling, even though the structure of the spots partly agree with the experimental one.

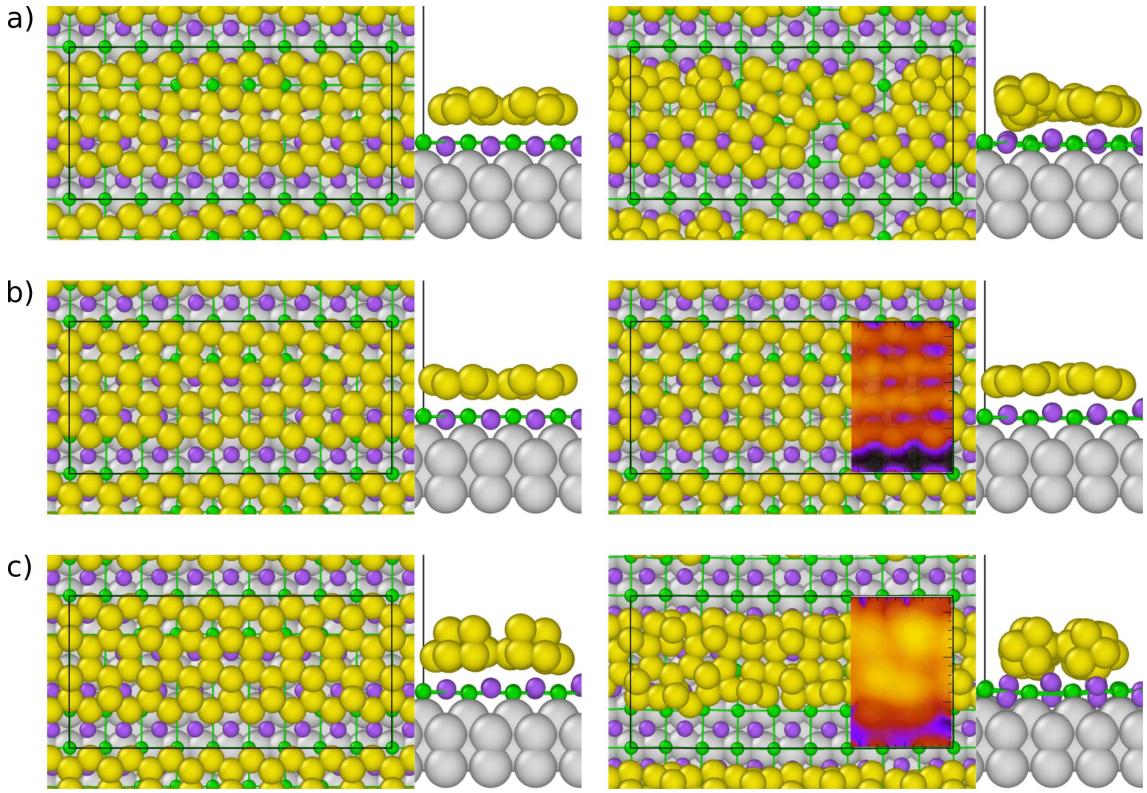

Figure 6.12: Initial (left panels) and final (right panels) snapshots of the optimization of different silicene nanoribbons adsorbed on the NaCl/Ag(110) substrate: (a)-(b) based on LB silicene and (c) based on DB silicene. The configuration of (a) and (b) differs by the relative position with respect to the underlying surface. Top and left views are provided for each configuration. Si atoms are reported as yellow spheres, Ag atoms are represented by grey spheres in background and Na and Cl atoms by purple and green spheres, respectively. In panels (b) and (c) the simulated STM image for the experimental bias (isovalue 10^{-5} and 10^{-6} states/Bohr^3, respectively) is overlaid on the final top view structure; its color scale indicates the height along z and goes from black ($z = 0$) through purple ($z = 1/z = 0$) and red ($z = 2/z = 3$) to orange ($z = 3/z = 5$). The supercell lattice is reported as a black rectangle.

6.3.2 Investigation of Si self-assembly

As the direct optimization of potential candidates for modeling the reconstruction of Si atoms deposited on the NaCl/Ag(110) substrate didn't show any promising pattern, another approach has been taken in to account. In this case the self-assembly process itself of Si atoms has been studied, first in static way, i.e. characterizing the adsorption of a single atom onto the clean substrate, and then extend such information with dynamical

evolution of a cluster of atoms.

The structure of the NaCl/Ag(110) is already known from literature [187], but it is useful to extract its electronic properties, which are shown in Fig. 6.13, namely the shape of the charge density and the density of states. The former shows that there is no additional modulation of the charge is space other than that of the (4×1) periodicity, while the latter describes the nature of the interaction between the two layers at the interface, as Ag-Cl bonds are formed. Therefore a single Si atom can be expected to weakly interact to Na atoms only and experience a potential with rectangular symmetry.

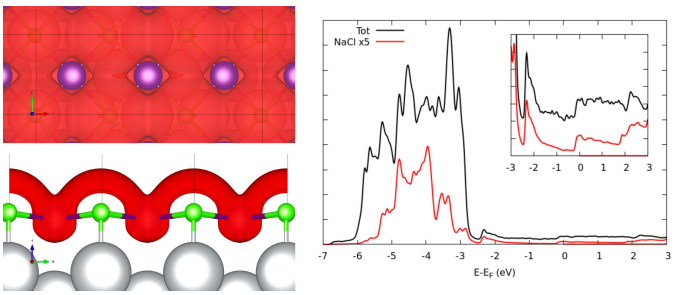

Figure 6.13: Electronic properties of bare (4×1) NaCl/Ag(110) substrate: the left panels report the electron density (for an isovalue of 0.002 e^-/A^3) as a red surface, from top and front views. Na/Cl atoms are shown as purple/green spheres, Ag ones as gray spheres. The supercell is drawn as black lines. The density of states is reported in the right panel. The projection onto Na and Cl atomic orbitals is reported as a red line. The inset shows a zoom of the DOS around Fermi energy.

As shown in Fig. 6.14, several sites for adsorbing a single Si atoms have been taken into account. For each, the coordinates have been optimized through a DFT relaxation, and the adsorption energies reported in a table in the same figure. From those values, the preferred adsorption sites for a single Si atom are bridge ones, in particular those laying on top of the Ag atoms from the first layer of the slab.

The dynamics of self-assembly itself has been finally investigated by the means of ab-initio molecular dynamics calculations, considering clusters of 6, 12 or 24 atoms of Si. The information about the adsorption of a single Si atom have been taken into account to construct the initial configuration of the system. Several simulation have been run to verify the length of the time step Δt and the temperature T of the system: for T >600 K several Si atoms desorb from the surface, hence at T =600 K $\sim$ 2 fs has been verified to be a good choice for Δt. For each cluster size, as shown in Fig. 6.15, the total energy and temperature have been extracted at the end of every self-consistent step, to

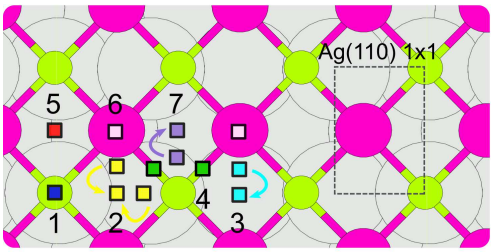

Ads. site	E_{ads} (eV)	ΔE (eV)
1	-1.54	0.59
2	-2.07	0.06
3	-2.10	0.03
4	-1.64	0.49
5	-1.98	0.15
6	-0.95	1.18
7	-2.13	--

Figure 6.14: Left panel: Sketch of NaCl/Ag(110) surface, the squares mark the investigated adsorption sites of a single Si atom; the colors highlight equivalent sites after optimization, while the numbers label the stable sites. The arrows point to the final position of the adatom after the optimization. On the background, the green/purple spheres show Cl/Na atoms and gray spheres show Ag atoms. Right panel: adsorption energies and energy difference for the stable configuration labeled in the left panel.

verify the absence of trends in both indicating the onset of numerical errors. At the step corresponding to the configuration with minimum energy, a snapshot has been extracted to visualize its geometry. From these plots it can be observed that the clusters evolve towards amorphous configurations, with no apparent symmetry. Therefore, it seems unlikely that the formation of isolated islands of Si atoms would be the correct model to address the regular structures observed through the experiments. It may be a good guess that such islands may act as nucleation centers allowing the formation of a thicker slab of silicon the surface of which is more regular. As the simulation of such evolution, within a first-principle formalism would require an important amount of computational resources, the identification of the reconstructed Si slab has been approached with a different method, which is dealt with in the next section.

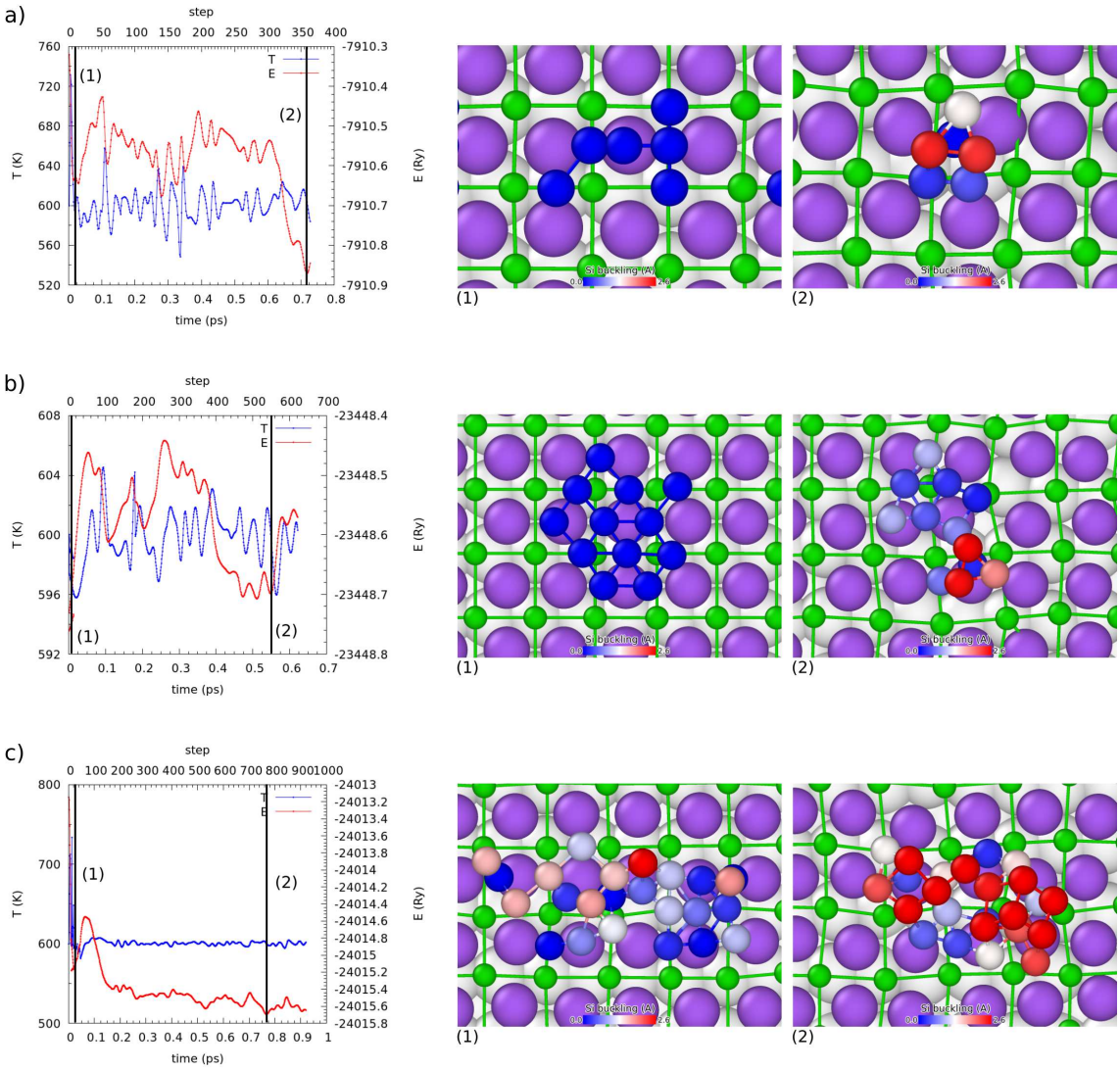

Figure 6.15: Molecular dynamics results for clusters of 6 (a), 12 (b) or 24 (c) Si atoms, adsorbed onto the NaCl/Ag(110) substrate. The left panels report the time evolution of temperature (T) and total energy (E) during the run; the straight lines on top of them mark the step at which the labeled snapshots have been taken. The right panels report the top view of the structures for the selected snapshots. The Si atoms are reported color-coded by their vertical position z: from red ($z=z_0$), through white to blue ($z=z_0+2.6$ Å). The Na/Cl atoms are shown as purple/green spheres. Ag atoms are shown as gray spheres, the darkness of which indicates the depth in the slab.

6.3.3 Converged random exploration of configuration space

Assuming a weak interaction of Si atoms with the NaCl film or the Ag surface, so that the only role of the layers of the substrate is to force the periodicity experimentally

measured, a way to target the reconstruction of Si atoms with the minimal energy is to consider an optimized random search of configurations. In particular the performance of the search is improved by considering the so-called genetic algorithm, in which the most stable coordinates are propagated step after step in order to converge the evolution of the geometries. Since the number of Si atoms to be included in the cell is not known, even that value has to be treated as a variable: in this way, it is possible to construct the 'energy-hull', i.e. the curve representing the energy of the most stable structure with respect to the number of Si atoms. Given the number of configurations to be taken into account, it is useful to consider the smallest supercell possible. In particular, focusing the attention on the LEED pattern reported in Fig. 6.1, it is useful to qualitatively investigate different periodicities. For example, if a silicene overlayer would have formed, its reciprocal space lattice should have appeared in the LEED pattern; moreover, given a 3×4 supercell, it is possible to construct a smaller supercell, in this case a 3/2×4/3 for which the aforementioned periodicity is the result of a coincidence pattern. Its appearance in the LEED could be the effect of the electron scattering contributions from the substrate, which would fold the spots into the first Brillouin zone of Ag(110). Therefore, the reciprocal vectors of the Ag(110), the NaCl film, the LB silicene, the 3×4 and the 3/2×4/3 lattices have been constructed and compared, as shown in Fig. 6.16, with and without the folding onto the Brillouin zone of the Ag(110) unit cell and with the experimental pattern. The silicene 1×1 lattice does not match any spot and can be ruled out; as expected from STM results, the additional spots observed in the experiments are best represented by those obtained from the 3×4 reconstruction. However, a non-uniform relaxation of a cell given by the coincidence pattern can still be the source of the observed periodicity, therefore such (3/2×4/3) supercell can still be regarded as a good candidate for the investigation through the approach with a genetic algorithm, in order to find trends that should apply for the larger supercell. Its structure has been constructed within the ASE module for python with an active region 1.0 Å thick into which the Si could be randomly inserted by the algorithm. The code starts constructing an initial pool of 40 such individuals, which are optimized through a DFT relaxation. Among those configurations, a population of 10 individuals, the ones called 'parents', is selected with the lowest energy (trying to avoid the replicas); from these, a pair of configurations is extracted and the coordinates of their atoms mixed, as mentioned in Sect. 2.5.2, to form a new structure. This process is repeated until 10 so-called 'children' have been generated; the probability of introducing a mutation, namely a random modification of the coordinates, is set to 0.9. These values have been chosen in order to try to guarantee enough variability, i.e. avoiding to get stuck in local minima,

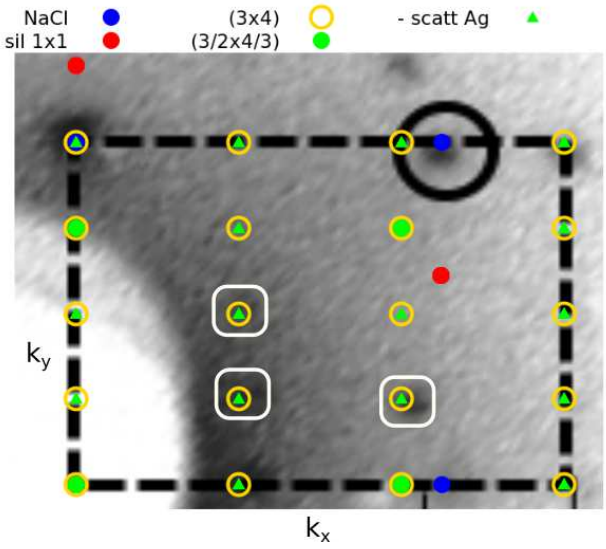

Figure 6.16: Simulated LEED pattern for different lattices and reconstructions, with and without the contribution of electron scattering from the substrate. The experimental pattern is reported in background for Si deposited on NaCl/Ag(110) from Fig. 6.1(c); the periodicity of the NaCl film is highlighted with a black circle. The pattern due to Ag(110) is reported by the dashed line. The white circles highlight the experimental spots marking the Si layer.

with a reasonable number of calculations. Once the energy hull has been constructed for such cell, the initial guesses for structures with $(3\times4)_{Ag}$ periodicity have been built either by random or by replicating the most stable geometries found in the (3/2×4/3) cell and starting the genetic algorithm again. Both the energy hulls plot are collected in Fig. 6.17. The energy trend is similar for both supercell sizes: the minimum can be found for 8 atoms in the (3/2×4/3) supercell; both configurations of the most stable structure are reported in Fig. 6.18. In the case of 6 atoms, the results for the larger cell do not include those for the smaller one. Since the initial population for such a configuration has been constructed through random collection of Si atoms, this result is an example of the dependency of the genetic algorithm from its numerical parameters. With 8 atoms, the formation of a thicker, although still regular, slab of silicon can be observed; with a larger cell the geometry is not amorphous but it is indeed less ordered. These results still indeed suggest that the substrate plays a role in stabilizing the structure of the overlayer and that a relaxation of such structure should yield important information about the validity of such an approach.

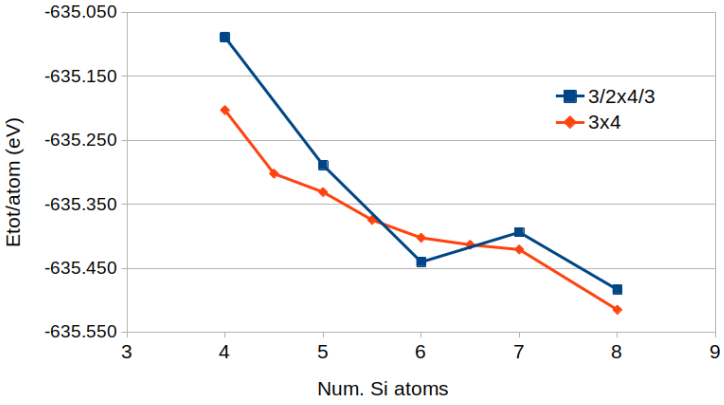

Figure 6.17: Energy of the most stable configuration obtained with the genetic algorithm as a function of the number of Si atoms in the supercell. The number of atoms is reported for the equivalent 3/2×4/3 supercell.

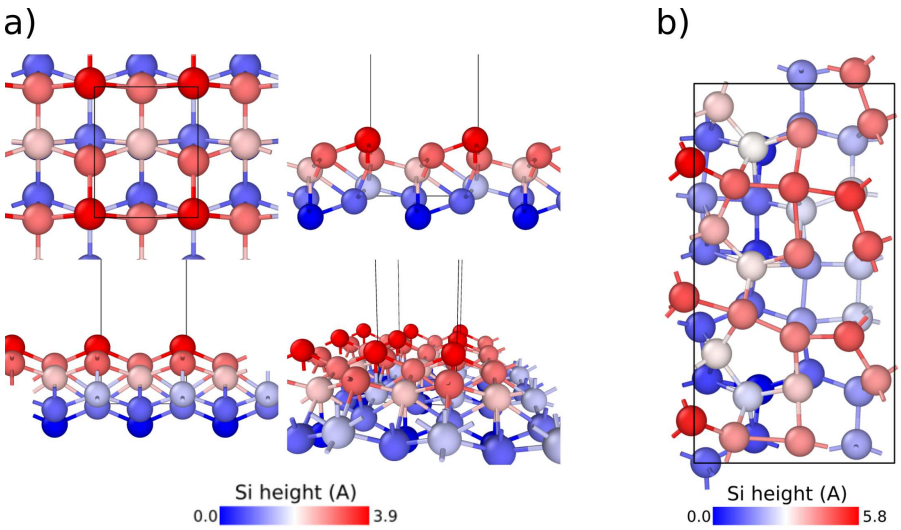

Figure 6.18: Structural models of the Si reconstructions for the most stable configurations, obtained with the genetic algorithm, for (a) 8 atoms in the 3/2×4/3 supercell and (b) 48 atoms in the 3×4 cell. In (a) different perspective of the cell are reported, in the clockwise direction there is top view, left view, perspective view and front view. In panel (b) the top view is shown. The supercell is reported as a black rectangle. The scale for the color code is reported at the bottom of each panel.

6.4 Conclusion

The reactivity of Si atoms deposited on the metallic Ag(110) surface has been investigated as a neutral film of NaCl is intercalated in between, with the hope of observing the

formation of a silicene layer. A complete experimental characterization, including STM, LEED, XPS and EXAFS results, has been studied in order to construct a model of the most probable reconstruction of the Si atoms. Since the data at hand was suggesting contrasting conclusions, the focus of this work shifted to investigate the self-assembly of Si atoms. Such study required through a multi-scale approach, in which several aspects of the interaction between Si atoms and the NaCl/Ag(110) substrate have been taken into account. Among those, the periodicity of the atomic structure or the dynamics of the aggregation have been compared with the experimental features to identify any pattern that could help identify the correct model for the system. In particular, the aggregation of Si atoms into clusters seems to foster the formation of a more regular layer, although not atomically thin. The application of an optimized search through random configuration, such as the one included in genetic algorithms, allowed the definition of a rationale for identifying good candidates for further optimization. Future developments of this work should include a verification and a refinement of the genetic algorithm through the inclusion of the effect of the substrate, which seems crucial in the stabilization of the Si layer in case of larger supercells.

Chapter 7

Conclusions

The research work described in this doctoral thesis has been dedicated to learn and exploit theoretical models suitable to investigate different materials and their interactions and to gather new insights on the physical processes happening at the nanoscale. Because of their technological relevance, the interfaces between a metallic surface coupled with materials, both organic and inorganic, have been modeled through both their ground and excited states.

In particular, their structural and electronic properties have been correlated with experimental measurements such as tunneling microscopy (STM), electron diffraction (LEED), x-ray absorption through (XPS, EXAFS, NEXAFS), optical absorption or reflection. From an atomistic perspective, such techniques often require to tackle with the properties of the excited states of the many-electrons system, for which it necessary to go beyond a ground state formalism. The common thread behind this work has been to address those physical properties arising from the limited dimensionality of a system, i.e. the presence of one or more surfaces, and to investigate the effect of the formation of the interface.

For an aromatic molecule, pentacene, adsorbed onto Pt(111), through experimental and simulated XPS and NEXAFS spectra it has been possible to verify the hybridization of molecular orbitals induced by the strong interaction regime.

In the case of an organic molecule with mixed sp^1/sp^2 hybridization C hybridization adsorbed on Au(111), the x-ray absorption has been investigated with respect to ideal sp^1 or sp^2 systems to identify the spectral fingerprint of carbon chains.

The two-dimensional honeycomb structure of Si, silicene, has been theoretically investigated both in free-standing and grown on Ag(111), as the surface is functionalized with the adsorption of single H or F atoms, at different coverages. The optical absorption and

reflection have been calculated and correlated with the modifications in the electronic properties, for which a dependency on the coverage of H/F adatoms can be observed. The functionalization has been shown to effectively tune the silicene properties; at the same time, the loss of the Dirac structure, characteristic of silicene, has been ascribed to the reactivity if Si atoms, which favor an sp^3 hybridization.

The deposition of Si atoms on the layered NaCl/Ag(110) substrate has been investigated with different approaches to search for a model of reconstruction which could fit experimental findings, which suggested the formation of a flat and homogeneous film. Several models of silicene, either with regular structures or with the inclusion of defects, have been constructed and compared with the Ag(110) lattice. The ones with best matching have been optimized, but they could not reproduce the reference periodicity nor the STM topography. Therefore the self-assembly of clusters of Si atoms has been investigated through ab-initio molecular dynamics calculations, for which it has been observed that Si atoms tend to aggregate as amorphous islands, suggesting the formation of a thicker layer that silicene. To verify such hypothesis, a random search through random configurations has been carried out, optimized through a genetic algorithm, for the periodicities of Si reconstructions identified from the experimental LEED pattern. The total energy of candidates for different number of Si atoms has been collected into the energy hull plot in order to identify the most promising structures to be further optimized in presence of the substrate. It has been observed that the most stable configurations have the same density of Si atoms; although their optimized structure is less ordered for larger reconstructions, suggesting the importance of stabilization effects of the substrate.

Finally, the various systems and phenomena investigated required to be tackled with different approaches and approximations, therefore this work indeed contributed to build a fundamental set of tools in my scientific background for future research activities.

Acknowledgments

I first want to thank Prof. Brivio for giving me such an opportunity to start a path on the journey of scientific research and to have kept me on that track. I also cannot be grateful enough to Guido Fratesi from Università degli Studi di Milano for having taught me not only the science, but the perspective of the scientist, too. I wish to thank Prof. Kara from University of Central Florida, Orlando (US) for the opportunity of getting to know the life in the Unites States and for showing me that there is always something to learn, sometimes even when you don't expect to. As the scientist that I like thinking myself to be, I cannot but be aware of the undeniable correlation I have with my partner Stefania and her never ending strength, even when she thinks otherwise. Many other people have contributed to get me where I am now, just to name a few my group mates Anu Baby and Abhilash Ravikumar (former! but I still miss our spicy lunches), my friends old and new, thanks you all. Last but not least, I deeply thank my parents: only as the times passes by, I can properly understand how much I am indebted to them.

Bibliography

[1] Graham Kendall. Would your mobile phone be powerful enough to get you to the moon?

[2] Hans Lüth. *Solid surfaces, interfaces and thin films.* Springer, 2010.

[3] University of Oxford. Department of chemistry - rauschenbach research.

[4] J. Tersoff and D.R. Hamann. Theory of the scanning tunneling microscope. *Phys. Rev. B*, (31):805, 1985.

[5] M.A. Van Hove, W.H Weinberg, and C.-M. Chan. *Low Energy Electron Diffraction.* Springer-Verlag Berlin Heidelberg, 1986.

[6] Charles Kittel. *Introduction to Solid State Physics.* Wiley, 2004.

[7] M. P. Seah and W. A. Dench. Quantitative electron spectroscopy of surfaces: A standard data base for electron inelastic mean free paths in solids. *Surface and Interface Analysis*, 1(1):2–11, 1979.

[8] M.-C. Desjonqueres and D. Spanjaard. *Concepts in Surface Physics.* Springer-Verlag Berlin Heidelberg, 1996.

[9] J.J. Rehr and R.C. Albers. Theoretical approaches to x-ray absorption fine structure. *Rev. Mod. Phys.*, (72):621, 2000.

[10] L.D. Landau and E.M. Lifshits. Quantum mechanics: non-relativistic theory, 1965.

[11] R.G. Parr and W. Yang. Density functional theory of atoms and molecules. *Oxford University press*, 1989.

[12] J.W. Negele and H. Orland. Quantum many-particle systems. 1998.

[13] A.L. Fetter and J.D. Walecka. *Quantum theory of Many-Body systems.* McGraw-Hill, 1971.

[14] P. Hohenberg and W. Kohn. Inhomogeneous electron gas. *Phys. Rev.*, (136(3B)):864, 1964.

[15] W. Kohn and L.J. Sham. Self-consistent equations including exchange and correlation effects. *Phys. Rev.*, (140(4A)):A1133–A1138, 1965.

[16] J.P. Perdew and Y. Wang. Accurate and simple analytic representation of the electron-gas correlation energy. *Phys. Rev. B*, (45):13244, 1992.

[17] J.P. Perdew, K. Burke, and M. Ernzerhof. Generalized gradient approximation made simple. *Phys. Rev. Lett.*, (77):3865, 1996.

[18] J Klimeš and Angelos Michaelides. Perspective: Advances and challenges in treating van der Waals dispersion forces in density functional theory. *Journal of Chemical Physics*, 137(12):120901, 2012.

[19] E. Zaremba and W. Kohn. Van der Waals interaction between an atom and a solid surface. *Phys. Rev. B*, 13(6):2270–2285, 1976.

[20] J. F. Dobson, B. P. Dinte, and J. Wang. Electronic density functional theory. *Springer Science+Business Media*, 1998.

[21] S. Grimme. Semiempirical gga-type density functional constructed with a long-range dispersion correction. *J. Comput. Chem.*, 27:1787–1799, 2006.

[22] S. Grimme, J. Antony, S. Ehrlich, and S. Krieg. A consistent and accurate *ab initio* parametrization of density functional dispersion correction (dft-d) for the 94 elements h-pu. *J. Chem. Phys.*, (132):154104, 2010.

[23] S. Grimme, S. Ehrlich, and L. Goerigk. Effect of the damping function in dispersion corrected density functional theory. *J. Comp. Chem.*, (32):1456, 2011.

[24] A. Tkatchenko and M. Scheffler. Accurate molecular van der waals interactions from ground-state electron density and free-atom reference data. *Phys. Rev. Lett.*, (102):073005, 2009.

[25] Langreth D.C., M. Dion, H. Rydberg, E. Schröder, P. Hyldgaard, and B.I. Lundqvist. Van der waals density functional theory with applications. *International Journal of Quantum Chemistry*, (101):599, 2005.

[26] M. Dion, H. Rydberg, E. Schröder, D.C. Langreth, and B.I. Lundqvist. Van der waals density functional for general geometries. *Phys. Rev. Lett.*, (92):246401, 2004.

[27] Kurt Lejaeghere, Gustav Bihlmayer, Peter Blaha, Stefan Bl, Volker Blum, Damien Caliste, Ivano E Castelli, Stewart J Clark, Andrea Dal Corso, Stefano De Gironcoli, John Kay Dewhurst, Igor Di Marco, Claudia Draxl, Marcin Dułak, Olle Eriksson, Kevin F Garrity, Luigi Genovese, Paolo Giannozzi, Matteo Giantomassi, Stefan Goedecker, Xavier Gonze, Oscar Gr, D R Hamann, Phil J Hasnip, N A W Holzwarth, Diana Ius, Dominik B Jochym, Daniel Jones, Georg Kresse, Klaus Koepernik, K Emine, Inka L M Locht, Sven Lubeck, Martijn Marsman, Nicola Marzari, Ulrike Nitzsche, Lars Nordstr, Taisuke Ozaki, Lorenzo Paulatto, Chris J Pickard, Ward Poelmans, and I J Matt. Reproducibility in density-functional theory calculations of solids. *Science*, 351(6280):aad3000, 2016.

[28] J. Kohanoff. Electronic structure calculations for solids and molecules: theory and computational methods. *Cambridge University press*, 2006.

[29] R. M. Martin. Electronic structure. basic theory and practical methods. *Cambridge University press*, 2004.

[30] D. Hamann, M. Schlüter, and C. Chiang. Norm-Conserving Pseudopotentials. *Phys. Rev. Lett.*, 43(20):1494–1497, 1979.

[31] David Vanderbilt. Soft self-consistent pseudopotentials in a generalized eigenvalue formalism. *Phys. Rev. B*, 41(11):7892–7895, 1990.

[32] P.E. Blöchl. Projector augmented waves. *Phys. Rev. B*, 50(24):17953, 1994.

[33] G. Kresse and D. Joubert. From ultrasoft pseudopotentials to the projector augmented-wave method. *Phys. Rev. B*, 59(3):1758, 1999.

[34] P. Giannozzi, S. Baroni, N. Bonini, M. Calandra, R. Car, C. Cavazzoni, D. Ceresoli, G. L. Chiarotti, M. Cococcioni, I. Dabo, A. D. Corso, S. de Gironcoli, S. Fabris, G. Fratesi, R. Gebauer, and et al. Quantum espresso: A modular and open-source software project for quantum simulations of materials. *J. Phys.: Condens. Matter*, (21):395502, 2009.

[35] P. Giannozzi and et. al. *J.Phys.:Condens.Matter*, (29):465901, 2017.

[36] G. Kresse and J. Hafner. *Phys. Rev. B*, (48):558, 1993.

[37] G. Kresse and J. Hafner. *Phys. Rev. B*, (14):251, 1994.

[38] G. Kresse and J. Furthmüller. *Comput. Mat. Sci.*, (6):15, 1996.

[39] G. Kresse and J. Furthmüller. *Phys. Rev. B*, 11(54):169, 1996.

[40] H.J. Monkhorst and J.D. Pack. Special points for brillouin zone integrations. *Phys. Rev. B: Condens. Matter Mater. Phys.*, 13:5188–5192, 1976.

[41] J.F. Janak. Proof that $\partial E/\partial n = \varepsilon$ in density functional theory. *Phys. Rev. B*, (18):7165, 1978.

[42] S. García-Gil, A. García, and P. Ordejón. Calculation of core level shifts within dft using pseudopotentials and localized basis sets. *Eur. Phys. J. B*, (85):239, 2012.

[43] L. Triguero, G.M. Pettersson, and H. Ågren. Calculations of near-edge x-ray-absorption spectra of gas-phase and chemisorbed molecules by means of density-functional and transition-potential theory. *Phys. Rev. B*, 58(12):8097, 1998.

[44] C. Gougoussis, M. Calandra, A.P. Seitsonen, and F. Mauri. First-principles calculations of x-ray absorption in a scheme based on ultrasoft pseudopotentials: From α-quartz to high-t_c compounds. *Phys. Rev. B*, 80:075102, 2009.

[45] M. Taillefumier, D. Cabaret, A.M. Flank, and F. Mauri. X-ray absorption near-edge structure calculations with the pseudopotentials: Application to the k edge in diamond and α-quartz. *Phys. Rev. B*, 66:195707, 2002.

[46] C. Lanczos. *J. Res. Natl. Bur. Stand.*, 45:255, 1950.

[47] C. Lanczos. *J. Res. Natl. Bur. Stand.*, 49:33, 1952.

[48] R. Haydock, V. Heine, and M.J. Kelly. *J. Phys. C*, 5:2845, 1972.

[49] R. Haydock, V. Heine, and M.J. Kelly. *J. Phys. C*, 8:2591, 1975.

[50] J.D. Jackson. *Classical electrodynamics*. Wiley, 1999.

[51] J.I. Pankove. *Optical processes in semiconductors*. Courier corporation, 1975.

[52] P.Y. Yu and M. Cadorna. *Fundamentals of Semiconductors*. Springer, 2010.

[53] R. Del Sole and R. Girlanda. Optical properties of semiconductors within the independent-quasiparticle approximation. *Phys. Rev. B*, 48(16):11789, 1993.

[54] G. Onida, L. Reining, and A. Rubio. Electronic excitations: density-functional versus many-body green's-function approaches. *Rev. Mod. Phys.*, 74:601, 2002.

[55] Bassani and Pastori-Parravicini. *Electronic states and optical transitions in solids*. Pergamon Press NY, 1975.

[56] F. Bechstedt, L. Matthes, P. Gori, and O. Pulci. *Appl. Phys. Lett.*, 100:261906, 2012.

[57] J.D.E. McIntyre and D.E. Aspnes. Differential reflection spectroscopy of very thin surface films. *Surf. Sci.*, 24:417, 1971.

[58] R.J. Cole, B.G. Frederick, and P. Weightman. Substrate dependence of adlayer optical response in reflectance anisotropy spectroscopy. *J. Vac. Sci. & Technol. A*, 16:3088, 1998.

[59] D. Mark and J. Hutter. *Ab-initio molecular dynamics: basic theory and advanced methods*. Cambridge University Press, 2009.

[60] A.R. Oganov and C.W. Glass. Crystal structure prediction using ab initio evolutionary techniques: Principles and applications. *J. Chem. Phys.*, 124:244704, 2006.

[61] D.M. Deaven and K.M. Ho. Molecular geometry optimization with a genetic algorithm. *Phys. Rev. Lett.*, 75(2):288, 1995.

[62] T.S. Bush, C.R.A. Catlow, and P.D. Battle. Evolutionary programming techniques for predicting inorganic crystal structures. *J. Mater. Chem.*, 5:1269, 1995.

[63] R.L. Johnston. Evolving better nanoparticles: Genetic algorithms for optimising cluster geometries. *Dalton Trans.*, page 4193, 2003.

[64] M. Griebel, S. Knapek, and G. Zumbusch. *Numerical simulation in Molecular Dynamics*. Springer, 2007.

[65] L.B. Vilhelmsen and B. Hammer. Systematic study of au6 to au12 gold clusters on mgo(100) f centers using density-functional theory. *Phys. Rev. Lett.*, 108:126101, 2012.

[66] L.B. Vilhelmsen and B. Hammer. A genetic algorithm for first principles global optimization of supported nano structures. *J. Chem. Phys.*, 141:044711, 2014.

[67] M. Van den Bossche, H. Grönbeck, and B. Hammer. Tight-binding approximation-enhanced global optimization. *J. Chem. Theory Comput.*, 14:2797, 2018.

[68] Ask Hjorth Larsen, Jens Jørgen Mortensen, Jakob Blomqvist, Ivano E Castelli, Rune Christensen, Marcin Dułak, Jesper Friis, Michael N Groves, Bjørk Hammer, Cory Hargus, Eric D Hermes, Paul C Jennings, Peter Bjerre Jensen, James Kermode, John R Kitchin, Esben Leonhard Kolsbjerg, Joseph Kubal, Kristen Kaasbjerg, Steen Lysgaard, Jón Bergmann Maronsson, Tristan Maxson, Thomas Olsen, Lars Pastewka, Andrew Peterson, Carsten Rostgaard, Jakob Schiøtz, Ole Schütt, Mikkel Strange, Kristian S Thygesen, Tejs Vegge, Lasse Vilhelmsen, Michael Walter, Zhenhua Zeng, and Karsten W Jacobsen. The atomic simulation environment—a python library for working with atoms. *Journal of Physics: Condensed Matter*, 29(27):273002, 2017.

[69] G. Trimarchi and A. Zunger. Global space-group optimization problem: Finding the stablest crystal structure without constraints. *Phys. Rev. B*, 75:104113, 2007.

[70] L. Kronik and N. Koch. Electronic properties of organic-based interfaces. *MRS Bull.*, 35:417–422, 2010.

[71] J. E. Anthony. Functionalized acenes and heteroacenes for organic electronics. *Chem. Rev.*, 106:5028–5048, 2006.

[72] N. Koch. Organic electronic devices and their functional interfaces. *Chem. Phys. Chem.*, 8:1438, 2007.

[73] J. Hwang, A. Wan, and A. Kahn. Energetics of metal-organic interfaces: New experiments and assessment of the field. *Mater. Sci. Eng. R*, 64:1–31, 2009.

[74] I. Kymissis and 2009. . *Organic Field Effect Transistors: Theory, Fabrication and Characterization*. Springer U.S., 2009.

[75] N. Koch. Energy levels at interfaces between metals and conjugated organic molecules. *J. Phys.: Condens. Matter*, 20:184008, 2008.

[76] I. Nausieda, K. K. Ryu, D. D. He, A. I. Akinwande, V. Bulovic, and C. G. Sodini. Dual threshold voltage organic thin-film transistor technology. *IEEE Trans. Electron Devices*, 57:3027–3032, 2010.

[77] N. V. Tsamados, D. ans Cvetkovic, K. Sidler, J. Bhandari, V. Savu, J. Brugger, and A. M. Ionescu. Double-gate pentacene thin-film transistor with improved control in sub-threshold region. *Solid-State Electron*, 54:1003–1009, 2010.

[78] R. Zhang, A. J. Hensley, J.-S. McEwen, S. Wickert, E. Darlatt, K. Fischer, M. Schöppke, R. Denecke, R. Streber, M. Lorenz, and et al. Integrated x-ray photoelectron spectroscopy and dft character- ization of benzene adsorption on pt(111), pt(355) and pt(322) surfaces. *Phys. Chem. Chem. Phys.*, 15:20662–20671, 2013.

[79] P. Ayishabi, K. Lakshmikanth, and R. Chatanathodi. Chemisorption of benzene on pt (111) surface: A dft study with van der waals interaction. *Chem. Phys. Lett.*, 637:182–188, 2015.

[80] W. Liu, V. G. Ruiz, G. X. Zhang, B. Santra, X. Ren, M. Scheffler, and A. Tkatchenko. Structure and energetics of benzene adsorbed on transition-metal surfaces: Density-functional theory with van der waals interactions including collective substrate response. *New J. Phys.*, 15:053046, 2013.

[81] H. Yildirim, T. Greber, and A. Kara. Trends in adsorption characteristics of benzene on transition metal surfaces: Role of surface chemistry and van der waals interactions. *J. Phys. Chem. C*, 117:20572–20583, 2013.

[82] H. Ihm, H. M. Ajo, J. M. Gottfried, P. Bera, and C. T. Campbell. Calorimetric measurement of the heat of adsorption of benzene on pt(111). *J. Phys. Chem. B*, 108:14627–14633, 2004.

[83] L. Floreano, A. Cossaro, D. Cvetko, G. Bavdek, and A. Morgante. Phase diagram of pentacene growth on au(110). *J. Phys. Chem. B*, 110:4908–4913, 2006.

[84] K. Muller, A. P. Seitsonen, T. Brugger, J. Westover, T. Greber, T. Jung, and A. Kara. Electronic structure of an organic/metal interface: Pentacene/cu(110). *J. Phys. Chem. C*, 116:23465–23471, 2012.

[85] D. Käfer and G. Witte. Evolution of pentacene films on ag(111): Growth beyond the first monolayer. *Chem. Phys. Lett.*, 442:376–383, 2007.

[86] A. Baby, H. Lin, G. P. Brivio, L. Floreano, and G. Fratesi. Core-level spectra and molecular deformation in adsorption: V-shaped pentacene on al (001). *Beilstein J. Nanotechnol.*, 6:2242–2251, 2015.

[87] J. H. Kang and X. Y. Zhu. Layer-by-layer growth of incommensurate, polycrystalline, lying-down pentacene thin films on au(111). *Chem. Mater.*, 18:1318–1323, 2006.

[88] C. B. France, P. G. Schroeder, and B. A. Parkinson. Direct observation of a widely spaced periodic row structure at the pentacene/au(111) interface using scanning tunneling microscopy. *Nano Lett.*, 2:693–696, 2002.

[89] L. Casalis, M. Danisman, B. Nickel, G. Bracco, T. Toccoli, S. Iannotta, and G. Scoles. Hyperthermal molecular beam deposition of highly ordered organic thin films. *Phys. Rev. Lett.*, 90:206101, 2003.

[90] Y. Wang, W. Ji, D. Shi, S. Du, C. Seidel, Y. Ma, H.-J. Gao, L. Chi, and H. Fuchs. Structural evolution of pentacene on a ag(110) surface. *Phys. Rev. B: Condens. Matter Mater. Phys.*, 69:075408, 2004.

[91] G. Bavdek, A. Cossaro, D. Cvetko, C. Africh, C. Blasetti, F. Esch, A. Morgante, L. Floreano, and et al. Pentacene nanorails on au (110). *Langmuir*, 24:767–772, 2008.

[92] M. Sauvage-Simkin, A. Coati, Y. Garreau, A. Vlad, K. Müller, A. Bendounan, and A. Kara. In-depth atomic structure of the pentacene/cu(110) interface in the monolayer coverage regime: Theory and x-ray diffraction results. *J. Phys. Chem. C*, 118:27815–27822, 2014.

[93] A. Ferretti, C. Baldacchini, A. Calzolari, R. Di Felice, A. Ruini, E. Molinari, and M. G. Betti. Mixing of electronic states in pentacene adsorption on copper. *Phys. Rev. Lett.*, 99:046802, 2007.

[94] X. Q. Shi, Y. Li, M. A. Van Hove, and R. Q. Zhang. Interactions between organics and metal surfaces in the intermediate regime between physisorption and chemisorption. *J. Phys. Chem. C*, 116:23603–23607, 2012.

[95] A. Baby, G. Fratesi, S. R. Vaidya, L. L. Patera, L. Africh, C. andFloreano, and G. P. Brivio. Anchoring and bending of pentacene on aluminum (001). *J. Phys. Chem. C*, 119:3624–3633, 2015.

[96] A. Ugolotti. Ab initio investigation of the adsorption of aromatic molecules on a platinum surface. Master's thesis, Università degli Studi di Milano-Bicocca, Milan, Italy, 2016.

[97] L. Bengtsson. Dipole correction for surface supercell calculations. *Phys. Rev. B: Condens. Matter Mater. Phys.*, 59:12301–12304, 1999.

[98] R. W. G. Wyckoff. *Crystal structures.* John Wiley, NY, 1963.

[99] A. Ugolotti, S.S. Harivyasi, A. Baby, M. Dominguez, A.L. Pinardi, M.F. López, J.A. Martín-Gago, G. Fratesi, L. Floreano, and G.P. Brivio. Chemisorption of pentacene on pt(111) with a little molecular distortion. *J. Phys. Chem. C*, 121:22797–22–805, 2017.

[100] V. G. Ruiz, W. Liu, E. Zojer, M. Scheffler, and A. Tkatchenko. Density-functional theory with screened van der waals interactions for the modeling of hybrid inorganic-organic systems. *Phys. Rev. Lett.*, 108:2–6, 2012.

[101] G. Kresse and J. Furthmüller. Efficient iterative schemes for ab-initio total-energy calculations using a plane-wave basis set. *Phys. Rev. B: Condens. Matter Mater. Phys.*, 54:11169–11186, 1996.

[102] P.-O. Löwdin. On the nonorthogonality problem. *Adv. Quantum Chem.*, 5:185–199, 1970.

[103] T. A. Land, T. Michely, R. J. Behm, J. C. Hemminger, and G. Comsa. Direct observation of surface reactions by scanning tunneling microscopy: Ethylene → ethylidyne → carbon particles → graphite on pt(111). *J. Chem. Phys.*, 97:6774–6783, 1992.

[104] L. Floreano, A. Cossaro, R. Gotter, A. Verdini, G. Bavdek, F. Evangelista, A. Ruocco, A. Morgante, and D. Cvetko. Periodic arrays of cu-phthalocyanine chains on au (110). *J. Phys. Chem. C*, 112:10794–10802, 2008.

[105] M. Leetmaa, M. P. Ljungberg, A. Lyubartsev, A. Nilsson, and L. G. M. Pettersson. Theoretical approximations to x-ray absorption spectroscopy of liquid water and ice. *J. Electron Spectrosc. Relat. Phenom.*, 177:135–157, 2010.

[106] O. McDonald, A. A. Cafolla, Z. Li, and G. Hughes. Synchrotron photoemission studies of pentacene films on cu(110). *Surf. Sci.*, 600:1909–1916, 2006.

[107] C. Baldacchini, F. Allegretti, R. Gunnella, and M. G. Betti. Molecule-metal interaction of pentacene on copper vicinal surfaces. *Surf. Sci.*, 601:2603–2606, 2007.

[108] Z. Zhou and R. Parr. *J. Am. Chem. Soc.*, pages 7371–7379, 1989.

[109] P. Geerlings, F. De Proft, and W. Langenaeker. *Chem. Rev.*, 103:1793, 2003.

[110] R. Toyoshima, M. Yoshida, Y. Monya, K. Suzuki, K. Amemiya, K. Mase, B. S. Mun, and H. Kondoh. A high-pressure-induced dense co overlayer on a pt(111)

surface: a chemical analysis using in-situ near ambient pressure xps. *Phys. Chem. Chem. Phys.*, 16:23564–23567, 2014.

[111] M. Alagia, C. Baldacchini, M. G. Betti, F. Bussolotti, V. Carravetta, U. Ekström, C. Mariani, and S. Stranges. Core-shell photoabsorption and photoelectron spectra of gas-phase pentacene: Experiment and theory. *J. Chem. Phys.*, 122:124305, 2005.

[112] G. Fratesi, V. Lanzilotto, L. Floreano, and G. P. Brivio. Azimuthal dichroism in near-edge x-ray absorption fine structure spectra of planar molecules. *J. Phys. Chem. C*, 117:6632–6638, 2013.

[113] G. Fratesi, S. Achilli, N. Manini, G. Onida, A. Baby, A. Ravikumar, A. Ugolotti, G. Brivio, A. Milani, and C. Casari. Fingerprints of sp1 hybridized c in the near-edge x-ray absorption spectra of surface-grown materials. *Materials*, 11(12):2556, 2018.

[114] Andreas Hirsch. The era of Carbon allotropes. *Nat. Mater.*, 9(11):868–871, NOV 2010.

[115] I. E. Castelli, P. Salvestrini, and N. Manini. Mechanical properties of carbynes investigated by ab-initio total-energy calculations. *Phys. Rev. B.*, 85:214110, 2012.

[116] R. Hoffmann, A. A. Kabanov, A. A. Golov, and D. M. Proserpio. Homo citans and carbon allotropes: For an ethics of citation. *Angew. Chem. Int. Ed.*, 55:10962, 2016.

[117] L.A. Burchfield, M. Al Fahim, R.S. Wittman, F. Delodovici, and N. Manini. Novamene: a new class of carbon allotropes. *Heliyon*, 3:e00242, 2017.

[118] F. Delodovici, N. Manini, R.S. Wittman, D.S. Choi, M. Al Fahim, and L.A. Burchfield. Protomene: a new carbon allotrope. *Carbon*, 126:574, 2018.

[119] C. S. Casari, M. Tommasini, R. R. Tykwinski, and A. Milani. Carbon-atom wires: 1-D systems with tunable properties. *Nanoscale*, 8(8):4414–4435, 2016.

[120] F. Cataldo, editor. *Polyynes: Synthesis, Properties, and Applications.* CRC, Taylor&Francis, London, 2005.

[121] C. S. Casari and A. Milani. Carbyne: from the elusive allotrope to stable Carbon atom wires. *MRS Commun.*, 8(2):207–219, JUN 2018.

[122] Florian Banhart. Chains of Carbon atoms: A vision or a new nanomaterial? *Beilstein J. Nanotech.*, 6:559–569, FEB 25 2015.

[123] Wesley A. Chalifoux and Rik R. Tykwinski. Synthesis of polyynes to model the sp-Carbon allotrope carbyne. *Nat. Chem.*, 2(11):967–971, NOV 2010.

[124] Lei Shi, Philip Rohringer, Kazu Suenaga, Yoshiko Niimi, Jani Kotakoski, Jannik C. Meyer, Herwig Peterlik, Marius Wanko, Seymur Cahangirov, Angel Rubio, Zachary J. Lapin, Lukas Novotny, Paola Ayala, and Thomas Pichler. Confined linear Carbon chains as a route to bulk carbyne. *Nat. Mater.*, 15(6):634+, JUN 2016.

[125] Levon D. Movsisyan, Dmitry V. Kondratuk, Michael Franz, Amber L. Thompson, Rik R. Tykwinski, and Harry L. Anderson. Synthesis of Polyyne Rotaxanes. *Org. Lett.*, 14(13):3424–3426, JUL 6 2012.

[126] Levon D. Movsisyan, Michael Franz, Frank Hampel, Amber L. Thompson, Rik R. Tykwinski, and Harry L. Anderson. Polyyne Rotaxanes: Stabilization by Encapsulation. *J. Am. Chem. Soc.*, 138(4):1366–1376, FEB 3 2016.

[127] Michael Franz, Johanna A. Januszewski, Dominik Wendinger, Christian Neiss, Levon D. Movsisyan, Frank Hampel, Harry L. Anderson, Andreas Goerling, and Rik R. Tykwinski. Cumulene Rotaxanes: Stabilization and Study of [9]Cumulenes. *Angew. Chem. Int. Edit.*, 54(22):6645–6649, MAY 26 2015.

[128] Nancy Weisbach, Zuzana Baranova, Sebastien Gauthier, Joseph H. Reibenspies, and John A. Gladysz. A new type of insulated molecular wire: a rotaxane derived from a metal-capped conjugated tetrayne. *Chem. Commun.*, 48(61):7562–7564, 2012.

[129] Stephen Schrettl, Emmanuel Contal, Tobias N. Hoheisel, Martin Fritzsche, Sandor Balog, Ruth Szilluweit, and Holger Frauenrath. Facile synthesis of oligoyne amphiphiles and their rotaxanes. *Chem. Sci.*, 6(1):564–574, 2015.

[130] Qiang Sun, Liangliang Cai, Honghong Ma, Chunxue Yuan, and Wei Xu. Dehalogenative Homocoupling of Terminal Alkynyl Bromides on Au(111): Incorporation of Acetylenic Scaffolding into Surface Nanostructures. *ACS Nano*, 10(7):7023–7030, JUL 2016.

[131] Qiang Sun, Bay V. Tran, Liangliang Cai, Honghong Ma, Xin Yu, Chunxue Yuan, Meike Stohr, and Wei Xu. On-Surface Formation of Cumulene by Dehalogenative

Homocoupling of Alkenyl gem-Dibromides. *Angw. Chem. Int. Ed.*, 56(40):12165–12169, SEP 25 2017.

[132] Chen-Hui Shu, Meng-Xi Liu, Ze-Qi Zha, Jin-Liang Pan, Shao-Ze Zhang, Yu-Li Xie, Jian-Le Chen, Ding-Wang Yuan, Xiao-Hui Qiu, and Pei-Nian Liu. On-surface synthesis of poly(p-phenylene ethynylene) molecular wires via in situ formation of Carbon-Carbon triple bond. *Nat. Commun.*, 9, JUN 13 2018.

[133] P.R. Wallace. The band theory of graphite. *Phys. Rev.*, 71:622, 1947.

[134] J.C. Slonczewski and P.R. Weiss. Band structure of graphite. *Phys. Rev.*, 109:272, 1958.

[135] K. S. Novoselov, A. K. Geim, S. V. Morozov, D. Jiang, Y. Zhang, S. V. Dubonos, I. V. Grigorieva, and A. A. Firsov. Electric field effect in atomically thin carbon films. *Science*, 306:666, 2001.

[136] K. S. Novoselov, A. K. Geim, S. V. Morozov, D. Jiang, M. I. Katsnelson, I. V. Grigorieva, S. V. Dubonos, and A. A. Firsov. Two-dimensional gas of massless dirac fermions in graphene. *Nature*, 438:197, 2005.

[137] Y. Zhang, Y.-W. Tan, H. L. Stormer, and P. Kim. Experimental observation of the quantum hall effect and berry's phase in graphene. *Nature*, 438:201, 2005.

[138] R. R. Nair1, P. Blake, A. N. Grigorenko, K. S. Novoselov, T. J. Booth, T. Stauber, N. M. R. Peres, and A. K. Geim. Fine structure constant defines visual transparency of graphene. *Science*, 320:1308, 2008.

[139] A. Molle and et al. Buckled two-dimensional xene sheets. *Nature Materials*, 26:163–169, 2017.

[140] S. Cahangirov, M. Topsakal, E. Aktürk, H. Şahin, and S. Ciraci. Two- and one-dimensional honeycomb structures of silicon and germanium. *Phys. Rev. Lett.*, 102:236804, 2009.

[141] R Qin, C.-H. Wang, W Zhu, and Y Zhang. First-principles calculations of mechanical and electronic properties of silicene under strain. *AIP Adv.*, 2:022159, 2012.

[142] Z.-G Shao, X.-S Ye, L Lei Yang, and C.-L Wang. First-principles calculation of intrinsic carrier mobility of silicene. *J. Appl. Phys.*, 114:093712, 2013.

[143] L. Matthes, O. Pulci, and F. Bechstedt. Optical properties of two-dimensional honeycomb crystals graphene, silicene, germanene, and thiene from first principles. *New Journal of Physics*, 16:105007, 2014.

[144] L. Matthes, P. Gori, O. Pulci, and F. Bechstedt. Universal infrared absorbance of two-dimensional honeycomb group-iv crystals. *Phys. Rev. B*, 87:035438, 2013.

[145] W. Wei and T. Jacob. Strong many-body effects in silicene-based structures. *Phys. Rev. B*, 88:045203, 2013.

[146] M Ezawa. A topological insulator and helical zero mode in silicene under an inhomogeneous electric field. *New J. of Phys.*, 14:033003, 2012.

[147] M Ezawa. Valley-polarized metals and quantum anomalous hall effect in silicene. *Phys. Rev. Lett.*, 109:055502, 2012.

[148] B Lalmi and et al. Epitaxial growth of a silicene sheet. *Appl. Phys. Lett.*, 97:223109, 2010.

[149] P Vogt, P De Padova, C Quaresima, J Avila, E Frantzeskakis, M C Asensio, A Resta, B Ealet, and G Le Lay. Silicene: Compelling experimental evidence for graphenelike two-dimensional silicon. *Phys. Rev. Lett.*, 108:155501, 2012.

[150] C.-L Lin, R Arafune, K Kawahara, N Tsukahara, E Minamitani, Y Kim, N Takagi, and M Kawai. Structure of silicene grown on ag(111). *Appl. Phys. Expr.*, 5:045802, 2012.

[151] E Cinquanta, E Scalise, D Chiappe, C Grazianetti, B van den Broek, M Houssa, M Fanciulli, and A Molle. Getting through the nature of silicene: An sp^2-sp^3 two-dimensional silicon nanosheet. *J. Phys. Chem. C*, 117:16719–16724, 2013.

[152] A Molle, C Grazianetti, D Chiappe, E Cinquanta, E Cianci, G Tallarida, and M Fanciulli. Hindering the oxidation of silicene with non-reactive encapsulation. *Adv. Funct. Mater.*, 23:4340–4344, 2013.

[153] M. Satta, S. Colonna, R. Flammini, A. Cricenti, and F. Ronci. Silicon reactivity at the ag(111) surface. *Phys. Rev. Lett.*, 115:026102, 2015.

[154] E. Cinquanta and et al. Optical response and ultrafast carrier dynamics of silicene-silver interface. *Phys. Rev. B*, 92:165427, 2015.

[155] C. Hogan and et al. Optical properties of silicene, si/ag(111), and si/ag(110). *Phys. Rev. B*, 97:195407, 2018.

[156] H. Houssa, E. Scalise, K. Sankaran, G. Pourtois, V. V. Afans'ev, and A. Stesmans. Electronic properties of hydrogenated silicene and germanene. *Appl. Phys. Lett.*, 98:223107, 2011.

[157] Y. Ding and Y. Wang. Electronic structures of silicene fluoride and hydride. *Appl. Phys. Lett.*, 100:083102, 2012.

[158] P Zhang, X D Li, C H Hu, S Q Wu, and Zhu Z Z. First-principles studies of the hydrogenation effects in silicene sheets. *Phys. Lett. A*, 376:1230–1233, 2012.

[159] F. Zheng and C. Zhang. The electronic and magnetic properties of functionalized silicene: a first-principles study. *Nanoscale Research Letters*, 7:422, 2012.

[160] X. Wang, H. Liu, and S. Tu. First-principles study of half-fluorinated silicene sheets. *RCS Adv.*, 5:6238, 2015.

[161] M. Pizzochero, M. Bonfanti, and R. Martinazzo. Hydrogen on silicene: like or unlike graphene? *Phys. Chem. Chem. Phys.*, 18:15654–15666, 2016.

[162] R. B. Pontes, R. R. Mançano, R. da Silva, L. F. Cótica, R. H. Miwa, and Padilha J. E. Electronic and optical properties of hydrogenated group-iv multilayer materials. *Phys. Chem. Chem. Phys.*, 20:8112, 2018.

[163] J. Qiu, H. Fu, Y. Xu, A. I. Oreshkin, T. Shao, H. Li, S. Meng, L. Chen, and K. Wu. Ordered and reversible hydrogenation of silicene. *Phys. Rev. Lett.*, 114:126101, 2015.

[164] J. Qiu, Y. Fu, Y. Xu, Q. Zhou, S. Meng, H. Li, L. Chen, and K. Wu. From silicene to half-silicane by hydrogenation. *ACS Nano*, 9:11192–11199, 2015.

[165] W. Wang, W. Olovsson, and R. I. G. Uhrberg. Bands structure of hydrogenated silicene on ag(111): Evidence for half-silicane. *Phys. Rev. B*, 93:081406(R), 2016.

[166] W. Wei, Y. Dai, and B. Huang. Hydrogenation of silicene on ag(111) and formation of half-silicene. *J. Mater. Chem. A*, 5:18128, 2017.

[167] A Molle, C Grazianetti, L Tao, D Taneja, Md Hasibul Alam, and D Akinwande. Silicene, silicene derivatives, and their device applications. *Chem. Soc. Rev.*, 47:6370, 2018.

[168] H. Liu, N. Han, and J. Zhao. Temperature and coverage effects on the stability of epitaxial silicene on ag(111) surfaces. *Appl. Surf. Sci.*, 409:97–101, 2017.

[169] H U Yang, J D'Archangel, M L Sundheimer, E Tucker, G D Boreman, and M B Raschke. Optical dielectric function of silver. *Phys. Rev. B*, 91:235137, 2015.

[170] P-O. Löwdin. On the non-orthogonality problem connected with the use of atomic wave functions in hte theory of molecules and crystals. *J. Chem. Phys.*, 18:365, 1950.

[171] W. Rzodkiewicz and A. Panas. Application of spectroscopic ellipsometry for investigations of compaction and decompactionstate in si-sio$_2$ systems. *J. Phys.: Conf. Ser.*, 181:012035, 2009.

[172] A. Rivera, J. Olivares, A. Prada, M.L. Crespillo, M.J. Caturla, E.M. Bringa, J.M. Perlado, and O. Peña Rodríguez. Permanent modifications in silica produced by ion-induced high electronic excitation: experiments and atomistic simulations. *Sci. Rep.*, 7:10641, 2017.

[173] B. Lalmi, H. Oughaddou, H. Enriquez, A. Kara, S. Vizzini, B. Ealet, and B. Aufray. Epitaxial growth of a silicene sheet. *Appl. Phys. Lett.*, 97:223109, 2010.

[174] A. Kara, H. Enriquez, A.P. Seitsonen, L.C.L.Y. Voon, S Vizzini, B. Aufray, and H. Oughaddou. A review on silicene – new candidate for electronics. *Surf. Sci. Rep.*, 67:1, 2012.

[175] H. Oughaddou, H. Enriquez, M. R. Tchalalaa, H. Yildirim, A.J. Mayne, Bendounan A., G. Dujardin, M. Ait Ali, and Kara. A. Silicene, a promising new 2d material. *Progress in Surface Science*, 90:46, 2015.

[176] M.R. Tchalalaa, A.J. Enriquez, H. and Mayne, Kara. A., S. Roth, M.G. Silly, B. Bendounan, S. Sirotti, T. Greber, B. Aufray, G. Dujardin, M. Ait Ali, and H. Oughaddou. Formation of one-dimensional self-assembled silicon nanoribbons on au(110)-(2x1). *Applied Physics letters*, 102:083107, 2013.

[177] S. Sadeddine, H. Enriquez, A. Bendounan, P. Das, I. Vobornik, A. Kara, A. Mayne, F. Sirotti, G. Dujardin, and H. Oughaddou. Compelling experimental evidence of a dirac cone in the electronic structure of a 2d silicon layer. *Sci. Rep.*, 7:44400, 2017.

[178] A.F.R. Fleurence, T. Ozaki, H. Kawai, Y. Wang, and Y.T. Yukiko. Experimental evidence for epitaxial silicene on diboride thin films. *Phys. Rev. Lett.*, 108:245501, 2012.

[179] L. Meng, Y. Wang, and et al. Buckled silicene formation on ir(111). *Nano Lett.*, 13:685, 2013.

[180] C.L. Lin, R. Arafune, K. Kawahara, M. Kanno, N. Tsukahara, E. Minamitani, Y. Kim, M. Kawai, and N. Takagi. Substrate-induced symmetry breaking in silicene. *Phys. Rev. Lett.*, 110:076801, 2013.

[181] Y.P. Wang and H.P. Cheng. Absence of a dirac cone in silicene on ag(111): First-principles density functional calculations with a modified effective band structure technique. *Phys. Rev. B*, 87:245430, 2013.

[182] P. Vogt, P. De Padova, C. Quaresima, J. Avila, E. Frantzeskakis, M.C. Asensio, A. Resta, B. Ealet, and G. Le Lay. Silicene: compelling experimental evidence for graphenelike two-dimensional silicon. *Phys. Rev. Lett.*, 108:155501, 2012.

[183] L. Chen, C.C. Liu, B. Feng, X. He, P. Cheng, Z. Ding, S. Meng, Y. Yao, and K. Wu. Evidence for dirac fermions in a honeycomb lattice based on silicon. *Phys. Rev. Lett.*, 109:056804, 2012.

[184] J. Repp, G. Meyer, S.M. Stojković, A. Gourdon, and C. Joachim. Molecules on insulating films: scanning-tunneling microscopy imaging of individual molecular orbitals. *Phys. Rev. Lett.*, 94:026803, 2005.

[185] B. Doppagne, M.C. Chong, E. Lorchat, S. Berciaud, M. Romeo, H. Bulou, A. Boeglin, F. Scheurer, and G. Schull. Vibronic spectroscopy with submolecular resolution from stm-induced electroluminescence. *Phys. Rev. Lett.*, 118:127401, 2017.

[186] J. Repp, G. Meyer, F.E. Olsson, and M. Persson. Controlling the charge state of individual gold adatoms. *Science*, 305:493, 2004.

[187] K. Quertite, K. and Lasri, H. Enriquez, A. Mayne, A. Bendounan, G. Dujardin, N. Trcera, W. Malone, A. El Kenz, A. Benyoussef, A. Kara, and H. Oughaddou. Atomic structure of submonolayer nacl grown on ag(110) surface. *J. Phys. Chem. C*, 121:20272, 2017.

[188] K. Quertite, H. Enriquez, N. Trcera, Y. Tong, A. Bendounan, A.J. Mayne, G. Dujardin, P. Lagarde, A. El kenz, A. Benyoussef, A. Kara, and H. Oughaddou. Silicene synthesis on insulating thin film. private communication.

[189] T. Thonhauser, V.R. Cooper, S. Li, A. Puzder, P. Hyldgaard, and D.C. Langreth. Van der waals density functional: Self-consistent potential and the nature of the van der waals bond. *Phys. Rev. B*, 76:125112, 2007.

[190] V.O. Özçelik and S. Ciraci. Local reconstructions of silicene induced by adatoms. *J. Phys. Chem. C*, 117:26305, 2013.

[191] Y. Sakai and A. Oshiyama. Structural stability and energy-gap modulation through atomic protrusion in freestanding bilayer silicene. *Phys. Rev. B*, 91:201405(R), 2015.

[192] D. Kaltsas and L. Tsetseris. Stability and electronic properties of ultrathin films of silicon and germanium. *Phys. Chem. Chem. Phys.*, 15:9710, 2013.

[193] Shuang Li, Yifeng Wu, Yi Tu, Yonghui Wang, Tong Jiang, Wei Liu, and Yonghao Zhao. Defects in silicene: Vacancy clusters, extended line defects, and di-adatoms. *Sci. Rep.*, 5:7881, 2015.

[194] A. Kara, C. Leandr, M.E. Dávila, P. De Padova, B. Ealet, H. Oughaddou, B. Aufray, and G. LeLay. Physics of silicene stripes. *J. Supercond. Nov. Magn.*, 22:259, 2009.

[195] A. Kara, S. Vizzini, C. Leandri, B. Ealet, H. Oughaddou, B. Aufray, and G. LeLay. Silicon nano-ribbons on ag(110): a computational investigation. *J. Phys.: Condens. Matter*, 22:045004, 2010.

[196] C. Hogan, S. Colonna, R. Flammini, A. Circenti, and F. Ronci. Structure and stability of si/ag(110) nanoribbons. *Phys. Rev. B*, 92:115439, 2015.

[197] J.I. Cedrá, J. Slawińska, G. Le Lay, A.C. Marele, and J Gómez-Rodríguez. Unveiling the pentagonal nature of perfectly aligned sing-and double-strand si nanoribbons on ag(110). *Nat. Commun.*, 7:13076, 2016.

[198] G. Prévot, C. Hogan, T. Leoni, R. Bernard, E. Moyen, and L. Masson. Si nanoribbons on ag(110) studied by grazing-incidence x-ray diffraction, scanning tunneling microscopy, and density functional theory: Evidence of pentamer chain structure. *Phys. Rev. Lett.*, 117:276102, 2016.

[199] M. Ferri, G. Fratesi, G. Onida, and A. Debernardi. Ab initio study of the structural, electronic, magnetic, and optical properties of silicene nanoribbons. *Phys. Rev. B*, 99:085414, 2019.